

MULTI-SENSOR CALIBRATION AND VALIDATION OF THE UWO-PCL
WATER VAPOUR LIDAR
(Spine title: Calibration of the PCL Water Vapour Lidar)
(Thesis format: Monograph)

by

Robin Wing

Graduate Program in Physics and Astronomy

A thesis submitted in partial fulfillment
of the requirements for the degree of
Masters of Science

The School of Graduate and Postdoctoral Studies
The University of Western Ontario
London, Ontario, Canada

© Robin Wing 2012

THE UNIVERSITY OF WESTERN ONTARIO
School of Graduate and Postdoctoral Studies

CERTIFICATE OF EXAMINATION

Supervisor:

.....
Dr. R. J. Sica

Examiners:

.....
Dr. M. Houde

Supervisory Committee:

.....
Dr. P. G. Brown

.....
Dr. P. Barmby

.....
Dr. M. Zinke-Allmang

.....
Dr. J. Voogt

The thesis by

Robin Wing

entitled:

Multi-sensor Calibration and Validation of the UWO-PCL Water Vapour Lidar

is accepted in partial fulfillment of the
requirements for the degree of
Masters of Science

.....
Date

.....
Chair of the Thesis Examination Board

Acknowlegements

I would like to thank Dr. R.J. Sica for his support, guidance and understanding over the past few years. I truely appreciate the experiences I have had and the lessons I have learned while working in the PCL lab. I would also like to thank Dr. P.S. Argall for his support in the lab and Dr. D.N. Whiteman for organising the PCL water vapour calibration campaign. I would like to acknowledge the tremendous support I have recieved from the departmental staff; my advisory committee members, Dr. P.G. Brown and Dr. M. Zinke-Allmang; B. Stonehouse at UWO Facilities Management; P. Duenk and C. Rasenberg at the Environmental Science Western Field Station; the NASA campaign team; and all the workstudy students who have helped our lab to record hundereds of hours of observations. Finally, I would like to thank my group members, past and present, E. McCullough, B. Iserhienrhien, F. Olofsson, J. Khanna, J. Bandoro, P. Argall, and A. Jalali.

Abstract

The Purple Crow Lidar (PCL) has recently participated in a water vapour validation campaign with the NASA/GSFC Atmospheric Laboratory for Validation/Interagency Collaboration and Education (ALVICE) Lidar. The purpose of this calibration campaign is to ensure that PCL water vapour measurements are of sufficient quality for use in scientific investigations of atmospheric change and to be included in the Network for the Detection of Atmospheric Climate Change (NDACC) data base. The detection of long term changes in water vapour concentration, particularly in the upper troposphere and lower stratosphere (UTLS), is an issue of pressing scientific, ecological and societal concern.

The field campaign took place at the University of Western Ontario Environmental Research Field Station near London Ontario Canada, from May 23rd to June 10th 2012 and resulted in 57 hours of measurements taken over 12 clear nights. On each night a minimum of one RS92 radiosonde was launched. In addition, 3 cryogenic frost-point hygrometer (CFH) sondes were launched on clear nights over the course of the campaign. Measurements were obtained from near the surface up to \sim 20 km by both lidar systems, the radiosondes, and the CFH balloons. These measurements were used to calibrate profiles of water vapour mixing ratio by the newly relocated PCL.

Comparisons between measurements of water vapour mass mixing ratio taken by RS92 radiosondes, Cryogenic Frostpoint Hygrometers, and the ALVICE and PCL lidars has resulted in the derivation of a system calibration factor of $\xi_{sys} = 0.7545$. The application of this calibration factor to PCL retrievals has allowed for the validation of PCL water vapour mass mixing ratio profiles to within $\pm 5\%$ between the altitudes of 2 km and 9 km.

Keywords: Raman-scatter lidar, UTLS water vapour, multi-instrument calibration, radiosonde, cryogenic frost point hygrometer

Contents

Certificate of Examination	ii
Abstract	iv
List of Figures	viii
List of Tables	xii
List of Appendices	xiii
1 A Review of Some Atmospheric Concepts	1
1.1 Introduction	1
1.2 Atmosphere Pressure for an Isothermal Atmosphere	2
1.3 Atmospheric Composition	3
1.4 Temperature Structure	5
1.5 Troposphere	5
1.6 Stratosphere	8
1.7 Water Vapour in the Atmosphere	8
1.7.1 Qualitative Discussion	9
1.7.2 Quantitative Discussion	11
1.7.3 Saturation Vapour Pressure as Applied to the Atmosphere	13
1.8 Atmospheric Scattering	16
1.8.1 Mie Scattering	17
1.8.2 Rayleigh Scattering	17
1.8.3 Raman Scattering	19
2 Lidar Instrumentation	24
2.1 Introduction	24
2.2 The Purple Crow Lidar History	24
2.3 PCL Sub-systems	26
2.3.1 The Transmitter	26
The Laser head	26
The Laser Power Supply and Cooling	28
The Beam Expander	32
The Optical Path	34
2.3.2 The Receiver	35

The Liquid Mercury Telescope	35
The Air Bearing and Breaking System	38
The Dish	39
The Detector Box	40
3 LIDAR Data Acquisition and Processing	42
3.1 Introduction	42
3.2 The LIDAR Equation	42
3.3 The Water Vapour Mixing Ratio Equation	44
Atmospheric Terms	45
System-specific Terms	46
Calibration and Correction Terms	47
4 Purple Crow Lidar Calibration	48
4.1 Introduction	48
4.2 NDACC Requirements	48
4.3 PCL-ALVICE Calibration Campaign	49
4.4 Radiosondes	49
4.5 Saturation Vapour Pressure Models	52
4.5.1 Uncertainties	52
4.5.2 Saturation Vapour Pressure over Water and Ice	54
4.5.3 Quantifying the RS92 Uncertainties	57
Temperature Uncertainty	58
Relative Humidity Uncertainty	58
Creating an Uncertainty Envelope for the SVP Models	59
4.6 Cryogenic Frost Point Hygrometers	60
4.6.1 Past Lidar-CFH Comparisons	62
5 Results and Discussion	65
5.1 Summary	65
5.2 The Calibration Fitting Factor Results	65
5.3 Testing the Calibration Fitting Factor	68
5.3.1 Difference Profiles	70
5.4 Applying the Calibration Fitting Factor	70
5.5 Case Study: June 8th Cirrus Cloud Event	74
6 Conclusions and Future Directions	80
6.1 Conclusion	80
6.2 Future Work	80
6.2.1 Instrumentation	80
6.2.2 Software	82
6.2.3 Calibration	82
Bibliography	83
A Campaign Data	91

A.1	May 24th 2012	91
A.2	May 25th 2012	96
A.3	May 26th 2012	98
A.4	May 28th 2012	100
A.5	May 29th 2012	102
A.6	June 4th 2012	104
A.7	June 6th 2012	107
A.8	June 7th 2012	110
A.9	June 8th 2012	112
A.10	June 10th 2012	116
B	Sample Code	118
B.1	Call PCL Water Code	118
B.2	RS92 data	118
B.3	Generating Water Vapour Mixing Profile from RS92	119
B.4	Call the ALVICE Data	119
B.5	Determine the Fitting Factor for Each Night	120
B.6	Generating a Reduced Chi-Squared Metric	121
B.7	Saturation Vapour Pressure Model Analysis	121
Curriculum Vitae		124

List of Figures

1.1	An atmospheric pressure profile calculated using the Barometric Formula.	4
1.2	An atmospheric temperature profile based on the US Standard Atmosphere values. [26]	6
1.3	A phase transition diagram for water.	7
1.4	Enthalpy of fusion and vapourization of water. [61]	9
1.5	Atmospheric absorption bands for water. [24]	10
1.6	Infinite pool of water below a vacuum. [59]	13
1.7	Stokes and anti-Stokes shifts with respect to Rayleigh scatter. PCL water vapour measurements rely on Stokes, or red-shifted Raman scatter from 532 nm.	20
1.8	Energy transitions for vibrational and rotational Raman scattering. [3]	21
1.9	Raman scatter showing the O-branch, Q-branch, and S-branch.	22
1.10	Water filter transmission at 293 K. [53]	22
1.11	Water filter transmission at 213 K.[53]	23
2.1	PCL schematic diagram containing Hg telescope and receiver system.	25
2.2	Schematic of the Litron LPY-7000 laser head.	26
2.3	Effect of doubler crystal temperature on laser output power.	28
2.4	Effect of room temperature on laser output power.	29
2.5	The output power of the laser can be modulated by varying the delay between triggering of the Oscillator (blue), Pre-amplifier (magenta), and Amplifier (yellow). The time delay of the emitted pulse is shown in green. [31]	31
2.6	Schematic of beam expander. [60]	33
2.7	Depiction of far field divergence from a laser aperture or terminal optic.	34
2.8	Original blueprint for the PCL optical transmission path.	35
2.9	Confirming the focal length of the liquid mercury telescope is 5.175 m. The red line represents measurements of the height in meters above the surface of the mirror. The blue curve is a fit to the count rates measured by the detector system while the mirror is rotating slowly. The green points are the count rates measured by the detector system while the mirror is rotating quickly. The mirror is unstable between the blue and green curves.	37
2.10	Schematic of the liquid mercury telescope from Borra et al. (1992). [8]	37

2.11	A plot which describes the leveling of the surface of the telescope dish. Green squares represent shims placed under the base of the mirror, red triangles represent lead weights hung from the rim of the mirror, blue diamonds are mirror surface height measurements made from a mounted engineer's clock. The mirror is leveled to better than 1:5000.	40
2.12	A schematic of the reworked PCL detector box. Adapted from [10]	41
4.1	Experimental data measuring SVP over ice. Text in red indicates the average cold point temperature for the PCL calibration campaign. Taken and modified from Murphy and Koop 2005 [38]	53
4.2	Model outputs measuring SVP over ice with respect to the Goff-Gratch equation. Taken and modified from Holger Vömel [64]	54
4.3	Variations in SVP with temperature over water (red) and between water and ice (green). Adapted from [68]	55
4.4	Variation between SVP models between 14 and 20 km for radiosonde data taken May 24 at 3:39 UTC. There is a factor of approximately two between calculations of the SVP according to the Tsonis and Murphy-Koop models.	56
4.5	Ratios of SVP models for water and ice as a function of temperature.	56
4.6	Ratios of SVP models to Wexler 1976.	57
4.7	Percent difference of mass mixing ratios generated from Wexler minus Murphy-Koop model outputs from RS92 data taken during the PCL calibration campaign. The Wexler model has a wet bias with respect to the Murphy-Koop model between 8 km and 14 km.	58
4.8	Uncertainty in RS92 temperature retrievals. Blue is measurement uncertainty, black is uncertainty due to solar heating, and red is total uncertainty. [22]	59
4.9	Percentile difference profile between RS92 RH profiles and CFH RH profiles. [35]	60
4.10	Percent difference between Murphy-Koop 2005 and Tsonis 2002 at altitudes from 275 m to 30 km.	61
4.11	Schematic of the cryogenic frost point hygrometer (CFH). Shown is the cryogenic tank which holds the carbon tetraflouride, the heater coil, the mirror, and the optical frost layer detection system Taken from [62]	62
4.12	Initial CFH-lidar comparison contaminated by fluorescence. Taken from [28]	63
4.13	CFH-lidar comparison up to 18 km . Taken from [33]	64
5.1	The scale factor is only generated from measurements between 3 and 8 km.	67
5.2	Percent difference between each RS92 MMR profile and the hourly profile from PCL.	69
5.3	Percent difference between the ensemble of RS92 and PCL profiles of MMR with RMS errors.	69
5.4	Comparison of the percent difference plots between RS92&PCL and RS92&CFH. [35]	71
5.5	Percent difference with height for PCL and ALVICE MMR profiles.	72

5.6	Example of a scaled tropospheric PCL lidar profile compared to an RS92 profile and an ALVICE profile accompanied by a percent difference plot between each of the CFH, RS92 and ALVICE with PCL.	73
5.7	Percent difference between the ensemble of ALVICE and PCL profiles of MMR with RMS errors.	73
5.8	PCL and ALVICE stratospheric water vapour returns.	74
5.9	Unexpected drop in CFH VMR compared to both lidars.	75
5.10	Unexplained deviations between the CFH and the lidars above 10.5 km.	75
5.11	Approximation for the flight path for the June 8th CFH.	76
5.12	Standard CFH and iMet plot for June 8th. CFH (purple), RS92 radiosonde (red), iMET radiosonde (yellow), and SVP curve (black dots). 100% RH is occurring near 10 km.	78
5.13	PCL and ALVICE stratospheric water vapour returns.	79
6.1	Ground loop contaminating PCL returns below ~3 km.	81
A.1	PCL nightly colour plot of tropospheric water for May 24th.	92
A.2	PCL, ALVICE, and RS92 mass mixing ratio profiles for May 24th at 3:39 UTC.	92
A.3	PCL, ALVICE, RS92, and CFH mass mixing ratio profiles for May 24th at 6:59 UTC.	93
A.4	PCL and ALVICE volume mixing ratio profiles for May 24th at 3:39 UTC.	93
A.5	PCL, ALVICE, and CFH volume mixing ratio profiles for May 24th at 6:59 UTC.	94
A.6	RS92 profiles for temperature (red) and RH (black) on May 24th at 3:39 UTC.	94
A.7	RS92 profiles for temperature (red) and RH (black) on May 24th at 6:59 UTC.	94
A.8	CFH profile for temperature on May 24th at 4:02 UTC.	95
A.9	PCL nightly colour plot of tropospheric water for May 25th.	96
A.10	PCL, ALVICE, and RS92 mass mixing ratio profiles for May 25th at 3:57 UTC.	96
A.11	PCL and ALVICE volume mixing ratio profiles for May 25th at 3:57 UTC.	97
A.12	RS92 profiles for temperature (red) and RH (black) on May 25th at 3:57 UTC.	97
A.13	PCL nightly colour plot of tropospheric water for May 26th.	98
A.14	PCL, ALVICE, and RS92 mass mixing ratio profiles for May 26th at 3:39 UTC.	98
A.15	PCL and ALVICE volume mixing ratio profiles for May 26th at 3:39 UTC.	99
A.16	RS92 profiles for temperature (red) and RH (black) on May 26th at 3:40 UTC.	99
A.17	PCL nightly colour plot of tropospheric water for May 28th.	100
A.18	PCL, ALVICE, and RS92 mass mixing ratio profiles for May 28th at 3:31 UTC.	100
A.19	PCL and ALVICE volume mixing ratio profiles for May 28th at 3:31 UTC.	101
A.20	RS92 profiles for temperature (red) and RH (black) on May 28th at 3:31 UTC.	101
A.21	PCL nightly colour plot of tropospheric water for May 29th.	102
A.22	PCL, ALVICE, and RS92 mass mixing ratio profiles for May 29th at 3:31 UTC.	102
A.23	PCL and ALVICE volume mixing ratio profiles for May 29th at 3:31 UTC.	103
A.24	RS92 profiles for temperature (red) and RH (black) on May 29th at 3:38 UTC.	103
A.25	PCL nightly colour plot of tropospheric water for June 4th.	104
A.26	PCL, ALVICE, and RS92 mass mixing ratio profiles for June 4th at 3:22 UTC.	104
A.27	PCL, ALVICE, and RS92 mass mixing ratio profiles for June 4th at 5:40 UTC.	105
A.28	PCL and ALVICE volume mixing ratio profiles for June 4th at 3:22 UTC.	105

A.29 PCL and ALVICE volume mixing ratio profiles for June 4th at 5:40 UTC.	105
A.30 RS92 profiles for temperature (red) and RH (black) on June 4th at 3:22 UTC. .	106
A.31 RS92 profiles for temperature (red) and RH (black) on June 4th at 5:40 UTC. .	106
A.32 PCL nightly colour plot of tropospheric water for June 6th.	107
A.33 PCL,ALVICE, and RS92 mass mixing ratio profiles for June 6th at 3:12 UTC. .	107
A.34 PCL,ALVICE, and RS92 mass mixing ratio profiles for June 6th at 5:29 UTC. .	108
A.35 PCL and ALVICE volume mixing ratio profiles for June 6th at 3:12 UTC.	108
A.36 PCL and ALVICE volume mixing ratio profiles for June 6th at 5:29 UTC.	109
A.37 RS92 profiles for temperature (red) and RH (black) on June 6th at 3:11 UTC. .	109
A.38 RS92 profiles for temperature (red) and RH (black) on June 6th at 5:29 UTC. .	109
A.39 PCL nightly colour plot of tropospheric water for June 7th.	110
A.40 PCL and RS92 mass mixing ratio profiles for June 7th at 3:45 UTC.	110
A.41 PCL volume mixing ratio profiles for June 6th at 3:45 UTC.	111
A.42 RS92 profiles for temperature (red) and RH (black) on June 7th at 3:45 UTC. .	111
A.43 PCL nightly colour plot of tropospheric water for June 8th.	112
A.44 PCL,ALVICE, and RS92 mass mixing ratio profiles for June 8th at 3:53 UTC. .	112
A.45 PCL,ALVICE, RS92, and CFH mass mixing ratio profiles for June 8th at 6:51 UTC.	113
A.46 PCL, ALVICE, and CFH volume mixing ratio profiles for June 8th at 3:53 UTC.	113
A.47 PCL and ALVICE volume mixing ratio profiles for June 8th at 6:51 UTC. . . .	114
A.48 RS92 profiles for temperature (red) and RH (black) on June 8th at 3:53 UTC. .	114
A.49 RS92 profiles for temperature (red) and RH (black) on June 8th at 6:51 UTC. .	114
A.50 CFH profile for temperature on June 8th at 2:51 UTC.	115
A.51 PCL nightly colour plot of tropospheric water for June 10th.	116
A.52 PCL,ALVICE, and RS92, mass mixing ratio profiles for June 10th at 4:02 UTC.	116
A.53 PCL and ALVICE volume mixing ratio profiles for June 10th at 4:02 UTC. . . .	117
A.54 RS92 profiles for temperature (red) and RH (black) on June 10th at 4:02 UTC. .	117

List of Tables

1.1	Fractional concentration of gasses in Earth's atmosphere. [68]	4
2.1	Optical specifications for the liquid mercury telescope.	36
3.1	Water vapour mixing ratio equation atmospheric parameters.	45
3.2	Reflectivity of PCL detector box optics.	46
4.1	PCL-ALVICE field campaign log.	50
5.1	Table of derived lidar fitting factors and reduced chi-squared values for each night of good data during the campaign.	66
5.2	Table of the average percent difference between MMR values measured by PCL and ALVICE lidars for each night of good data during the campaign. Poor fits have percent differences greater than 10%, acceptable fits have differences between 5% and 10%, and excellent fits have differences less than 5%.	71

List of Appendices

Appendix A	91
Appendix B	118

Chapter 1

A Review of Some Atmospheric Concepts

1.1 Introduction

The atmosphere makes life on Earth possible. It shields us from harmful extra-planetary radiation; it moderates the surface temperature of the planet and insulates us from the diurnal solar cycle; it allows for a common, well mixed reservoir of gasses from which organisms can cycle necessary chemical compounds; and it provides a medium for the long range transport and circulation of water.

The presence of water vapour in the atmosphere is a very important, but imperfectly understood, variable in the global atmospheric radiation balance. It is expected that in the troposphere water vapour acts as a greenhouse gas and warms the atmosphere by absorbing and remitting long wave infrared radiation. As the temperature of the atmosphere warms, it is expected that an increase in the concentration of water vapour in the air will occur. This process in turn will cause more heating and act as a positive feedback mechanism.

However, as the concentration of water molecules increases in the lower atmosphere, it is expected that more clouds will be formed as more moist air is lifted and cooled. Clouds are a key component in reflecting incoming solar rays, preventing higher frequency light from being absorbed and re-emitted from the surface. If this effect is dominant, it would act to cool the lower atmosphere, limiting water-driven heating, which in turn limits cloud formation. This effect is known as cloud feedback and is a sensitive negative feedback loop parameter in most

global climate models.

The above mechanisms are well understood and are a part of the many complexities in attempting to make model forecasts of global atmospheric change. A more full description of these phenomena can be found in the IPCC 2007 report [25]. One of the major issues with properly incorporating the effects of increased water vapour in both the troposphere and the lower stratosphere is the absence of a long term, reliable, well calibrated measurements [25].

Currently, water vapour mixing ratio can be measured by various kinds of satellites such as the Atmospheric Chemistry Experiment (ACE), through measurements from humidity sensors mounted on commercial and research aircraft, by dropsonde and radiosonde campaigns, and by Raman Lidar techniques [36]. Each instrument type has observational strengths and weaknesses and lidar is no exception. The lidar technique provides excellent spatial and temporal resolution measurements of water vapour mixing ratio but has limited geographic coverage, requires extensive expertise for construction, maintenance and operation, and requires calibration and routine checks on data consistency. This thesis will focus on the calibration of Raman lidar measurements of water vapour in the upper troposphere and lower stratosphere (UTLS).

1.2 Atmosphere Pressure for an Isothermal Atmosphere

The homogeneous, neutral atmosphere is a relatively well mixed, stably stratified fluid extending from the planet's surface to the turbopause, a region which is nominally located between 95 and 115 km in altitude. The gravitational attraction between Earth and its atmosphere gives rise to an exponential decrease in pressure with height, as lower layers of gas are compressed under the weight of layers at higher altitudes. By invoking the equation of state for an ideal gas, (1.1) where P is the gas pressure (Pa), ρ is the gas density in $\frac{\text{kg}}{\text{m}^3}$, R is the universal gas constant for dry air and is equal to $8.314 \frac{\text{N}\cdot\text{m}}{\text{mol}\cdot\text{K}}$, and T is the gas temperature in Kelvin, an expression

which balances the pressure gradient force with gravity can be derived.

$$P = \rho RT \quad (1.1)$$

This condition, known as the Hydrostatic Equilibrium Equation, (1.2),

$$\frac{dP}{dz} + \rho g = 0 \quad (1.2)$$

where $g(z)$ is the gravitational acceleration and the surface value is $9.80665 \frac{\text{m}}{\text{s}^2}$, allows us to characterize an e -folding height for the density curve of the atmosphere (1.4), where k is Boltzmann's Constant $1.3806488 \times 10^{23} \frac{\text{J}}{\text{K}}$, and M is the molar mass of air, which can be calculated from a periodic table, is $0.0289644 \frac{\text{kg}}{\text{mol}}$. A typical value of the e -folding, or scale height, in the region of Earth's atmosphere is approximately 8 km. A curve representing this exponential drop in pressure with altitude can be calculated using the Barometric Formula(1.3),

$$P = P_0 \cdot \exp \left[\frac{-g \cdot M \cdot z}{R \cdot T_0} \right] \quad (1.3)$$

where T_0 and P_0 are the respective temperatures and pressures at the surface, and can be seen in Figure 1.1.

$$H = \frac{kT}{Mg(z)} \quad (1.4)$$

1.3 Atmospheric Composition

Within this well mixed region, the composition of the atmosphere is uniform. Table 1.1 details the fractional concentration by volume for the most abundant gasses in Earth's atmosphere. Taken together, molecular nitrogen and molecular oxygen compose approximately 99.03% of the air with the trace gasses comprising the remaining fraction of a percent in the dry atmosphere. The one exception to this uniform gas mixture is water vapour, which has a range of

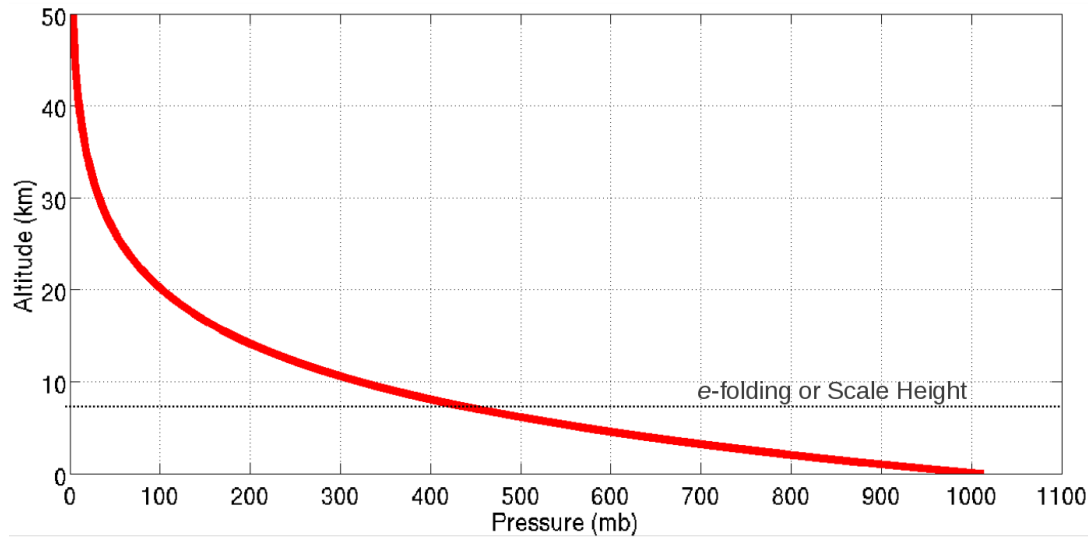


Figure 1.1: An atmospheric pressure profile calculated using the Barometric Formula.

Constituent	Molecular Weight	Fractional Concentration by Volume
Nitrogen (N ₂)	28.013	78.08%
Oxygen (O ₂)	32.000	20.95%
Argon (Ar)	39.95	0.93%
Water Vapour (H ₂ O)	18.02	0-5%
Carbon dioxide (CO ₂)	44.01	380 ppm
Neon (Ne)	20.18	18 ppm
Helium (He)	4.00	5 ppm
Methane (CH ₄)	16.04	1.75 ppm
Krypton (Kr)	83.80	1 ppm
Hydrogen (H ₂)	2.02	0.5 ppm
Nitrous oxide (N ₂ O)	56.03	0.3 ppm
Ozone (O ₃)	48.00	0-0.1 ppm

Table 1.1: Fractional concentration of gasses in Earth's atmosphere. [68]

values possible and is extremely variable in both space and time. This uncertainty in the concentration of water vapour can be intuitively understood as the variation in the humidity of our environment with temperature changes. The summer air is hot and humid, while the winter air tends to be cold and dry. A more formal exploration of how moisture in the atmosphere cycles and which physical parameters are important in its description are presented later in the chapter.

1.4 Temperature Structure

Temperature variations are important parameters in characterizing and understanding the atmosphere. The atmosphere can be divided into four regions, each of which is marked by a temperature gradient which is calculated from the hydrostatic balance equation (1.2) and a formulation of the first law of thermodynamics (1.5) where U is the internal energy of the system, δQ is an infinitesimal amount of heat supplied to the system by its surroundings, and dV is a change in the volume of the system. The four regions of the atmosphere are the troposphere, stratosphere, mesosphere, and thermosphere. For the purposes of this work only the lowest two regions will be considered; the dynamics and chemistry of water vapour in the mesosphere and thermosphere will be ignored.

$$dU = \delta Q - PdV \quad (1.5)$$

1.5 Troposphere

The troposphere is the lowest region extending from the surface of the planet up to nominally 10 km altitude and it is characterized by a negative lapse rate, convective and turbulent mixing, and an abundance of water vapour. It is also the region of the atmosphere that we associate with

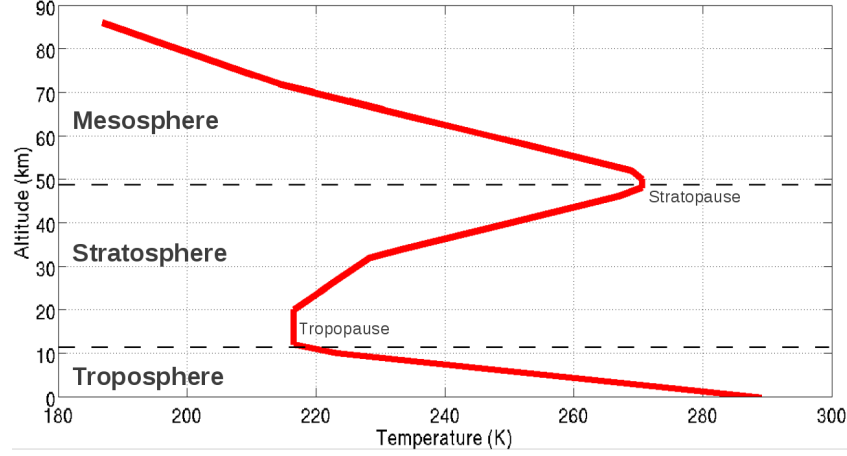


Figure 1.2: An atmospheric temperature profile based on the US Standard Atmosphere values. [26]

our day-to-day weather phenomena. Using an appropriate value for the specific heat capacity at constant pressure, $c_p = 29.07 \frac{\text{J}}{\text{mol}\cdot\text{K}}$, and the assumption of an adiabatically rising parcel of air we can derive equation (1.6) the Dry Adiabatic Lapse Rate (DALR) which is equal to $9.8 \frac{\text{K}}{\text{km}}$.

$$\Gamma_d = -\frac{dT}{dz} = \frac{g}{c_p} \approx 9.8 \frac{\text{K}}{\text{km}} \quad (1.6)$$

Given that water is a condensable gas and has easily accessible liquid, solid, and vapour states over a normal range of atmospheric pressures, the contributions of water to the thermodynamics of the atmosphere must be considered. Figure 1.3, shows the phase transition curves for water and have been sketched based on values listed in the CRC [30].

As water evaporates and condenses in Earth's atmosphere there is a flux of enthalpy into the surrounding air. If we assume that the atmosphere is completely saturated with water vapour, then the DALR must be modified to accommodate the enthalpy associated with the water which results in a Moist Adiabatic Lapse Rate (MALR). The MALR is typically around $5 \frac{\text{K}}{\text{km}}$ and is given by (1.7)

$$\Gamma_m = \frac{g}{c_p} \left[\frac{1 + \frac{Lq_s}{RT}}{1 + \frac{0.62L^2q_s}{c_p R_{H_2O} T^2}} \right] \quad (1.7)$$

where L is the enthalpy of water, R_{H_2O} is the universal gas constant for water, and q_s is a water

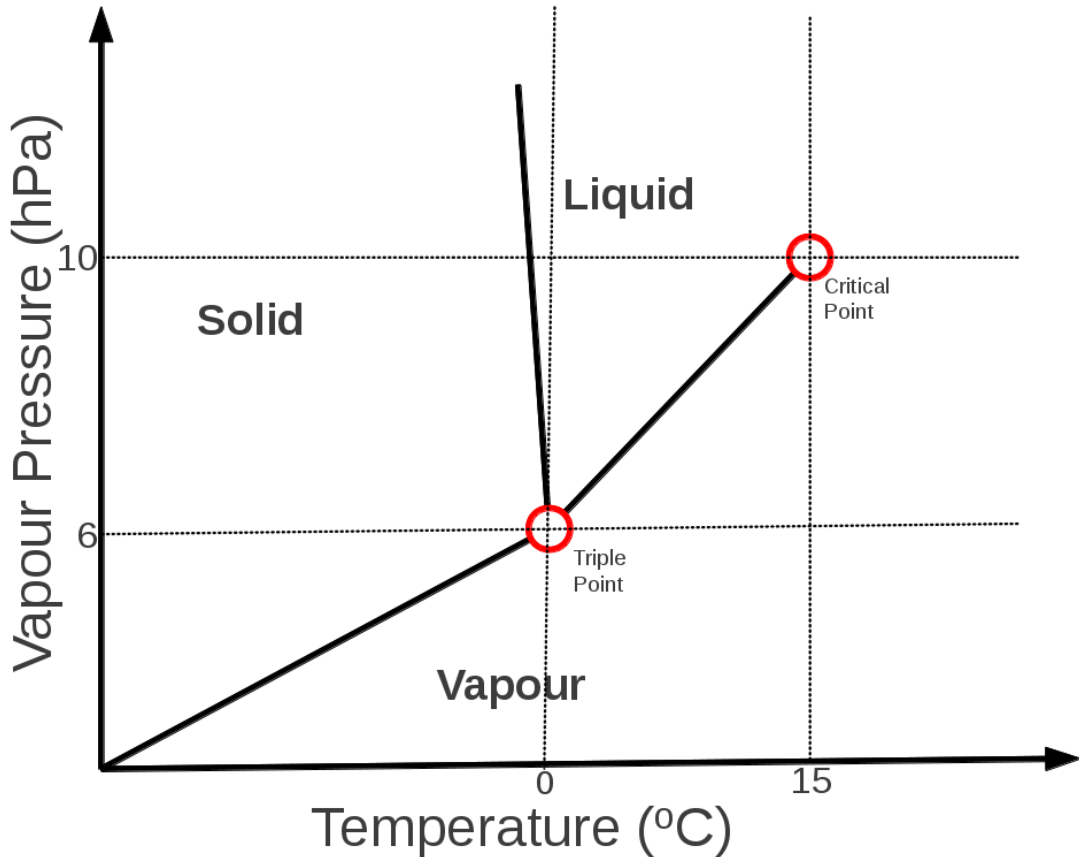


Figure 1.3: A phase transition diagram for water.

mixing ratio which will be defined later. The MALR is derived in a similar fashion to the DALR accounting for the enthalpy of the water contained in the air [20].

As can be seen from (1.6) and (1.7) the presence of water vapour in the atmosphere plays a crucial role in the temperature profile. If we imagine a parcel of dry air, composed of molecular nitrogen and molecular oxygen, having an average molar mass of approximately $29 \frac{\text{g}}{\text{mol}}$ [30] then we know that by adding moisture to the air parcel we make it lighter as the molar mass of water is approximately $18 \frac{\text{g}}{\text{mol}}$ [30]. Using the ideal gas law equation (1.1) we can see that the gas constant for dry air, R , needs to be slightly altered to R_{H_2O} , taking into account the moisture contained within the air parcel.

Above the troposphere is an intermediate region known as the tropopause. The tropopause is a region where the lapse rate fluctuates about zero and can be thought of as an isotherm. Associated with this change in lapse rate, the tropopause is often associated with a local minimum

in atmospheric temperature. Values colder than 210 K are not uncommon. The significance of this region of the atmosphere is that it acts as a partial barrier to the convective mixing of moist, tropospheric air and the drier non-convecting stratosphere directly above it. However, the transport of air across this region, known as stratosphere-troposphere exchange, can be driven by localized and transient dynamical, chemical and radiative coupling processes [21]. These processes are essential for the water vapour inventory of the stratosphere [42].

1.6 Stratosphere

The stratosphere is the region directly above the tropopause and extends to roughly 50 km altitude. The region gets its name from the stably stratified nature of the temperature profile. Whereas the troposphere features a negative lapse rate, the stratospheric temperature profile increases with increasing altitude due to the presence of ozone. This temperature inversion suppresses convection and damps out the vertical motions of injected tropospheric air. The ozone molecule, O_3 , absorbs incoming ultraviolet solar radiation and redistributes a portion of the energy as increased temperature.

Accurately measuring stratospheric water vapour is of particular interest to climate scientists as existing global climate models do not simulate temperature trends in the lower stratosphere very accurately and stratospheric chemistry-climate models cannot produce temperature profiles which match observations [23]. Well calibrated measurements of stratospheric water vapour are essential for calculating the radiative forcing on the stratosphere and for integration into prognostic climate models.

1.7 Water Vapour in the Atmosphere

As was discussed in section 1.3, water vapour is a very important, poorly understood and highly variable chemical species in the atmosphere. Its most critical role is manifested as a condensable greenhouse gas, as even relatively minute quantities can play a significant role in

the planet's atmospheric energy balance.

The following subsection will lay out a few qualitative points, summarized from [46], explaining why water vapour is such a potent atmospheric constituent and why it requires study. Following the qualitative summary a few useful metrics for the quantization of water vapour and saturation vapour pressure equations will be derived. Both of these ideas are of central importance to the calibration effort in this thesis.

1.7.1 Qualitative Discussion

Water vapour has a very large 'latent heat', hereafter properly referred to as enthalpy, associated with all of its phase transitions. Figure 1.4 gives an indication of the magnitudes of these enthalpies for the processes of vapourization and fusion [12]. As a result, the vapour pressure of water, at equilibrium, has a very strong dependence on temperature. The two most important consequences of this close connection between temperature and the phase state of water are:

- i) Water vapour abundance varies strongly with season, altitude, and latitude.

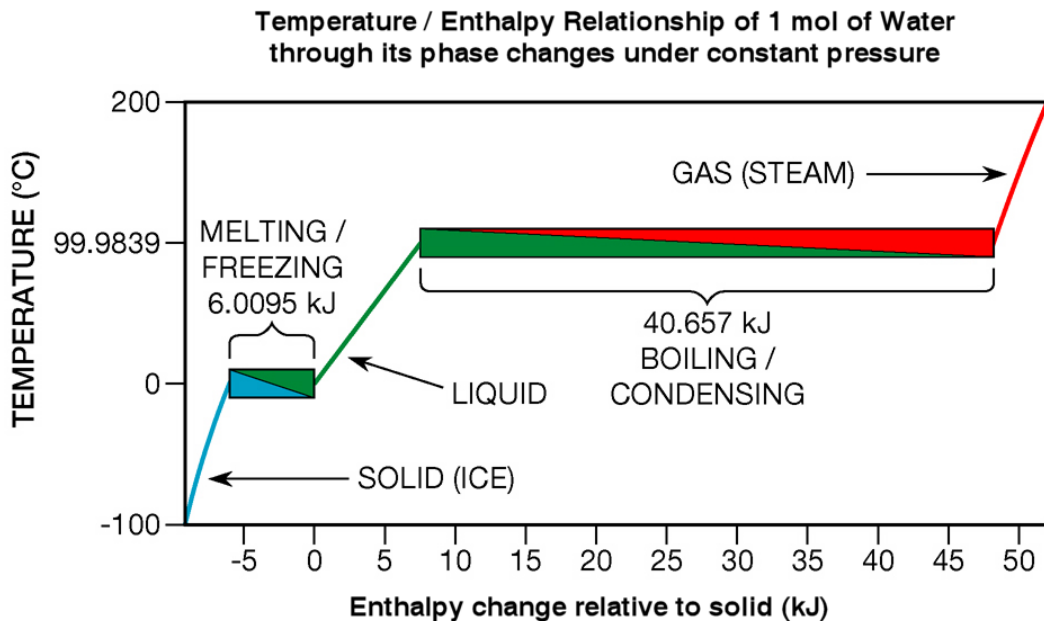


Figure 1.4: Enthalpy of fusion and vapourization of water. [61]

ii) The local abundance of water vapour may be perturbed by large scale atmospheric circulation patterns and convection, drawing it into regions where it is out of equilibrium with the temperature of the environment.

Due to the associated enthalpies associated with changes in state, water can act as a vector for the transport of significant amounts of energy throughout the atmosphere. For example, as water undergoes vapourization at the surface it requires energy and decreases the temperature of its surroundings. When that water vapour is then lifted convectively to an altitude where it becomes energetically favourable to condense, the water molecules release energy into their new environment and precipitate out of solution. From start to finish, this example transports heat from the surface aloft and greatly changes the radiative balance of the local atmosphere.

The H_2O molecule has a very complex set of absorption bands as can be seen in Figure 1.5. These absorption bands are interspersed with windows which transmit easily through the moist lower layers of the atmosphere. Looking at Figure 1.5 it can be seen that the light which

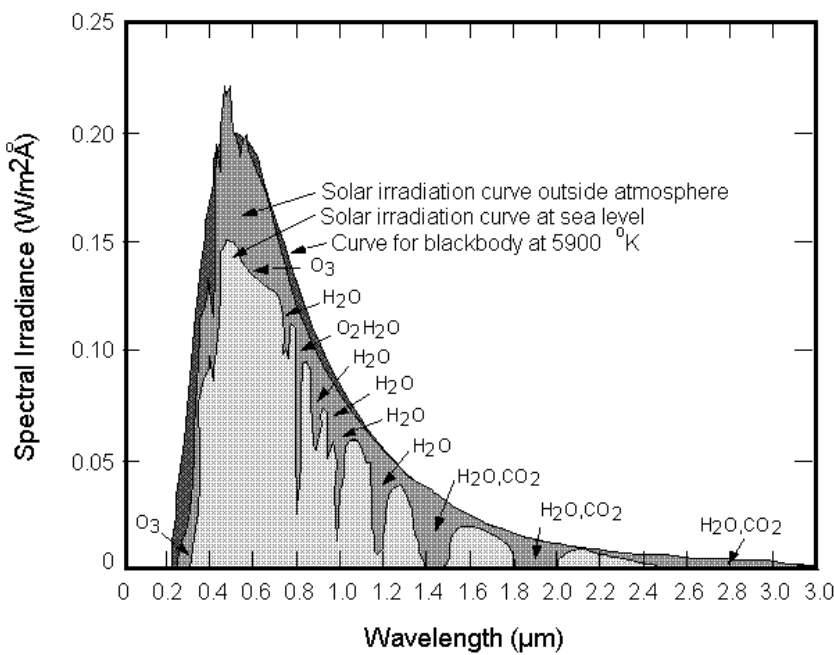


Figure 1.5: Atmospheric absorption bands for water. [24]

the Sun emits in the visible portion of the spectrum is weakly absorbed by water vapour, and is presumably then incident upon Earth's surface. When the Earth then re-radiates energy,

based on its black-body temperature, the IR radiation is strongly absorbed and re-emitted in several absorption bands which are associated with water vapour. This "trapping" of long wave, outgoing radiation, is the basic idea behind the "greenhouse effect", thus making water vapour a prominent greenhouse gas. Further, the concentration of this gas is closely linked to the long term warming trend of the troposphere as water is known to participate in a positive feedback loop where warmer temperatures promote a higher atmospheric water vapour concentration [23].

When water vapour condenses to form clouds of liquid or ice particles its optical properties also change. As can be observed, clouds are often opaque in the visible portion of the spectrum, and where once solar radiation passed freely through the atmosphere to the Earth's surface, now is reflected or absorbed by cloud layers. The clouds reflect incoming visible light and lower the planet's albedo, or reflection coefficient. With less light reaching the surface the planet should cool. As was mentioned in the introduction to this thesis, the fundamental question: Does increasing Earth's water vapour budget heat or cool the planet? is still open for exploration.

1.7.2 Quantitative Discussion

There are several common methods for quantifying the amount of water vapour in the atmosphere. The most basic measure is absolute humidity which is simply the number or mass density of water molecules over the number or mass density of molecules of "dry air" within a given volume. From the mass density we can express the 'partial pressure' of water vapour relative to the total pressure of the gas mixture. We can invoke a slightly modified form of the ideal gas law, equation (1.1), and define a partial pressure for water vapour, e , where ρ_{vapour} is the mass density of water vapour, R_{vapour} is the gas constant for water vapour, and T is the temperature of the gas mixture [68].

$$e = \rho_{vapour} R_{vapour} T \quad (1.8)$$

Carrying forward with the ideas of partial pressure and vapour mass density, two more metrics can be defined:

a. The humidity mixing ratio, w

$$w = \frac{\rho_{vapour}}{\rho_{dry}} \quad (1.9)$$

$$r = \frac{w}{w_{saturation}} \quad (1.10)$$

where ρ_{dry} is the mass density of dry air and $w_{saturation}$ is the saturation vapour mixing ratio which will be elaborated on in the next section [68]. Relating the mixing ratio, w , to the partial pressure of water vapour, e , using equation (1.11)

$$w \frac{R_{dry}}{R_{vapour}} \frac{e}{P - e} = 0.622 \frac{e}{P - e} \quad (1.11)$$

Where P is the total pressure of the gas and R_{dry} is the gas constant for air. The last (and most useful for this thesis) metric is called relative humidity RH and is properly defined in equation (1.12) [68].

$$RH = \frac{w}{w_s} = \frac{e}{e_s} \frac{P - e_s}{P - e} \quad (1.12)$$

Many texts and papers neglect the second half of the equation and approximate RH by $\frac{e}{e_s}$. One of the lessons learned from the MOHAVE campaign, which will be discussed in a later chapter, is that the contribution of the $\frac{P - e_s}{P - e}$ is essential when determining RH in very cold, dry environments like the lower stratosphere [29]. RH is seen to depend on pressure, which is a function of temperature, e , which was shown earlier to be a function of temperature, and on e_s , the saturation vapour pressure, which will be discussed in the next section and is also a function of temperature.

1.7.3 Saturation Vapour Pressure as Applied to the Atmosphere

Saturation vapour pressure (SVP) is a nuanced concept and some time will be taken to lay out a precise description. The framework for the following derivation comes from [5] but more detailed expressions from [38], [70], and [65] will be inserted where required.

Imagine an infinitely large and infinitely deep, flat, pool of water at constant temperature, T depicted in Figure 1.6. Above this pool there is only vacuum and we assume that any walls or surfaces are infinitely far away. The speed of water molecules depends upon the temperature of the liquid. There should be an expectation speed for the molecules, $\langle v \rangle$, which is proportional to the square root of temperature, and the distribution of the speeds from the expectation value should follow the Boltzmann distribution in a liquid.

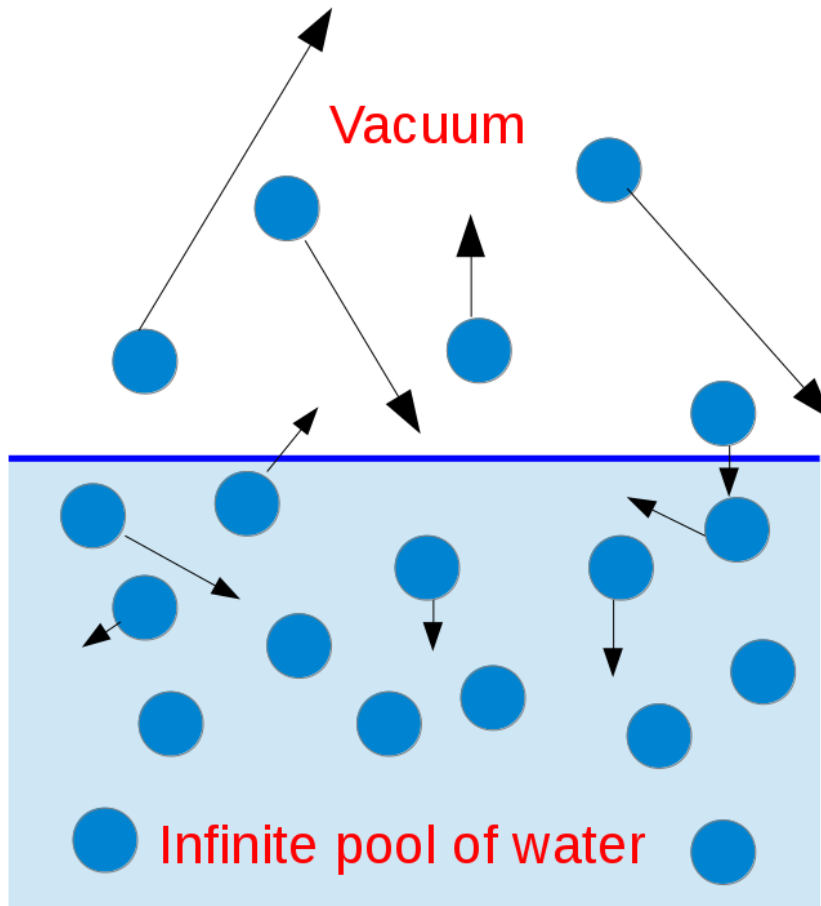


Figure 1.6: Infinite pool of water below a vacuum. [59]

When a sufficiently energetic water molecule near the surface has enough momentum to

over come the inter-molecular cohesion of the liquid it can escape into the vacuum. This process is evaporation, E , and it is only dependant on the temperature of the liquid. Again, we are assuming that our infinite pool is sufficiently large that the enthalpy of vapourization of the escaped molecule does not lower the temperature of the liquid.

Now we have some water vapour above the pool and it has some mass density, m_{vapour} , temperature, T_{vapour} (does not need to be the same as the liquid), and a distribution of molecular speeds about $\langle v_{vapour} \rangle$. We should expect some of the molecules in the vapour to have low kinetic energies and to collide with the surface of the liquid. When this happens the molecule may be seized by the cohesive forces and condensed, C , back into the liquid state. We should also expect that the number of condensation events is some function of the temperature of the vapour and the number of vaporized molecules. Equation (1.13) summarizes the preceding two paragraphs.

With these ideas about total evaporation and condensation we can define a net flux of water molecules between the liquid and gaseous states, equation (1.14). It is important to note that F_{net} is the quantity that our instruments measure, not F_{up} .

$$\frac{d(m_{vapour})}{dt} = E(T_{liquid})C(T_{vapour, m_{vapour}}) \quad (1.13)$$

$$F_{net} = F_{up} - F_{down} \quad (1.14)$$

In the previous section we defined the absolute humidity, w , as a vapour density ratio. Fluxes are really just the rate of change in time of number densities. If we set $T_{liquid} = T_{vapour} = T_{total}$ we should be able to use equation ([?]) to work out the saturation mixing ratio, w_s .

$$\frac{F_{up}}{F_{down}} = w \langle v(T) \rangle / w_s \langle v(T) \rangle \quad (1.15)$$

$$\frac{E}{C} = \frac{w}{w_s} \quad (1.16)$$

We have shown that SVP is a ratio of water vapour fluxes which depends only on temper-

ature and RH ; however, we have not given a functional form. SVP is a very difficult quantity to determine. It is very difficult to accurately measure the fluxes associated with an infinite flat pool as the introduction of an instrument or a surface alters the rate of condensation, especially at low temperatures [32]. Modelling the SVP also involves difficulties [38]. However, we can begin to sketch out the generalized form that an SVP model should take.

Beginning with the Clausius-Clapeyron equation (1.17) as given in [70].

$$\frac{d(e_s)}{dt} = \frac{L}{T(V - i)} \quad (1.17)$$

where L is the enthalpy of condensation or sublimation, V is the specific volume of the saturation vapour pressure for water vapour, and i is the specific volume of the saturation vapour pressure over ice.

Next we need an equation of state to describe the gasses being modelled. We will use a modified version of the ideal gas law (1.18) where Z is a measured compressibility factor instead of a mass or a density.

$$PV = ZRT \quad (1.18)$$

Combining equation (1.1) into equation (1.17) and separating like terms we arrive at Equation 1.19.

$$\frac{dP}{P} = \frac{L}{ZRT^2(1 + \frac{i}{v})dT} \quad (1.19)$$

Now we need to select a temperature range (and appropriately mapped pressure range) over which the equation will be valid. This is limited by the range over which measurements or models of L are available.

$$\int_{P_1}^{P_2} d\ln P = \int_{T_1}^{T_2} dT \frac{L}{ZRT^2(1 + \frac{i}{v})} \quad (1.20)$$

Until this point in the derivation we have not had to make any approximations or rely on measurements or modelling. Unfortunately, we now need an expression for both the enthalpy of ice, L_{ice} , and the enthalpy of water, L_{water} , which are accurate over the temperature range of interest. Much like with the lab experiments for measuring the SVP curve directly, experimental measurements of the enthalpy curves, such as the work done by Marti and Mauersberger (1993) [32], are technically challenging and do not produce sufficiently reliable results for our work.

The other approach for determining enthalpies at low temperatures is to write series expansions of the enthalpy terms, fit the terms with a polynomial and then extrapolate to low temperatures. Unfortunately, there are a multitude of models to choose from, all of which suffer from the typical blights of truncation, rounding, choice of fitting function, order, etc. with large variations existing between models by different authors. Murphy and Koop (2006) [38] wrote a review paper of the most prominent SVP models and came to the conclusion that there is very little basis for any of the models or measurements within the temperature regime of interest for this thesis. In chapter 4 a comparison of model outputs will be shown and the reasoning behind the choice of model choice for this work will be discussed.

1.8 Atmospheric Scattering

The scattering of light off particles in the atmosphere is an everyday phenomenon; we see bright, clear blue skies, white, grey and black clouds, red sunsets and sunrises, and at times many other shades of pink, purple and green. All these different picture-perfect moments can be described in terms of photons scattering off of atoms, molecules and aerosols.

In general, there are three major types of scattering which can occur: Mie, Rayleigh, and Raman and the returned observed light may be either coherent or incoherent.

1.8.1 Mie Scattering

Mie scattering happens when light scatterers off a particle with a radius much larger than the wavelength of the incident photon. Surface effects, shape, and refractive index are all important quantities to know when working with this kind of scattering. Mie scattering is typically associated with lidar studies of aerosols and for the purposes of this thesis I will not consider it.

1.8.2 Rayleigh Scattering

Rayleigh scattering is elastic scattering of a photon off a scattering target. Rayleigh scattering is a central technique employed by PCL so it is important to examine its postulates, PCL's data acquisition, and address any discrepancies between the two.

Rayleigh scattering has five assumptions:

- i) The scatterer must be smaller in size than the wavelength of the incident photon. The PCL transmits at 532 nm and we assume that the bulk atmospheric scatterers are molecular nitrogen and molecular oxygen typical cross sections for these molecules are estimated at 300 pm and 292 pm respectively [30]. Rayleigh scattering is valid for the majority of atmospheric constituents. Care must be taken when larger particles such as aerosols are present in the atmospheric sample.
- ii) The scatterer must not be ionized. Most molecules below the ionosphere, altitudes greater than approximately 90 km, are non-ionized. This work takes place in the lower and middle atmosphere so we are safe in using Rayleigh techniques.
- iii) The scatterers must have an internal index of refraction near unity. This condition is required to prevent large phase changes in the photon wave fronts as they move into the scatterer and out again. These phase changes can be conceptualized by recalling the definition of the absolute index of refraction equation (1.21), where c is the speed of light, v is the wave velocity, ϵ and μ represent Maxwell's permittivity values for free space and the dielectric.

$$n \frac{c}{v} = \sqrt{\frac{\epsilon\mu}{\epsilon_0\mu_0}} \quad (1.21)$$

The index of refraction for air is usually given as $n = 1.000293$ [19]. However, it is important to note that other atmospheric constituents, most importantly water vapour ($n \approx 1.33$) do not satisfy this criterion.

iv) The scatterers must be isotropic molecules which do not experience dipole oscillations when interacting with a photon. Neither molecular nitrogen nor molecular oxygen satisfies this criterion due to their diatomic structures. Fortunately, a correction for anisotropy was given by Cabannes which separates out the elastic component of the signal from the inelastic side lobes [49]. To be correct what PCL truly measures is called Rayleigh-Cabannes scattering as it assumes a correction for molecular anisotropy.

v) The scatterers must not have resonant frequencies near the frequency of the incident photon. For example, when the laser frequency of a lidar transmitter approaches the absorption line of an atmospheric constituent the scattering cross section is significantly enhanced [49]. This resonant scattering phenomenon is what allows lidars to determine atmospheric temperature in regions such as the sodium layer in the upper atmosphere.

When we consider a photon 'scattering' off an atom or particle what we are actually envisioning is an absorption and re-emission process. Imagine a molecule of nitrogen; it has a central nucleus and a cloud of electrons surrounding it. Each of these electrons has a defined energy associated with it. When a photon interacts with one of the electrons associated with the molecule it raises the energy level of the electron to a 'virtual state'. These virtual states are unstable arrangements and the electron quickly decays back to a lower energy state and emits a photon with the exact same wavelength at which it was stimulated.

It can be shown that the intensity of a scattered beam has both angular and wavelength dependence [34]. If a given molecule has a scattering cross section given by equation (1.23), where n is the index of refraction, k is the wave number, and N is the number density of scatters

per unit volume then we can define an expression equation (1.22) for the scattering intensity.

$$I(x) = I_0 e^{-\sigma N x} \quad (1.22)$$

$$\sigma = \frac{2k^4}{3\pi N^2} (1 - n^2) \quad (1.23)$$

This form can approximately be expressed in terms of the scattering intensity of linearly polarized light off a dielectric sphere as a function of scattering angle expressed in equation (1.24) where ϕ is the scattering angle and E_0 is the magnitude of the incident electric field.

$$I(\phi) \approx E_0^2 \frac{9\pi 2\epsilon_0 c}{2N^2 \lambda^4} \sin 2\phi \quad (1.24)$$

1.8.3 Raman Scattering

In contrast to Rayleigh scattering, Raman scattering is an inelastic process where a ray of monochromatic light scatters off a molecule at different wavelengths than the incident ray. This frequency shifting of scattered light happens when energy is transferred between the incident photon and the scatterer, in increments which are proportional to the quantized rotational and vibrational energy levels of the atom or molecule. Said another way: the scattered photon either gains energy from the interaction and shifts to a higher frequency, a process known as Stokes shift, or the scattered photon loses energy from the interaction and shifts to a lower frequency, a process known as anti-Stokes shift. Since our scattering targets of interest are mostly diatomic molecules we expect that there will be energy shift due to both the vibrational as well as rotational transitions. Figure 1.7 represents the Raman transitions with respect to the virtual state and the energy of the incident photon.

To characterize the possible energy states it is best to introduce two quantum numbers J and v . Beginning with the idea of Bohrs atom we imagine electron shells which have discrete energy levels. Combining two atoms together the allowable energy states become more numerous. There are vibrational states, J , and each vibrational state can have many rotational

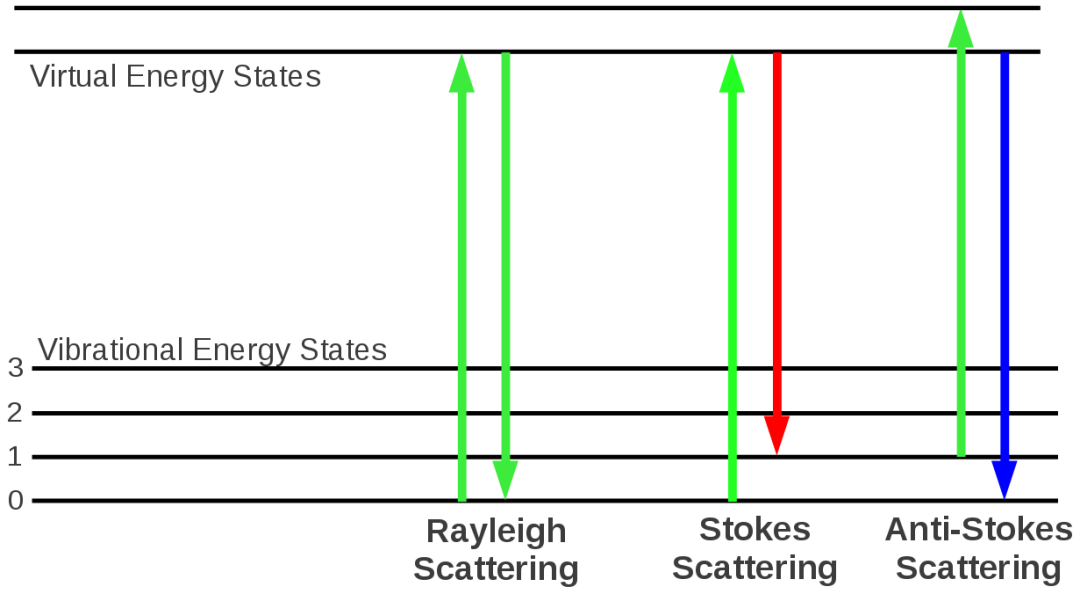


Figure 1.7: Stokes and anti-Stokes shifts with respect to Rayleigh scatter. PCL water vapour measurements rely on Stokes, or red-shifted Raman scatter from 532 nm.

sub-levels, v . For our purposes we will only allow $\Delta J = 0, \pm 2$ and $\Delta v = 0, \pm 1$ which are the allowable states of a diatomic molecule. A plot of three different Raman vibrational modes with their attendant rotational wings is shown in Figure 1.8.

For a given Raman spectrum we can define a central Q -branch transition where $\Delta J = 0$ and $\Delta v = \pm 1$. This spectral mode is associated with "pure" vibrational scattering and is analogous to the central Cabannes line discussed in the previous section on Rayleigh scattering. When $\Delta J = +2$ and $v = 0$ we enter a rotational side lobe known as the S-branch. The S-branch is the 'blue-shifted' or anti-Stokes wing of the spectrum. When $\Delta J = -2$ and $v = 0$ we enter the other rotational side lobe known as the O-branch also known as the 'red-shifted' or Stokes wing of the spectrum. Figure 1.9 shows a diagram of this nomenclature scheme.

It is important to specify that PCL only seeks to make measurements of the Q-branch of a Raman spectrum as these are pure vibrational lines. However, it is not possible to measure an infinitely thin spectral width. Therefore, PCL also measures the O- and S- branches of the desired spectra. Theoretically, this poses a problem as there is a temperature dependent asymmetry between the two side lobe branches. Algara-Siller examined this problem and

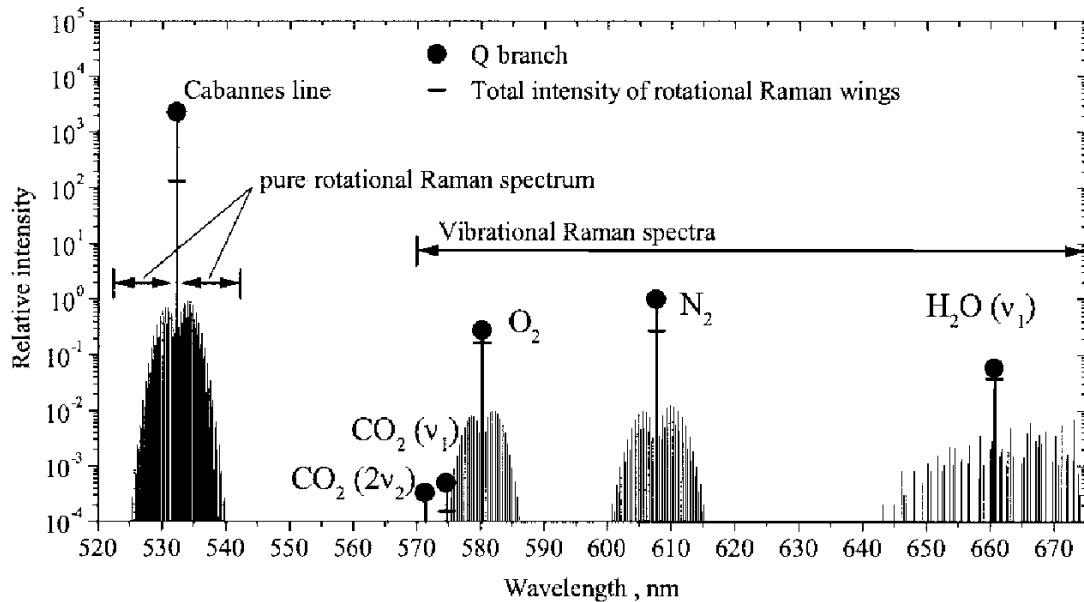


Figure 1.8: Energy transitions for vibrational and rotational Raman scattering. [3]

concluded that for the 1.11 nm filter in front of the PCL water channel there is a less than 5% variation over the temperature range of 293 K to 213 K. His results are shown in Figures 1.10 and 1.11.

In Figures 1.10 and 1.11 the dashed line represents the filter bandwidth while the Raman spectrum intensity is shown for two temperatures. At 293 K the filter fits the spectrum well and there is minimal loss. At 213 K the sum of the product of the spectrum intensity and transmission index is lower, indicating a poorer fit. Marcos Algara-Siller derived and applied the appropriate correction to PCL water retrievals based on radiosonde data [53].

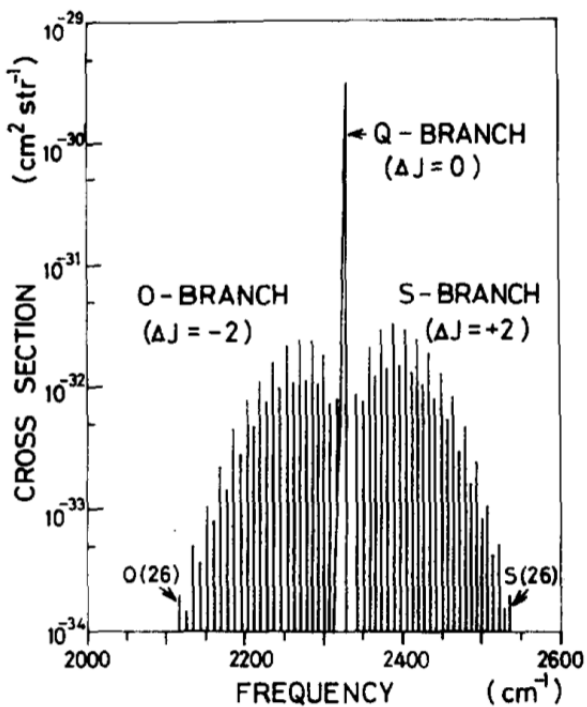


Figure 1.9: Raman scatter showing the O-branch, Q-branch, and S-branch.

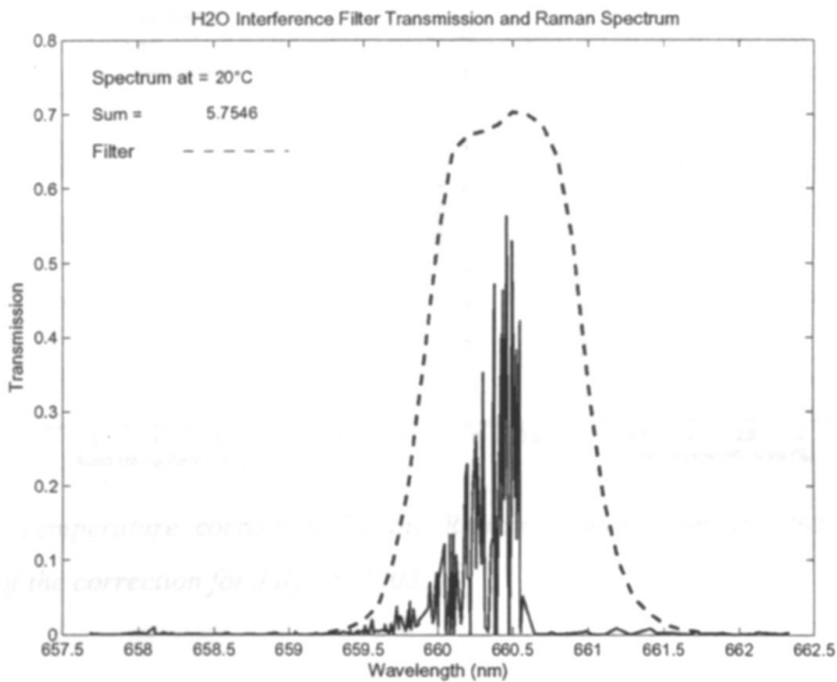


Figure 1.10: Water filter transmission at 293 K. [53]

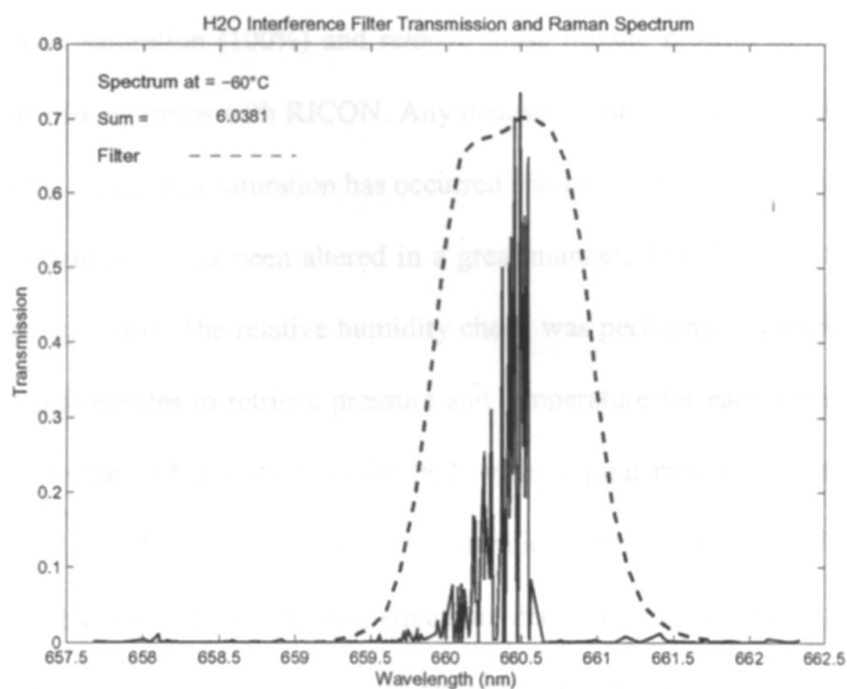


Figure 1.11: Water filter transmission at 213 K.[53]

Chapter 2

Lidar Instrumentation

2.1 Introduction

LIDAR is an optical remote sensing technique, analogous in concept to the radar or sonar, relying on pulsed visible or near visible frequency light to determine range and surface information for a target. The acronym LIDAR stands for LIght Detection And Ranging [15].

2.2 The Purple Crow Lidar History

The Purple Crow Lidar (PCL) was first constructed at Delaware Radio Observatory (42.52 N, 81.23 W, 225 m) in 1992 and was designed to measure temperature and dynamics in the middle atmosphere [51]. In order to take measurements of temperature in the upper mesosphere and lower thermosphere the PCL was designed as a high power-aperture Rayleigh lidar with a complementary sodium resonance-fluorescence system (589 nm) for measuring the temperature of the sodium layer [2].

In the late 1990s and early 2000s PCL started to focus on developing measurements of water vapour mixing-ratio in the lower and middle atmosphere. Early work done in the Master's theses of [10] and [53] allowed for the early calibration and validation of water vapour mixing-ratio by vibrational Raman lidar measurements. An overview of the initial PCL calibration for

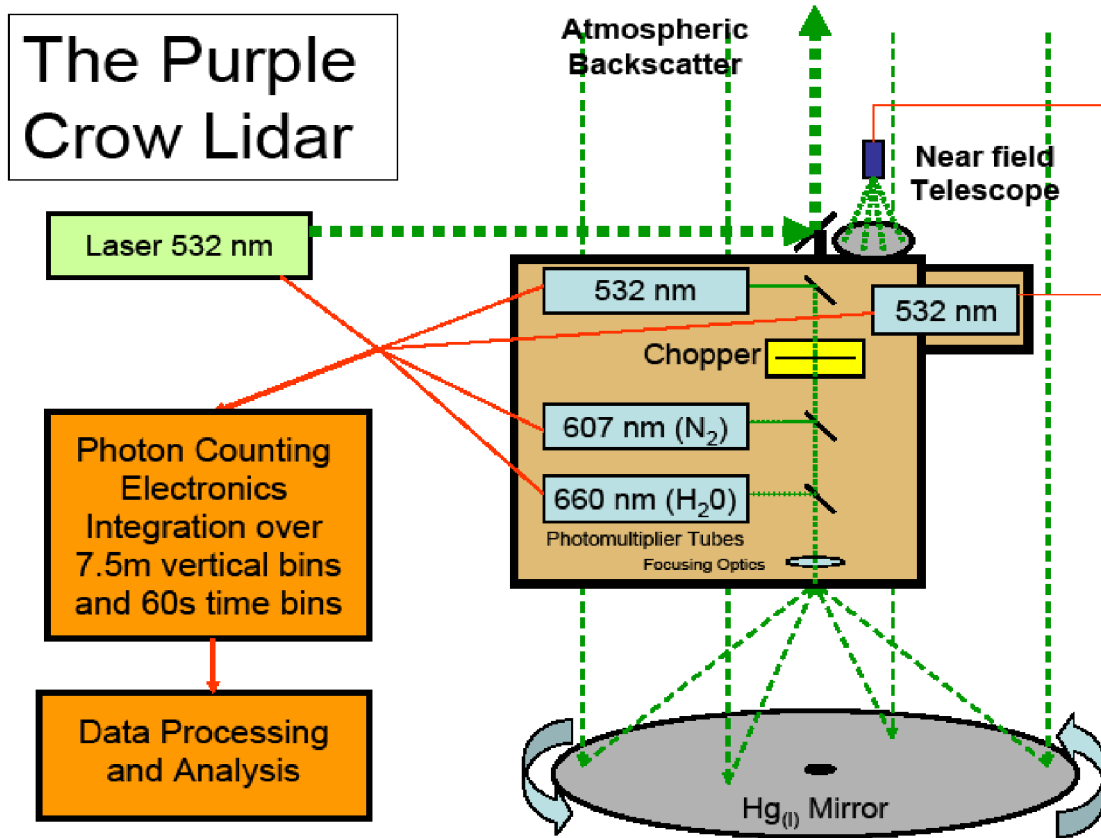


Figure 2.1: PCL schematic diagram containing Hg telescope and receiver system.

both water vapour mixing ratio and Raman temperatures using radiosondes from Detroit and Buffalo can be found in a paper by Argall et al. [1].

By the summer of 2010 the Delaware Observatory was no longer suitable for PCL and a new, custom-built observatory was made ready at the Environmental Science Western Field Station (43.07 N, 81.33 W, 275 m) (Ministry of Natural Resources 1983). The move provided an opportunity to update and rework PCL and the system received a new, more powerful, laser; new photomultiplier tubes; new, faster, counting electronics; new optics; an environmentally friendly geothermal cooling loop for laser temperature stability; and a low dew-point, ultra clean compressor which supplies air to the liquid mercury telescope. In addition to these upgrades the new site also offers better seeing conditions and is much closer to campus which allows for more routine observations. A schematic overview of the system can be found in figure 2.1.

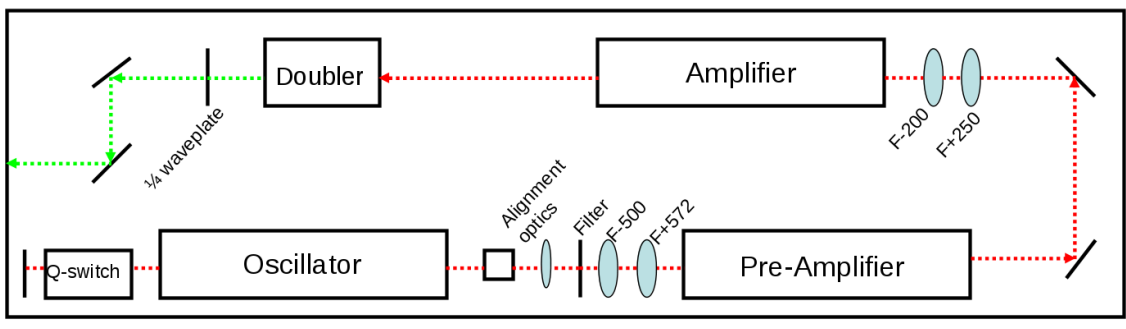


Figure 2.2: Schematic of the Litron LPY-7000 laser head.

2.3 PCL Sub-systems

The Purple Crow Lidar is a mono-static lidar system which was designed and assembled during the summers of 2010 and 2011 and became fully operational in early 2012. In essence, the PCL Observatory can be subdivided into three independent sub-systems which will be broadly labeled as: the Transmitter, the Receiver, and the Data Acquisition System. Each of these three systems will be described separately and the work that has been done in their creation and calibration will be detailed.

2.3.1 The Transmitter

The Laser head

The PCL uses the second harmonic of a Neodymium: Yttrium-Aluminium-Garnet (Nd:YAG) solid state laser to produce light at 532 nm. The laser itself is an experimental prototype which was designed and manufactured by a British company, Litron Lasers. An optical diagram is shown in Figure 2.2 as a visual reference for the following discussion on the characteristics, modifications, and operation of this device.

The unseeded, double rod, Gaussian oscillator outputs a 10 ns pulse of coherent 1064 nm light at a repetition rate of 30 Hz. The measured beam diameter at this point is 8.0 ± 0.5 mm when run on a fixed Q (time delay) and slightly larger when triggered by an internal Q-switch. The laser light upon exiting the oscillator passes through a set of primary collimation lenses

with *f*-numbers of $F - 500$ and $F + 572$, respectively, before entering the pre-amplifier.

The pre-amplifier contains two laser rods in a deionized water cooled cavity that is surrounded by two flash lamps in a parallel circuit. Separating the flash lamps from the laser rod cavity are broadband UV filters chosen to protect the laser rods from degradation caused by UV light in the lamp spectrum.

The pre-amplifier is followed by another set of collimating lenses with f-numbers of $F - 200$ and $F + 250$, and then by an amplifier which is an identical device to the pre-amplifier. At this point, the laser beam is still at 1064nm but the laser pulse energy has been increased to approximately 2500 mJ per pulse with a beam diameter approaching 10 mm. It is important to note that the position of the oscillator, pre-amplifier, and amplifier are not perfectly co-linear with the back trajectory of the beam path. The reason for this displaced layout is to introduce a small angular offset so that any back reflected laser light does not re-enter the previous stage of the laser and cause damage. To visualize this offset, imagine a very slight, almost indiscernible by the eye, lightning bolt-shape to the beam path.

After leaving the collimating lenses of the amplifier, the beam travels into the doubler. The doubler is an oven, in its original design heated to 40°C which contains a crystal of Potassium titanyl phosphate (KTiOPO_4). The doubling crystal is a solid state non-linear optic which converts incoming photons at 1064 nm into outgoing 532 nm photons.

Significant work was done, post installation, to modify the oven temperature in an effort to maintain a constant laser output. The work involved very slowly changing the temperature of the oven and correcting the phase of the crystal to compensate for thermal drift. This experiment was carried out over 72 hours and required shifts with fellow graduate students Emily McCullough and Jaya Khana. A new oven temperature of 50°C was selected which allowed the laser power to plateau at a stable value. A summary of the results is given in Figure 2.3. Since running the crystal at such a high temperature is not a good long term solution, Litron Lasers redesigned and installed a more sophisticated oven which aided in uniform and consistent crystal heating.

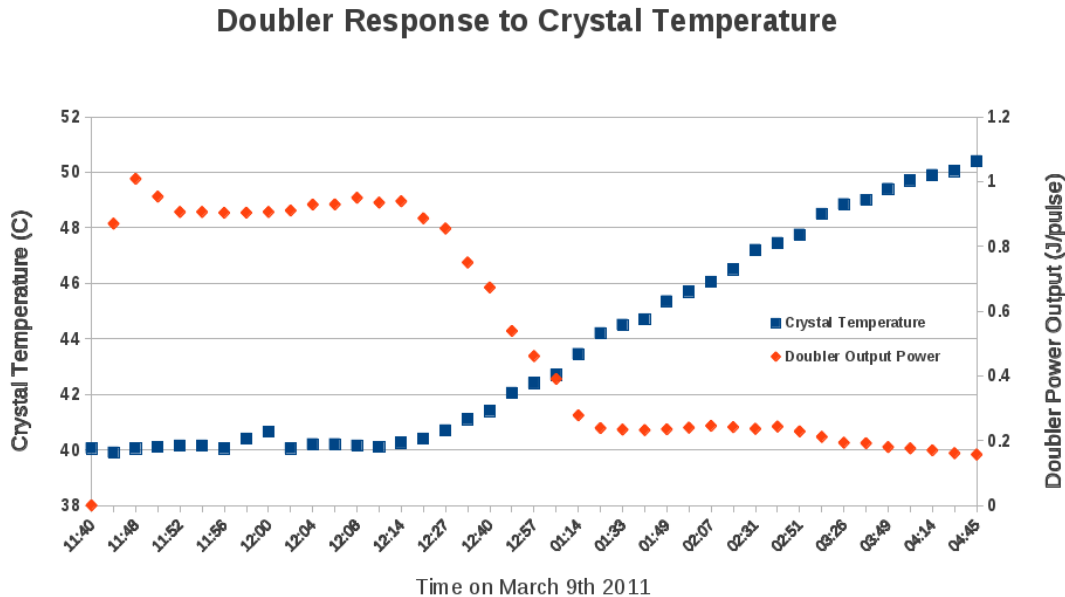


Figure 2.3: Effect of doubler crystal temperature on laser output power.

When the beam exits the doubler chamber the frequency of the light has been changed to 532 nm, the pulse length has been shortened to 8.0 ns, and the new beam diameter is 11 ± 1 mm. Power measurements of the laser output at this point yielded an average pulse energy of 970 ± 50 mJ, an energy density per pulse of $\sim 100 \frac{\text{MW}}{\text{cm}^2}$ and a specified divergence of 0.5 mrad.

The Laser Power Supply and Cooling

Due to the experimental nature of this laser, extensive testing and redesign work was required for the power supply and coolant systems. The laser assembly was measured to require a 40 A draw on a 240 V line, a significant amount of power. Given that most lasers have a less than 1% efficiency in the conversion of electrical energy to light [52] (calculated to be approximately 3% for our system) there is a significant amount of waste heat produced. This heat, calculated to be approximately 9600 W, must be efficiently removed from the laser head as variations in the temperature of many optical components like the laser rods and the doubling crystal affect their lensing properties. The system is designed to operate most efficiently between 18 °C and 25 °C [31]. Figure 2.4 shows how crucial temperature stability is to the operation of the laser.

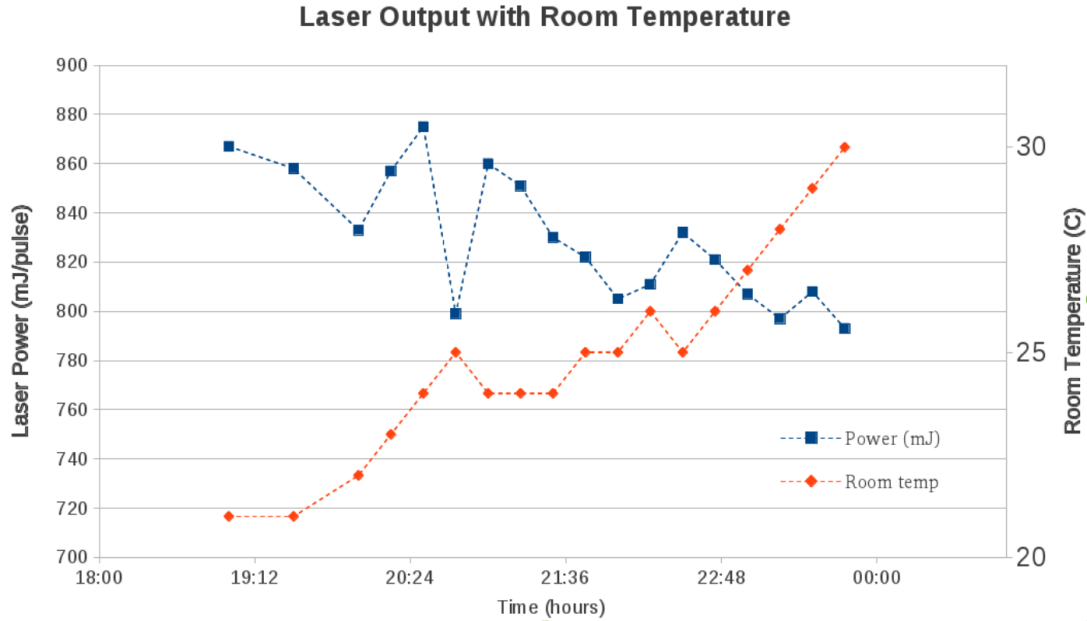


Figure 2.4: Effect of room temperature on laser output power.

Unfortunately, the initial design of both the laser and the PCL Observatory were not able to dissipate the heat produced in the system at a sufficient rate and the system overheated after about 30 minutes of use. It was decided that the laser required both a set of cooling fans mounted into the casing, which would draw air across the outside of the flash lamp casing, and a geothermal cooling system which couples with the laser's cooling system and dissipates the heat in 200 m underground loops. We worked out that the geothermal system was required to supply 8 L/minute at 30 PSI to the laser power supply which runs a cross-current circulation into a de-ionized water (DI) loop.

After addressing the concerns regarding the doubler crystal oven temperature, the laser output power stability, the electrical supply, and the heat dissipation, the laser manifested a tendency to produce irregular beam shapes. A normal beam shape is a tight Airy diffraction pattern with an energy density distribution related to the Fourier transform of the aperture. For a circular aperture of radius, R, equation (2.1) is the transform where $J_1(x)$ is a Bessel function of the first kind.

$$I(\theta) = I_0 \frac{2J_1(x)}{x^2} \quad (2.1)$$

$$x = kR \sin(\theta) \quad (2.2)$$

This pattern is expected in cases of Fraunhofer, or far field, diffraction. When a beam shape becomes irregular (in our case the asymmetry begins in the oscillator) there is a tendency to focus portions of the beam very near to the aperture, or Fresnel diffraction (less than 10 m). When this process occurs in the laser it develops what are called hot spots which are regions in the beam where the energy density spikes up due to intra-beam focusing.

When these hot spots occur over optics in the beam path they act to deposit energy into the material at a rate which is faster than the optic coating or underlying glass can thermally dissipate. At this point, chemistry becomes an issue as the specialized coatings on the optics oxidizes, rendering the component useless. As a relative measure of the intensity of the hot spots, the average central energy fluence of the laser is $110 \pm 10 \frac{\text{MW}}{\text{cm}^2}$ and the hot spot was able to burn through optical coating rated at $500 \frac{\text{MW}}{\text{cm}^2}$.

The beam hot spots in our system burned through several of the internal optics in the laser head, scorched the ends of the laser rods, burned the coatings off of the PCL beam expander (discussed in the next section), and made holes in a few of our old 532 nm laser line mirrors. After replacing all the damaged components, the laser technicians from Litron and I developed a procedure to damp out the hot spots by deliberately misaligning the laser and reducing the overall output power.

There are two main ways to modulate laser power: the first and most simple way is to change the voltage that the system puts across the flash lamps. Thinking back to the laser chamber, we see a simple system where the potential across the lamps induce a greater response, which pumps more energy into the laser rods, which in turn increases the total laser power output. Changing the voltage across the flash lamps is a very common technique for

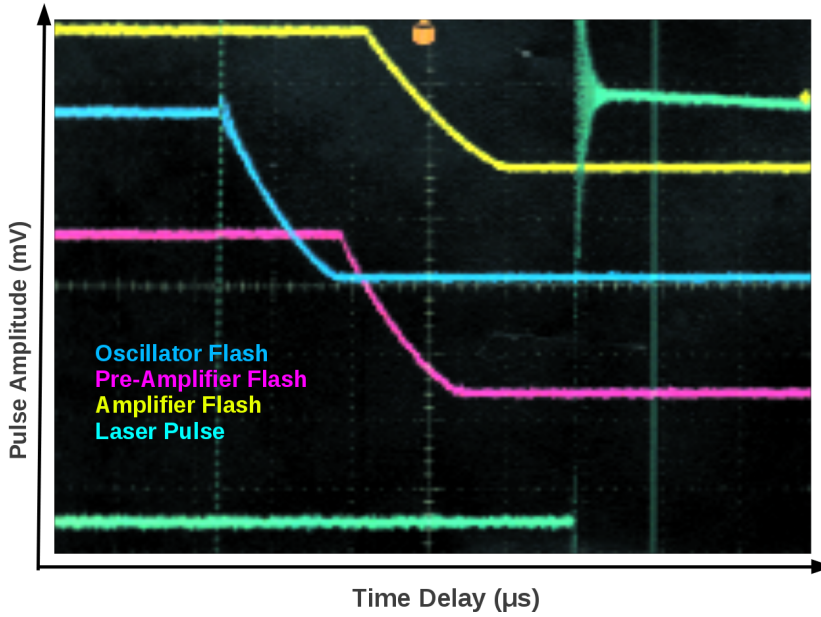


Figure 2.5: The output power of the laser can be modulated by varying the delay between triggering of the Oscillator (blue), Pre-amplifier (magenta), and Amplifier (yellow). The time delay of the emitted pulse is shown in green. [31]

maintaining a consistent flash as the bulbs degrade and discolour over time.

The second part of the method for modulating the laser output is to adjust the pulse delay across the laser head. Referring back to Figure 2.2, we see that each of the three pumping chambers (the oscillator, pre-amplifier, and amplifier) and the Q-switch are precisely positioned in the laser head. Given that light travels at the speed of light, c , and that the laser must output 30 pulses per second, it is important that each of the pumping chambers and the Q-switch are properly synchronized. When a pulse originates in the oscillator and then travels to the pre-amplifier the delay on the pre-amplifier must be set so that it adds energy to the pulse in phase. The same must hold with the pulses coming to the amplifier and Q-switch. Figure 2.5 is from the laser manual and gives an illustrative picture of this delay between pulse generation and pulse output across the system [31]. By introducing an offset in the pulse delay between the Q-switch and the outgoing pulse, the energy of the system is damped and the change in the lasing temperature of the rods helps to minimize the hot spots. To compensate for changing the lasing temperature of the rods we alter the voltage across the flash lamps and adjust the angle

of the doubling crystal. Dr. Steve Argall built a small switch controlled potentiometer which allows me to change the delay in real time while the system is operational. Without this device it would be too dangerous to conduct this procedure. Balancing the timing delay, voltage, and crystal angle has allowed me to maintain a relatively constant output of 600 mJ per pulse on the system. This reduced, but stable, output was sufficient for PCL to participate in a calibration experiment with NASA GFSCs ALVICE lidar (described in Chapter 4). It is important to note that this quick fix has a number of problems which must be addressed:

- 1) The hot spots are only minimized, not eliminated. They will likely continue to degrade the internal optics of the laser over time.
- 2) The procedure to balance the pulse delay, voltage and crystal phase is a very delicate and non-trivial procedure where experience with this particular laser and intuition are valuable. When the potential or pulse delay is changed the local heating on the laser rods also changes which alters their lensing properties. If care is not taken in this procedure the flash lamps can explode, the beam shape can become distorted, or the doubler crystal can burn.
- 3) There is a finite length of time that this method can be employed before the corrections to the pulse delay become of the order of the pulse separation. Fortunately, the laser has gone back to the Litron factory for a redesign and rebuild of the oscillator which should hopefully correct the beam defect.

The Beam Expander

After the beam leaves the laser head, it passes through a pair of lenses to expand the beam in an effort to minimize the beam divergence of 0.5 mrad. The original beam expander was designed by Dr. Argall and was composed of a pair of lenses mounted in a set of optical stands. Unfortunately, these optics were destroyed by hot spots in the beam. Upon closer examination of the outgoing laser beam it was discovered that the beam divergence was larger than specified by the manufacturer.

To accommodate the high photon fluence and larger beam divergence a Galilean telescope

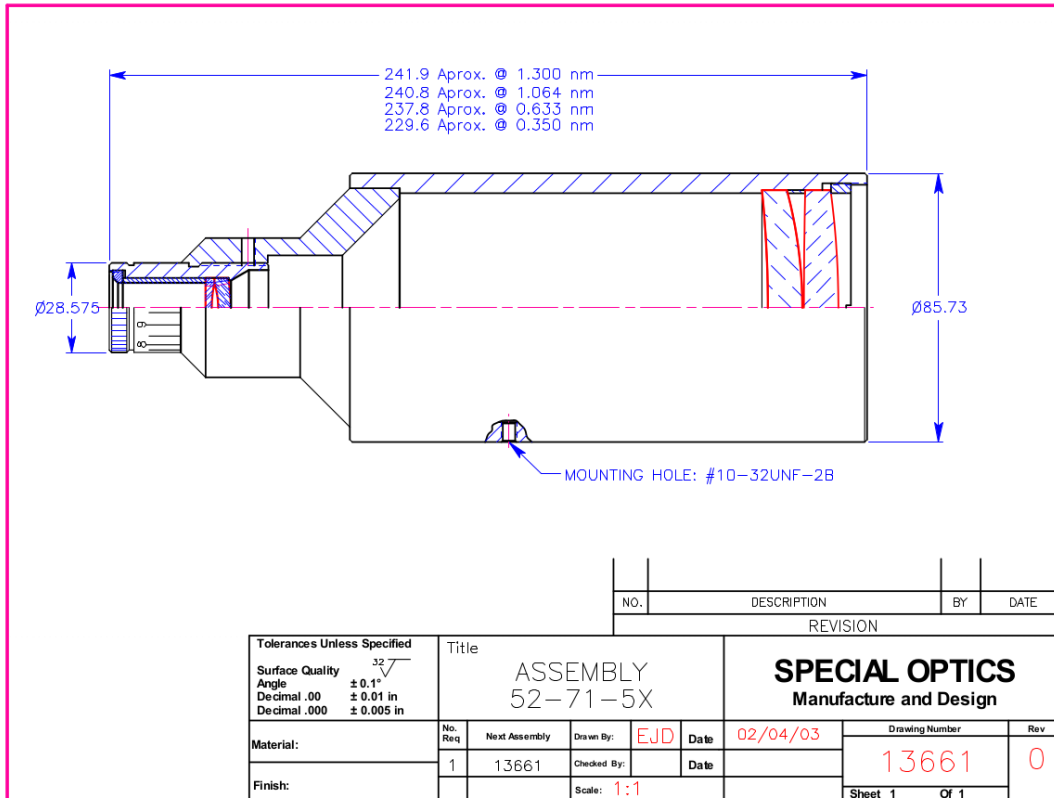


Figure 2.6: Schematic of beam expander. [60]

was purchased from Special Optics the specifications of which are given in figure 2.6. This new set up expands the beam from a diameter of 12 mm with a divergence greater than 0.5 mrad to a 600 mm beam with a divergence less than 87 μ rad. An étalon was used to ensure proper collimation of the outgoing laser beam.

Beam expanders work to reduce the beam divergence in the far field by increasing the final aperture size of the terminal optic. Assume a setup as shown in figure 2.7 where D_0 is the optic aperture or beam waist, θ is the beam divergence, x is a suitably far distance from the aperture such that near field optical effects are no longer dominant, and $D(x)$ is the diameter of the beam at distance x . Diffraction is the spreading of light which is emitted from a finite source and it makes beam collimation impossible. As the laser beam exits the aperture secondary waves arise from the characteristics of the edges of the optic. These secondary waves interfere with the primary wave to create the diffraction pattern.

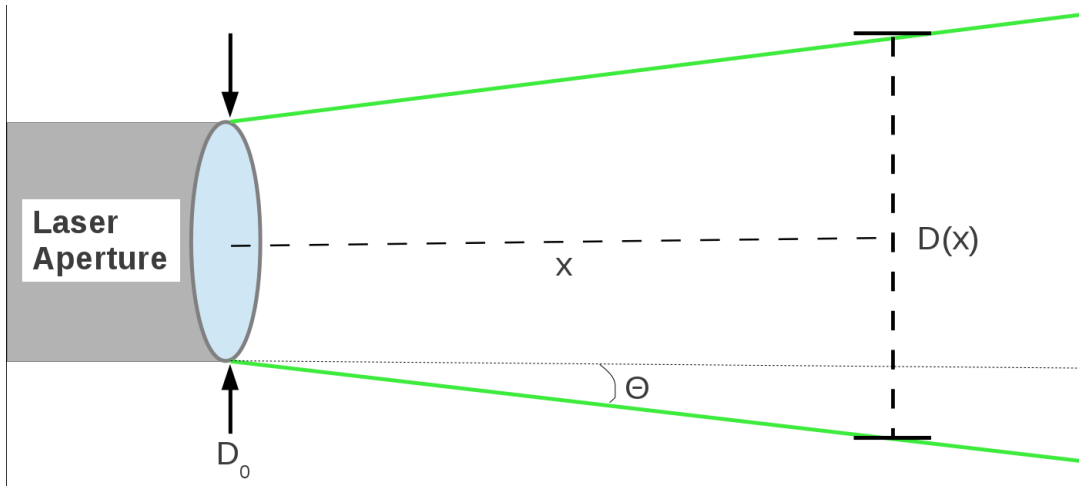


Figure 2.7: Depiction of far field divergence from a laser aperture or terminal optic.

The spreading of the beam can be expressed by equation (2.3) where

$$D(x) = D_0 \sqrt{1 + \left(\frac{\lambda x}{\pi S_0^2}\right)^2} \quad (2.3)$$

$$S(x) \approx \frac{\lambda x}{\pi S_0}. \quad (2.4)$$

$$\theta = \frac{S(x)}{x} \approx \frac{\lambda}{\pi S_0} \quad (2.5)$$

λ is the laser wave length. If $\frac{\lambda x}{\pi S_0^2} \gg 1$, which is the case for the far field where x can be large, then equation (2.3) can be approximated by equation (2.4). Then using some trigonometry, the divergence angle θ can be approximated by equation (2.5). As can be seen, there is an inverse relationship between the beam width and the far field divergence, therefore expanding the Gaussian laser beam through a Galilean telescope acts to tighten the beam. [18] Having a small beam size is important for lidar studies and will be discussed later in this chapter.

The Optical Path

The collimated beam travels through 13.418 m and reflects off three 2.5 inch laser line mirrors on its way to the sky. Figure 2.8 gives a sketch of the beam path. The final mirror, mounted

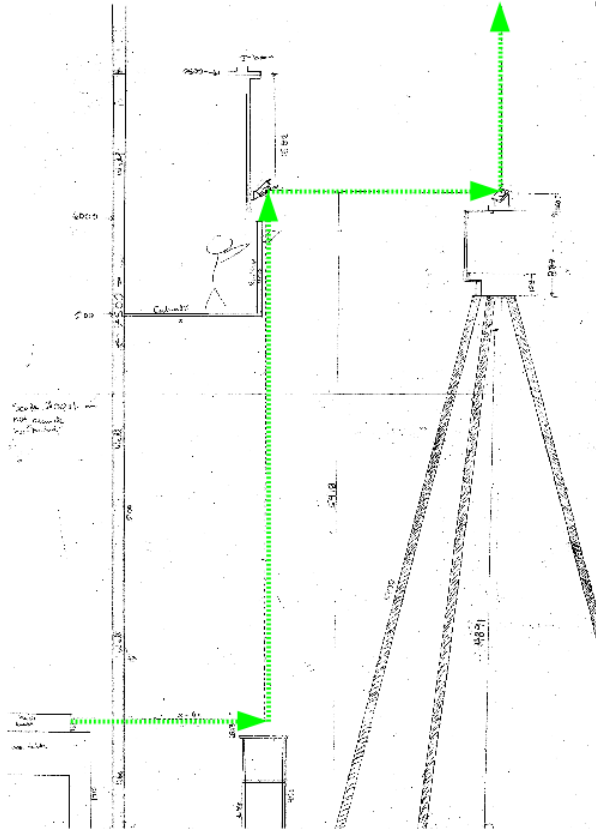


Figure 2.8: Original blueprint for the PCL optical transmission path.

on top of the detector box, is a commercial motorized mirror mount. This mount is computer controlled to tilt the laser beam in the sky for optimal alignment.

2.3.2 The Receiver

The Liquid Mercury Telescope

The primary receiving optic for the PCL is a mirror made from a rotating dish of liquid mercury. The initial design of the liquid mercury telescope was done by Prof. Ermanno Borra and colleagues at the Université Laval [7] and [8] and it was built with the expertise of Prof. P. Hickson (UBC). The advantage to using a liquid mirror telescope in lidar studies is that it allows for a relatively large, relatively inexpensive, alternative to a glass mirror. An added advantage of this design is that it is a simple matter to resurface the mirror to remove dust and

Telescope Specifications	
Focal Length	5.175 m
Field of View	0.39 mrad
Rotation Period	6.330 s
Reflectivity	79%
Volume of Hg	8 L
Aperture	2.44 m

Table 2.1: Optical specifications for the liquid mercury telescope.

debris or in the case that something is dropped on the surface. The optical specifications for the PCL telescope are given in table 2.1. The theory behind this telescope design is quite simple; a cylindrical dish with a near parabolic bottom is partially filled with a volume of mercury. The dish is then rotated at some angular frequency, ω , about a central axis which is parallel to the gravity vector, g . The fluid moves in such a way that the acceleration of the dish balances the gravitational force on each fluid parcel, resulting in a stationary parabolic mirror in the reference frame of the dish. It can be shown that the focal length of this parabola, f , is equal to (2.6). This means that we can adapt the focal length of our telescope by varying the speed at which the dish rotates by way of a small electric motor.

$$f = \frac{g}{2\omega^2} \quad (2.6)$$

This ability to adjust the focal length as seen in figure 2.9 is very useful for our work as the equipment is exposed to ambient temperatures and, thus, experiences thermally induced expansions and contractions over the course of a night and a season. In practice, this liquid mirror technology can be fairly challenging to perfect and requires significant effort to precisely align and balance. However, once a near perfect balance has been achieved, the system will run continuously for months at a time. There are three primary components of the liquid mirror telescope: the air bearing system, the braking system, and the dish. Each of these three systems will be described separately and the work that I have done in their creation and calibration will be detailed. A picture of the entire system is given in figure 2.10 from [8].

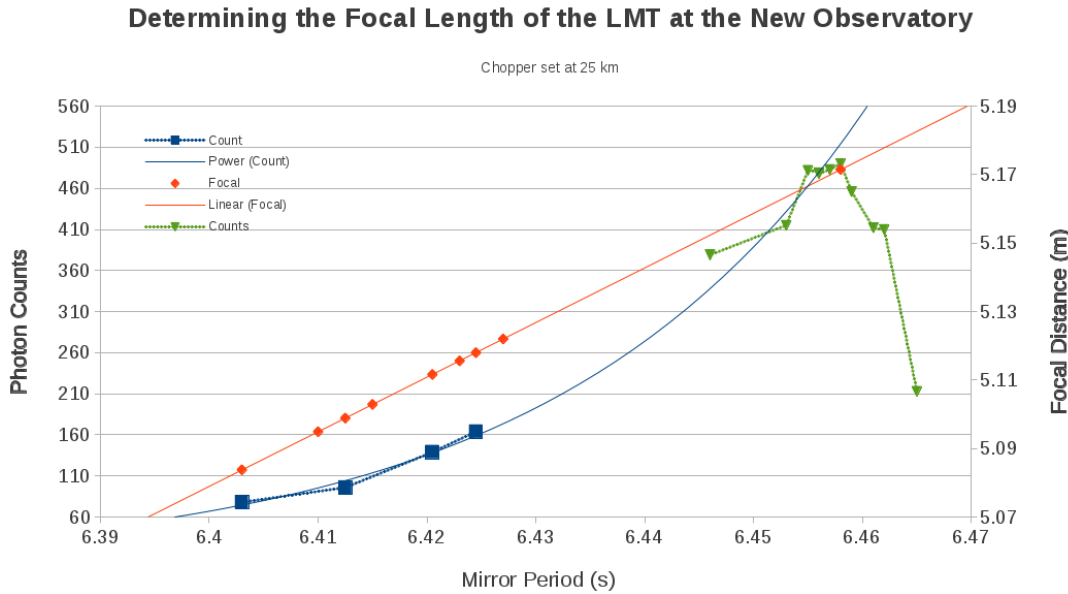


Figure 2.9: Confirming the focal length of the liquid mercury telescope is 5.175 m. The red line represents measurements of the height in meters above the surface of the mirror. The blue curve is a fit to the count rates measured by the detector system while the mirror is rotating slowly. The green points are the count rates measured by the detector system while the mirror is rotating quickly. The mirror is unstable between the blue and green curves.

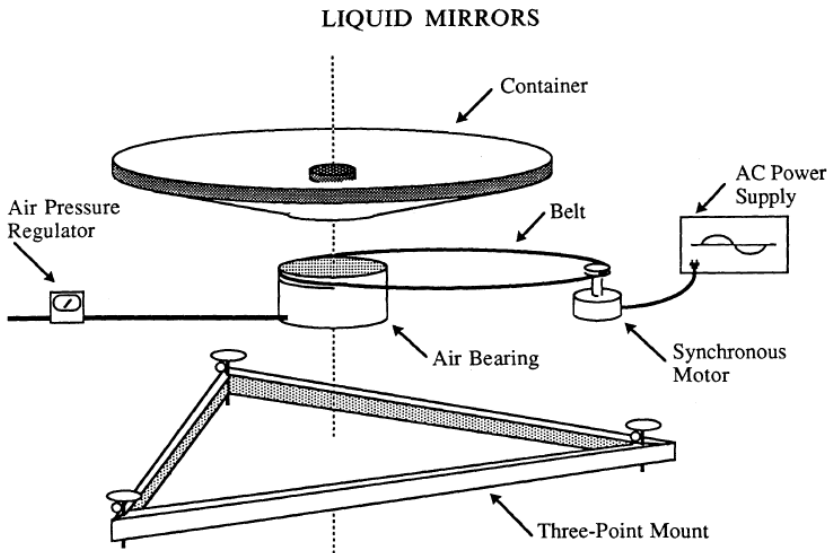


Figure 2.10: Schematic of the liquid mercury telescope from Borra et al. (1992). [8]

The Air Bearing and Breaking System

The most challenging subsystem of the PCL liquid mercury telescope is the pneumatic bearing which floats the mirror dish. To supply the air bearing with a sufficiently dry source of air, an oil free compressor, a series of desiccant filters, particulate filters, a pressure tank, pressure regulators, and a dew point hygrometer were installed. The pneumatic subsystem supplies a consistent 80 psi of air that is clean of particulates or hydrocarbons greater than half a micron, and has a dew point below 213 K. The hygrometer draws a small amount of air off the main line and passes it over a hygroscopic wire. The resistance of the wire changes based on the water content of the air and a measure of the current is displayed on a digital readout. A dew point conversion chart for air was calculated using a factory supplied correction curve and is posted for reference on the wall near the hygrometer. A PCL user should check the hygrometer read out prior to running the liquid mirror telescope and ensure that the dew point is within tolerances.

The braking and safety system for the PCL was upgraded and adapted from components used in the old system which was active at Delaware. The system has been wired so that brakes will be applied to the mirror dish should any of the following criteria be met:

1. The power fails in the building
2. The pressure in the air bearing falls below 70 psi or exceeds 90 psi
3. The electric mirror motor stops or the drive belt breaks
4. The frequency generator for the mirror power supply is shut off
5. The hygrometer measures too much current (still to be wired)

These measures are in place to protect the air bearing and to prevent the dish from rotating too quickly or becoming unsteady. However, should the mirror dish begin to wobble on the air bearing (the dish is hit or the mercury surface tension breaks in an asymmetrical fashion),

there are a series of 8 spill wheels under the mirror to prevent it from tipping. These wheels are mounted on posts which are placed approximately half a millimeter under the rim of the mirror dish. Each post is bolted to the floor in an octagonal fashion, with a post every 45 degrees.

The Dish

The dish of the liquid mercury telescope must be very precisely balanced on the air bearing so that the rotation axis of the dish is aligned with the gravity vector. An engineer's spirit level was used to level the air bearing and the dish to better than 1 part in 10000. The next step after levelling the plane of the dish is to flex the dish into the proper shape. Since the layer of mercury which covers the surface of the dish can be as thin as a few millimetres it is important to minimize any peaks or troughs over the rubber surface of the dish. To flex the dish without unbalancing it is a very delicate procedure. Lead weights are placed on the rim of the dish near regions where the dish has flexed upwards and shims, consisting of single pieces of aluminium foil, are placed between the air bearing and the base of the dish near regions where the dish flexes downwards. The final results are shown in figure 2.11, where the red triangles represent the placement of weights, the green squares shims, and the blue diamonds are measurements of relative elevation from a fixed engineer's clock.

Now that the final surface of the liquid mercury telescope dish is levelled and flattened to better than 0.5 mm over the 2.44 m diameter span of the dish, the telescope should have a field of view equal to 0.39 mrad [8]. Recall that an étalon was used to collimate the outgoing laser beam to approximately 87 μ rad. It is important to check that the spot size of the laser is less than the field of view for the telescope.

Using the angular mil approximation which allows $\sin(\theta) \approx \theta$, the angular divergence of the laser beam in milliradians, θ , can be related to the target range, d , and target radius, r using equation (2.7).

$$d(m) \approx \frac{r(mm)}{\theta} \quad (2.7)$$

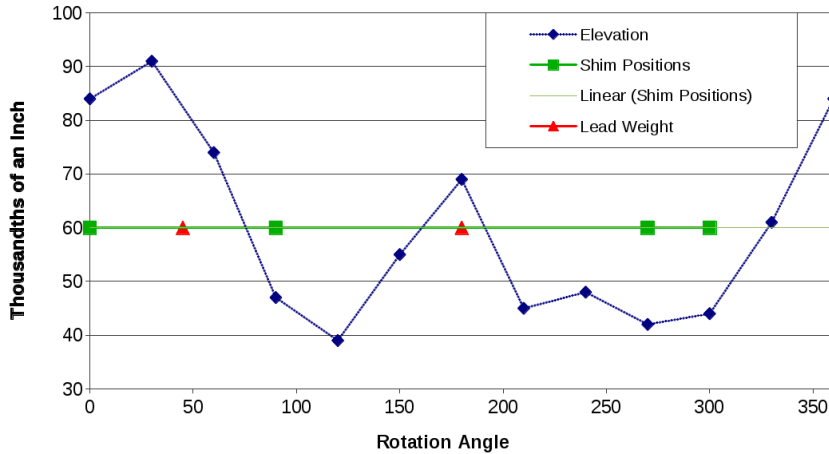


Figure 2.11: A plot which describes the leveling of the surface of the telescope dish. Green squares represent shims placed under the base of the mirror, red triangles represent lead weights hung from the rim of the mirror, blue diamonds are mirror surface height measurements made from a mounted engineer's clock. The mirror is leveled to better than 1:5000.

At 100 km the field of view of the telescope has a diameter of 78 m and the collimated beam has a spot size of with a diameter of approximately 18 m. The spot size is sufficiently small compared to the field of view for the telescope.

The Detector Box

The PCL move afforded an opportunity to rework the detector system which is mounted above the liquid mercury telescope. In the past PCL has made measurements of the sodium layer [2] however, this system was removed to make room for upgrades. A schematic of the detector box can be seen in figure 2.12. The old photomultipling tube (PMT) for sodium was replaced by a R9880-20 Hamamatsu PMT and is now PCL's new Rayleigh channel (labelled Rayleigh Licel). As well the old nitrogen channel was refitted with a similar PMT (labelled Raman N₂ Licel). The old Rayleigh channel (labelled Rayleigh Hamamatsu) was adapted to become a calibration and alignment channel for use in testing the linearity of the new Licel system as well as for use as a nightly system alignment check. After the box optics were cleaned and reorganized to account for the new optical paths, a new high-voltage power system was wired in and the PMTs were calibrated for linearity and best signal.

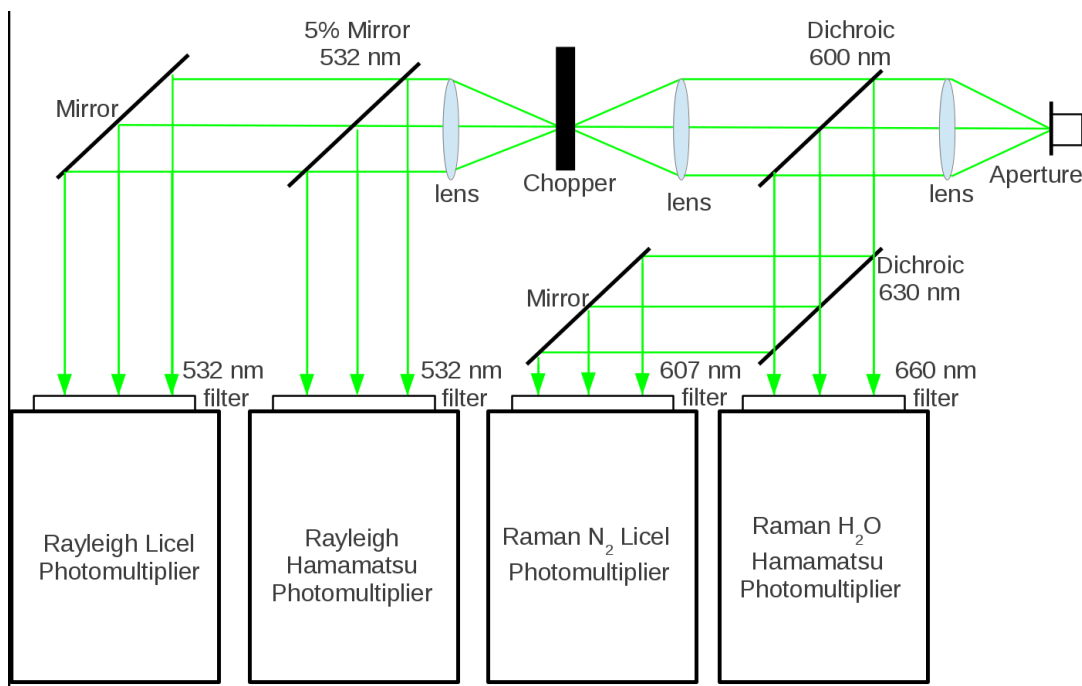


Figure 2.12: A schematic of the reworked PCL detector box. Adapted from [10]

Chapter 3

LIDAR Data Acquisition and Processing

3.1 Introduction

The goal of this work is to accurately measure the water vapour mixing ratio of the atmosphere using Raman lidar techniques. Our measured quantity is back-scattered photons from the laser beam. We can further divide these photons according to their Raman shifted frequencies from a doubled YAG at 532 nm, 660 nm for water vapour and 607 nm for molecular nitrogen. This chapter details the techniques used to ratio these two signals to arrive at a value which is proportional to water vapour mixing ratio.

3.2 The LIDAR Equation

Back-scattered photons are collected and counted by PCL detectors. The number of photons collected can be expressed by the lidar equation (3.1) as given by Measures [34]:

$$N(z) = \xi_{sys} \cdot \tau_{emitted}(z, \lambda) \tau_{return}(z, \lambda) \cdot O(z) \frac{P_{laser}}{\frac{hc}{\lambda_{laser}}} \cdot \sigma n(z) \cdot \frac{A}{4\pi z^2} \cdot \Delta t \cdot \Delta z + B \quad (3.1)$$

N is the number of returned photons which are detected

z is altitude above the detector

ξ_{sys} is the system-specific receiver efficiency

$\tau_{emitted}(z, \lambda)$ is the transmittance of the photons through the atmosphere

$\tau_{return}(z, \lambda)$ is the return transmittance of the photons through the atmosphere

$O(z)$ is the overlap function of the receiver field of view

$P_{laser}/\frac{hc}{\lambda_{laser}}$ is the laser power

σ is the scattering cross section of the target

$n(z)$ is the number density of scatterers in the atmosphere

$A/4\pi z^2$ is the effective area of the primary telescope

Δt is the temporal integration for data collection

Δz is the spatial range over which photons in a bin are integrated

B is the background count rate.

The general form of the above equation holds true for any kind of lidar scattering processes. There may be further complexities introduced depending on the particular lidar system or application but those equations all share this general form. Care must be taken when doing Raman scattering experiments as the frequencies of the transmitted and returned photons are different and have different transmittance functions and scattering properties.

There are three simple assumptions we make when equation (3.1) is used. First, we assume that each photon we count only scatters once. While this is almost certainly not the case, we can say that it is approximately true. Visual wavelength photons have a very low probability of back-scattering in the atmosphere and when we have a multiple-scatter process we must square that very small probability. Therefore, for the purposes of this work it is an acceptable assumption that there is only single scattering.

Second, we assume that the laser pulse length is shorter than the recording time in an altitude bin. For PCL the laser pulse length is 9 ns and the bin duration is 0.8 μ s. There is approximately an order of magnitude difference so we can safely say that a particular bin is not receiving photons from multiple laser pulses.

Third, we assume that the returned photons are proportional to the number of scatterers in

the atmosphere and that the local number density of scatterers within a particular bin width is constant. Our bin duration for vibrational nitrogen returns is 7.5 m and for vibrational water vapour is 24 m. Recalling our scale height of the atmosphere (1.4) we are fairly safe in assuming that the number density of nitrogen molecules is constant over this range. However, water vapour can change very rapidly with changing altitude and temperature so we may miss features which are thinner than 24 m. Previous water vapour measurements made by PCL occurred at 250 m resolution and the most recent upgrade has improved the resolution to 6 m.

3.3 The Water Vapour Mixing Ratio Equation

One method of retrieving water vapour mixing ratio from Raman lidar measurements is to ratio the returns from a channel which detects back scatter from water vapour and from another channel which detects back scatter from a tracer of atmospheric density. In this experiment we transmit at 532 nm and expect that Raman-shifted nitrogen at 607 nm is a proxy for total atmospheric density and that Raman-shifted water vapour at 660 nm is a measure of water vapour content in the atmosphere. It then follows that calculating a ratio of these two signals, obtained from independent retrievals of equation (3.1) at the respective wavelengths, should provide a result which is proportional to the number density of water over the total atmospheric number density and lead to equation (3.2).

$$w_{number} = C(z, \lambda_1, \lambda_2) \cdot \frac{N_{N_2}}{N_{H_2O}} \quad (3.2)$$

The constant $C(z, \lambda_1, \lambda_2)$ can be decomposed into terms which relate the molecular and optical properties of both scattering species and systematic corrections. Equation (3.3) has been adapted from work done by Dr. D.N. Whiteman [73]. Note that since the system parameters are identical and the scattering in both channels come from the same atmosphere, the following terms in equation (3.1) cancel out: $O(z)$, the overlap function provided there are no wavelength dependent effects, $\frac{P_{laser}}{\lambda_{laser}}$ the laser power, $\frac{A}{4\pi z^2}$ the area of the telescope, Δt the data collection

Parameter	Value	Reference
$\frac{\sigma_{N_2}}{\sigma_{H_2O}}$	6.8	[48] at 515 nm
M_{dryair}	28.88 $\frac{g}{mol}$	[30]
M_{H_2O}	18.02 $\frac{g}{mol}$	[30]
$\frac{\phi_{N_2}}{\phi_{dryair}}$	78.08%	[30]

Table 3.1: Water vapour mixing ratio equation atmospheric parameters.

time, Δz , the vertical data binning.

$$w_{mass} = \xi_{sys} \cdot \Xi_{sys}(z) \cdot \Delta\omega(z, \lambda_1, \lambda_2) \cdot \frac{k_{N_2}}{k_{H_2O}} \cdot \frac{\sigma_{N_2}}{\sigma_{H_2O}} \cdot \frac{M_{H_2O}}{M_{dryair}} \cdot \frac{\phi_{N_2}}{\phi_{dryair}} \cdot \frac{N_{N_2}}{N_{H_2O}} \quad (3.3)$$

w_{mass} is the water vapour mass mixing ratio,

ξ_{sys} is the system specific calibration factor,

$\Xi_{sys}(z)$ is the system specific correction vector,

$\Delta\omega(z, \lambda_1, \lambda_2)$ is a differential transmission correction,

$\frac{k_{N_2}}{k_{H_2O}}$ is the ratio of the optical efficiencies in each detection channel,

$\frac{\sigma_{N_2}}{\sigma_{H_2O}}$ is the ratio of the back scatter cross sections,

$\frac{M_{H_2O}}{M_{dryair}}$ is the ratio of the molar masses for each atmospheric species,

$\frac{\phi_{N_2}}{\phi_{dryair}}$ is the molecular mixing ratio,

$\frac{N_{H_2O}}{N_{N_2}}$ is the ratio of the number of back scattered photons detected by the receiver,

Atmospheric Terms

A correction for the differential transmission of 607 nm light and 660 nm light through the atmosphere must be identified; the back scatter cross sections, molar masses, and mixing ratios for N_2 and H_2O as variables independent of the lidar must be determined from laboratory measurements or models. It is important to note that the back scatter cross sections obtained from Schrotter et al. 1979 [48] have very large uncertainties associated with them. The values we have chosen to use and their references are given in table 3.1.

The differential transmission term, $\Delta\omega(z, \lambda_1, \lambda_2)$, is calculated from an online version of the

Reflectivity		Reference
Hg Mirror	79%	[7]
Each Lens Surface	5%	estimate
600 nm Dichroic	7%	[57]
630 nm Dichroic	10%	[57]
607 nm Mirror	100%	estimate
660.3 \pm 0.6 nm Bandpass Filter	7%	estimate [43]
607.3 \pm 7.5 nm Bandpass Filter	5%	[43]

Table 3.2: Reflectivity of PCL detector box optics.

MODTRAN 3 model [4]. The original PCL retrieval algorithm for Delaware Radar Tracking Station assumed a rural aerosol loaded model. The assumption has been maintained at the new location at the UWO Environmental Field Station.

System-specific Terms

The remaining terms in the correction factor are system specific and are related to the particular optical experimental layout of the PCL. The first term, $\frac{k_{N_2}}{k_{H_2O}}$, describes the efficiency with which light travels through our detection system, as seen in figure 2.12, and is converted into electrical signals at the photomultiplier tubes. This term can be re-expressed in terms of transmission efficiencies and photo-conversion efficiencies in equation (3.4)

$$\frac{k_{N_2}}{k_{H_2O}} = \tau \cdot \frac{\Phi_{607}}{\Phi_{660}} \quad (3.4)$$

where τ is the light transmission through the receiver system and Φ is the efficiency of the photon detection in the photomultipling tubes (PMTs). The system transmission can be found by adding the logarithms of each of the values in table 3.2.

The quantum efficiency of the PMTs, Φ , are specified by the manufacturer. The sensitivity of the Licel R9880-20 PMT to 607 nm light is 79 $\frac{mA}{W}$ which corresponds to a conversion efficiency of $\Phi_{607}=16.1\%$ [54]. Unfortunately, the PMT we use for 660 nm, the Hamamatsu R5600P-01, was discontinued 12 years ago. The best estimates by their in-house engineers put

the quantum efficiency for 660 nm at $\Phi_{660}=2.9\%$ [55].

Calibration and Correction Terms

The final two components of our constant, C , are calibration constants. ξ_{sys} will represent a height independent scalar factor, of order unity, which will scale our remote sensing lidar retrievals to in-situ measurements. $\Xi_{sys}(z)$ is a term which is applied to correct for achromatic transmission of light through our systems, geometric overlap problems in the near field, and height dependent non-linearities in our count profiles. These two factors can only be obtained by way of a calibration campaign which will be the subject of the next chapter.

Chapter 4

Purple Crow Lidar Calibration

4.1 Introduction

The calibration of the PCL requires that the system constant ξ_{sys} and any system corrections $\Xi_{sys}(z)$ be quantified and integrated into standard data processing. This calibration scheme follows the method of the three MOHAVE (Measurements of Humidity in the Atmosphere and Validation Experiments) campaigns in 2006, 2007 and 2009 [29], [28], and [33]. In general, the remote sensing instrument(s) to be validated are co-located and a series of in-situ measurements are taken with which the remote instruments can derive a calibration factor.

4.2 NDACC Requirements

The Network for the Detection of Atmospheric Composition Change (NDACC) is an atmospheric research network with a set of globally distributed and certified research stations [56]. The goal of this network is to collect calibrated and validated measurements of atmospheric parameters and integrate these measurements into a common database. A common, high quality, database is essential for detecting changes and trends in atmospheric composition particularly in the troposphere and stratosphere. To this end PCL was targeted as an ideal candidate for the data assimilation of both atmospheric temperature and UTLS water vapour [71].

In order to properly certify PCL measurements of water vapour mixing ratio, a blind instrument inter-comparison is required with one of the NDACC mobile lidar systems. The instruments must be co-located for the duration of the campaign and be compared against in-situ measurements to determine a system constant [71].

4.3 PCL-ALVICE Calibration Campaign

In order to determine the system calibration factor, ξ_{sys} , for the new PCL Observatory a calibration campaign was organized with the Raman Lidar Group at NASA Goddard Flight Center. A mobile trailer containing the Atmospheric Lidar for Validation/Interagency Collaboration and Education (ALVICE) was shipped to London along with a science team for a month-long calibration campaign.

ALVICE and PCL were co-located for the duration of the campaign and radiosondes were launched to provide an in situ measurement as the basis for the calibration. The measurement portion of the campaign took place between May 23rd and June 10th 2012 and resulted in measurements from 18 RS92 radiosondes; 3 cryogenic frost point hygrometers (CFH); 57h 38min of lidar data over 12 nights taken by ALVICE as well as 15h of white light calibrations; 52h 57min of lidar data over 12 nights taken by PCL as well as 3h of white light calibrations. Table 4.1 details the particulars of the campaign.

4.4 Radiosondes

In order to validate PCL water vapour measurements in the dry lower stratosphere, where typical values for water vapour mixing ratio range from 1 to 10 ppmv, we require "weather balloons", also called radiosondes, to take in situ measurements of RH. The standard instrument for measuring water vapour in these sounding experiments is the Vaisala RS92 radiosonde. A standard RS92 measures temperature, pressure, and relative humidity as a function of altitude along its flight path.

Date	Weather	ALVICE Run	PCL Run (UTC)	RS92 (UTC)	CHF (UTC)
15/5/2012	Clear	Trailer Arrives	02:15 - 05:58	—	—
16/5/2012	—	Setup	—	—	—
17/5/2012	—	Setup	—	—	—
18/5/2012	—	Setup	—	—	—
19/5/2012	—	Testing	—	—	—
20/5/2012	—	Testing	—	—	—
21/5/2012	Cloudy	—	—	—	—
22/5/2012	Cloudy	—	—	—	—
23/5/2012	Low Cloud	6 hours 48min	02:12 - 08:30	04:18 and 06:34	—
24/5/2012	Clear	6 hours 24 min	02:29 - 08:58	03:39	07:01
25/5/2012	Clear	4hours 30min	02:38 - 07:07	03:57	—
26/5/2012	Partly cloudy	—	02:03 - 05:22	03:48	—
27/5/2012	Rain	—	—	—	—
28/5/2012	Low Clouds	2 hours	02:19 - 06:58	03:30	—
29/5/2012	High Clouds	4 hours 13 min	03:45 - 06:00	03:39	—
30/5/2012	Low Clouds	3 hours	02:23 - 05:21	—	—
31/5/2012	Clear	2 hours 24 mins	File Corrupted	07:48	04:44
1/6/2012	Rain	—	—	—	—
2/6/2012	Rain	—	—	—	—
3/6/2012	Rain	—	—	—	—
4/6/2012	Clear	5 hours 18 min	02:20 - 08:28	03:22 and 05:39	—
5/6/2012	Rain	—	—	—	—
6/6/2012	Clear	4 hours	02:41 - 06:56	03:10 and 05:28	—
7/6/2012	High Clouds	—	03:05 - 05:30	03:43	—
8/6/2012	Clear	6 hours 10 min	04:42 - 09:00	03:53	06:50
9/6/2012	Rain	—	—	—	—
10/6/2012	High Clouds	7 hours	03:00 - 08:49	04:02	—
11/6/2012	—	Packing	—	—	—
12/6/2012	—	Packing	—	—	—

Table 4.1: PCL-ALVICE field campaign log.

Most RS92 measure RH using a carbon hygristor composed of a small plastic strip with two metallic edges and a hygroscopic coating. As the RH changes, the thin coating expands and contracts, altering the electrical resistance across the elements [66]. The electrical current measured across the hygristor strip is then linearly proportional to the number of water molecules in the local environment and with the assumption of a saturation vapour pressure model can be converted to a value for relative humidity.

There are five issues relevant to the determination of the PCL calibration constant. I mention these issues not to disparage the validity of the measurements made by the Vaisala RS92 but simply as systematic uncertainties to be considered.

1. The primary purpose of the standard RS92 is to measure meteorological parameters in the lower troposphere. The instrument is not designed for high accuracy measurements of RH in the lower stratosphere. The calibration and validation of radiosondes for this purpose is an area of current active research. The most recent and notable examples of this kind of radiosonde calibration work was done by the World Meteorological Organization Intercomparison of High Quality Radiosonde Systems campaign in Vacoas, Mauritius (2005) and Yangjiang, China (2011) [41], [40].
2. At low values of RH (less than ~10% depending on the particular model version of RS92) the current response curve across the hygristor can become non-linear and the calculated RH calibration can be affected. Vaisala corrects for this error during the instrument calibration but we should keep in mind that the measurements of RH below ~ 10% are corrected [9]. Based on private communications with other RS92 users it is also inadvisable to trust the Vaisala correction below RH of 2%.
3. Cold temperatures induce a time lag in the hygristor measurements which effect the reliability of the RH measurement. Additionally, temperature differentials across the structure of the RS92 and between the RS92 and its environment can skew the RH value [14]. It is generally held that radiosonde measurements of RH obtained when the tem-

perature is less than -30 °C are not reliable and as such will not be used in this calibration experiment.

4. The RS92 measures RH with respect to the saturation vapour pressure over water. The SVP model used to calibrate the RH sensor is Wexler1976 [35]. The Wexler1976 model [70] is based on the saturation vapour pressure over ice.
5. An RS92 measures a current across a hygristor strip which is then converted into an estimation of RH by way of an assumed saturation vapour pressure model. The choice of model for saturation vapour pressure can have a profound impact on our calibration experiment for the following reasons:
 - (a) None of the major expressions have been compared to the recent measurements by Marti and Mauersberger (1993) [32];
 - (b) In most cases the models are extrapolated down to temperatures important in the stratosphere [38];
 - (c) Most models do not account for mixed-phase vapour pressures or metastable forms of ice [13];

The next section will include a discussion of saturation vapour pressure models.

4.5 Saturation Vapour Pressure Models

4.5.1 Uncertainties

Murphy and Koop (MK) [38] compared several prominent SVP models and measurements over a temperature range of interest for atmospheric work. MK compared experimental measurements of SVP taken over the last century and presented them in figure 4.1 with respect to the model envelope as calculated from the Clausius-Clapeyron equation (1.17). Added to their figure is a red line which is the average of the coldest temperatures retrieved from the nightly

radiosondes during this campaign. Figure 4.1 shows that the majority of the lab measurements for the SVP over ice fall outside the bounds of the Clausius-Clapeyron equation at temperatures which are common in the upper troposphere. It is therefore probable that the RS92 has an experimental dry bias [17].

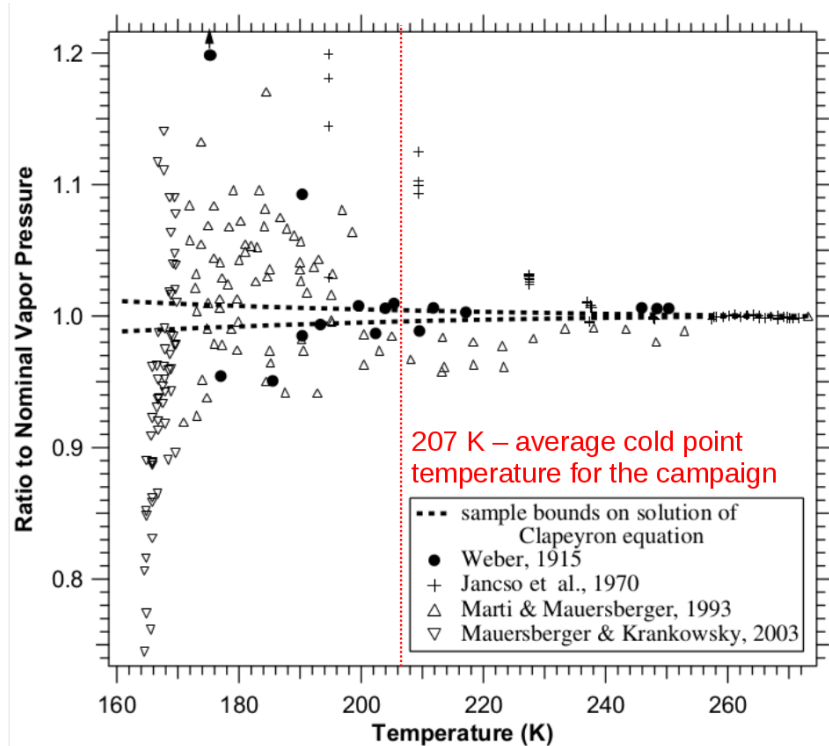


Figure 4.1: Experimental data measuring SVP over ice. Text in red indicates the average cold point temperature for the PCL calibration campaign. Taken and modified from Murphy and Koop 2005 [38]

Holger Vömel [64] made a similar comparison using the models of SVP over ice as seen in figure 4.2. Vömel chose to use the Goff-Gratch equation as a baseline model for comparing SVP ice models and his analysis in figure 4.2 shows that there can be significant differences in the models at temperatures colder than 200 K. Additionally, there is a positive ~ 2 percent deviation in the SVP at cold temperatures in the Hyland-Wexler 1983 model [65]. The Hyland-Wexler 1983 model is virtually identical to the Wexler1976 model (upon which it is based) used by Vaisala [65], [40]. Since equation (1.10) shows that an overestimation of the saturation vapour pressure would lead to a lower value of RH, it is therefore probable that the RS92 has a

dry bias which is the result of the choice in calibration model [38].

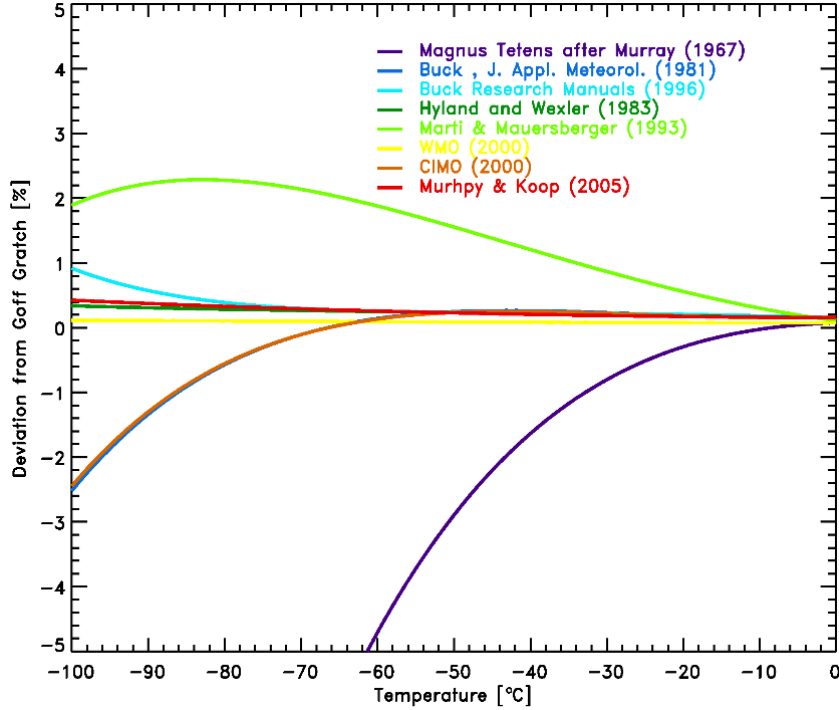


Figure 4.2: Model outputs measuring SVP over ice with respect to the Goff-Gratch equation. Taken and modified from Holger Vömel [64]

4.5.2 Saturation Vapour Pressure over Water and Ice

Figure 4.3 illustrates the magnitude of the variation between the SVP over water and ice based on simplified versions of the saturation vapour pressure equation (1.20). As the temperature drops below 273.16 K the water in the air does not immediately freeze but can remain in a supercooled liquid. If the air is free from nucleation surfaces, water can remain a liquid state down to temperatures of 230 K. This liquid water problem is a common phenomenon in clouds [47]. Having liquid water persist at altitudes where the temperature is colder than 273 K means that it may not be correct to assume a SVP model which depends on only ice surfaces.

Following the example of Murphy and Koop 2005 [38] a set of SVP models which are commonly referenced in the literature were compared over a range of temperatures common to the upper troposphere and lower stratosphere. Figure 4.4 shows the model outputs between

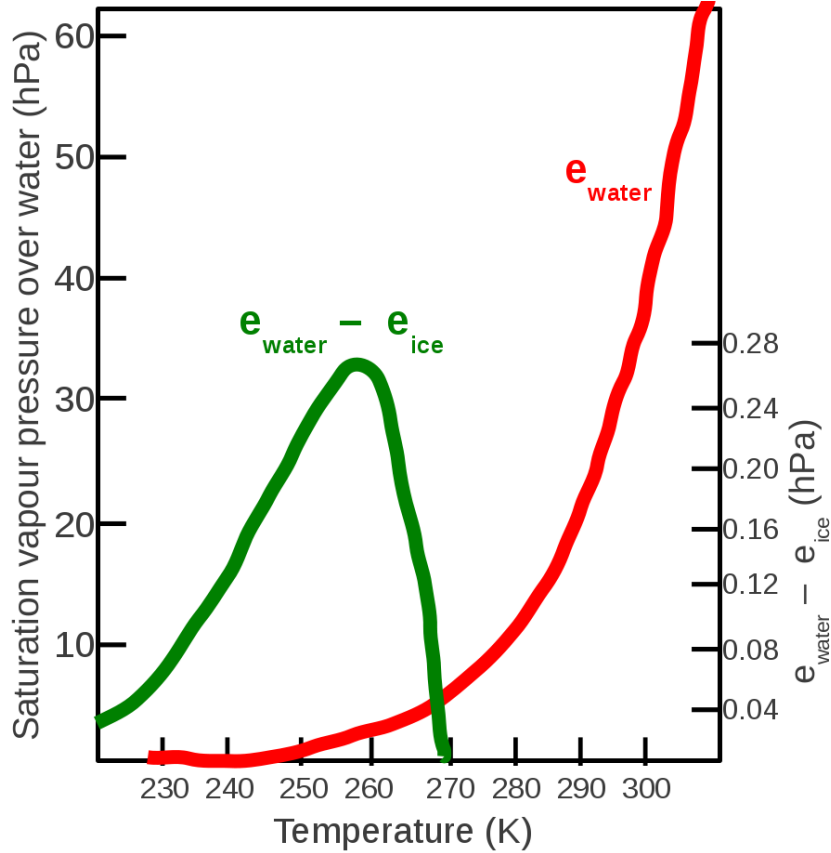


Figure 4.3: Variations in SVP with temperature over water (red) and between water and ice (green). Adapted from [68]

14 and 20 km for Goff-Gratch 1946 [16], Wexler 1976 [70], Goff 1957 [38], Hyland-Wexler 1983 [65], Buck 1981 [11], Sonntag 1994 [64], Magnus Tetens equation [39], Bolton 1980 [6], Murphy-Koop 2005 [38], Wagner-Pruß 2002 [67], and Tsonis 2002 [58]. As can be seen there is a factor of ~ 2 difference between the Murphy-Koop and Tsonis models. If the partial pressure of water at 14 km is nominally 5 hPa [44] then it can make a large difference to the absolute humidity, r , from equation (1.10), if the SVP is 2 hPa or 3 hPa.

Much of the variation between the SVP models comes from how water is incorporated (or not) in the initial assumptions. Figure 4.5 shows the a SVP model; over water divided by its counterpart over ice for the cases where a particular author developed both kinds of model. Wexler 1976 is the reference model as it depends purely on ice so its ratio is always one. As can be seen, especially at temperatures warmer than 273 K and colder than 230 K, it is important to

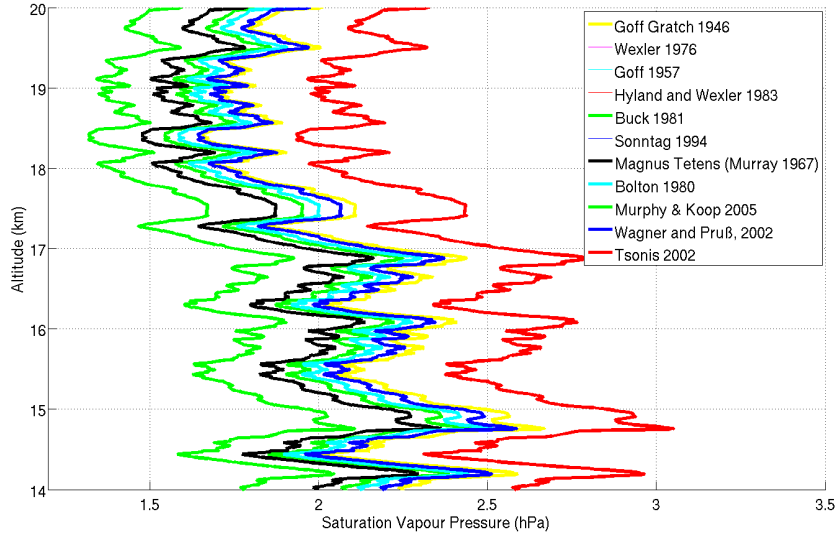


Figure 4.4: Variation between SVP models between 14 and 20 km for radiosonde data taken May 24 at 3:39 UTC. There is a factor of approximately two between calculations of the SVP according to the Tsonis and Murphy-Koop models.

choose a model which correctly incorporates liquid water. Since the Vaisala RS92 is factory-

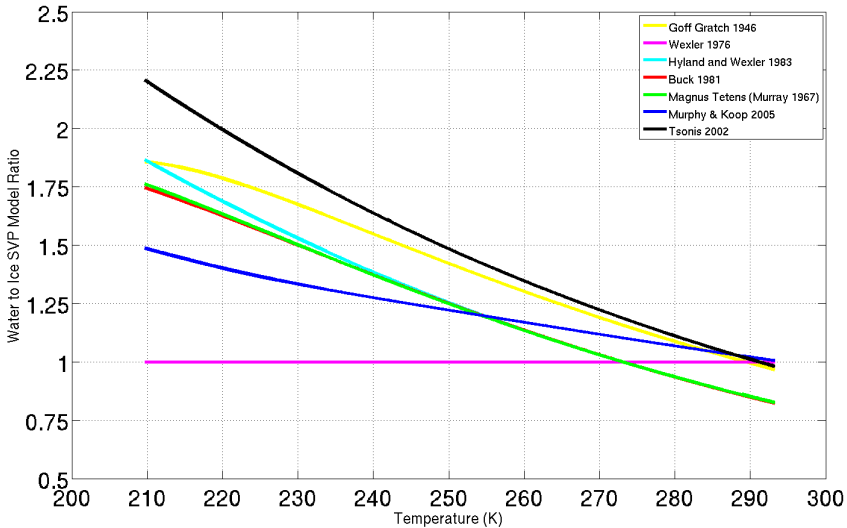


Figure 4.5: Ratios of SVP models for water and ice as a function of temperature.

calibrated to the Wexler 1976 model it is important to include a plot which shows how some of the other models compare to Wexler over a range of temperatures. It can bee seen in figure 4.6 that there are significant differences between the models. Of particular interest is how the Murphy-Koop (magenta) compares to Wexler (the unity line). The Murphy-Koop model is

the most aggressive in accounting for liquid water and also makes several corrections for the differences in saturation vapour pressure over several kinds of ice. To show the difference that model choice makes on real data, the radiosonde data for May 24 was converted into a mass mixing ratio profile using both the Murphy-Koop model and Wexler model. Then a percentile difference was calculated between the two profiles, shown in figure 4.7. From this plot it can be concluded that the in-factory calibration of the RS92 using the Wexler 1976 model discourages the use of alternate models as it can introduce large variations in data output. In order to apply an alternate SVP model to RS92 data, an RS92 would need to be reverse engineered in a lab setting to back out the Wexler derived system calibrations.

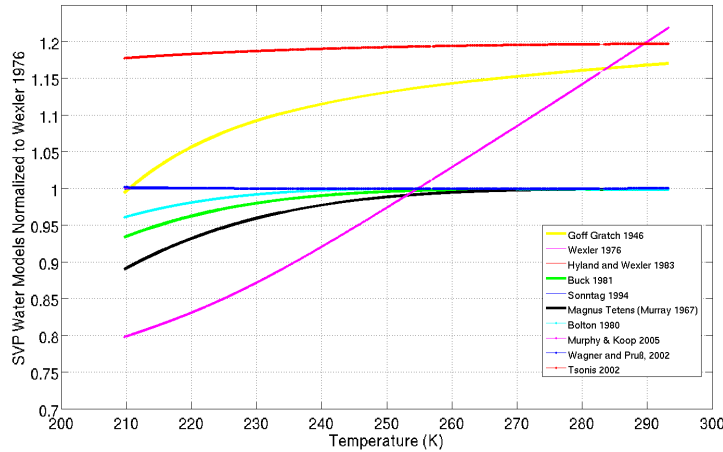


Figure 4.6: Ratios of SVP models to Wexler 1976.

4.5.3 Quantifying the RS92 Uncertainties

Given that there are both experimental and model uncertainties regarding RS92 measurements of water vapour at temperatures near those found in the upper troposphere, there needs to be an uncertainty envelope associated with the RH retrievals for the campaign's in situ measurements.

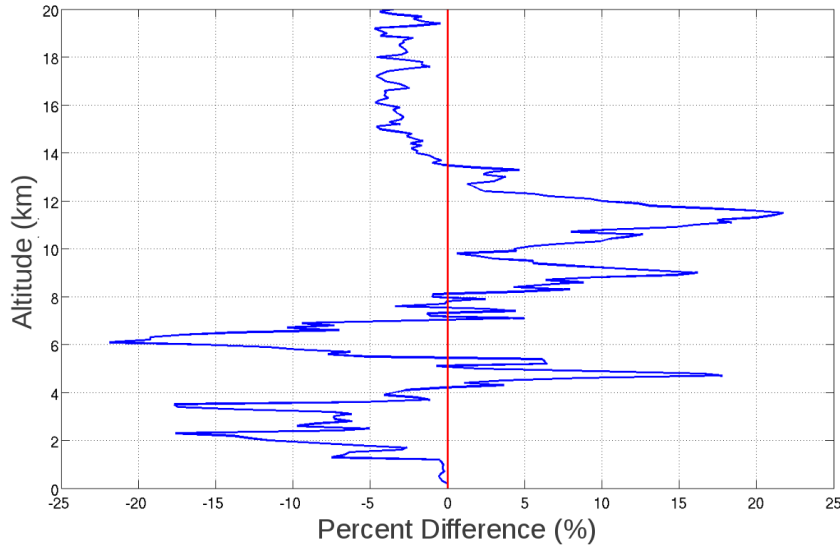


Figure 4.7: Percent difference of mass mixing ratios generated from Wexler minus Murphy-Koop model outputs from RS92 data taken during the PCL calibration campaign. The Wexler model has a wet bias with respect to the Murphy-Koop model between 8 km and 14 km.

Temperature Uncertainty

Recall that the general form of the saturation vapour pressure equation (1.20) depends only on pressure, temperature and enthalpy. Pressure can be related to temperature using the Barometric Equation (1.3) and improving on the lab measurements of enthalpy is beyond this project. That leaves the SVP uncertainty as a function of temperature only. A paper by Immel in 2010 [22] describes the uncertainty in RS92 temperature measurements, figure 4.8. Since the radiosondes for this campaign were launched after astronomical dusk we can assume that there is no contribution to the temperature uncertainty due to solar heating. Therefore, a constant standard uncertainty of 0.2 K was used for the error determination of the SVP models.

Relative Humidity Uncertainty

A comparison campaign between RS92s and Cryogenic Frost Point Hygrometers (to be discussed in the next section) done by Larry Miloshevich et al. in 2009 [35] attempted to address the RH biases in the RS92. The campaign established a percent difference profile with altitude, seen in figure 4.9, derived a set of polynomial fitting parameters which represent a correction

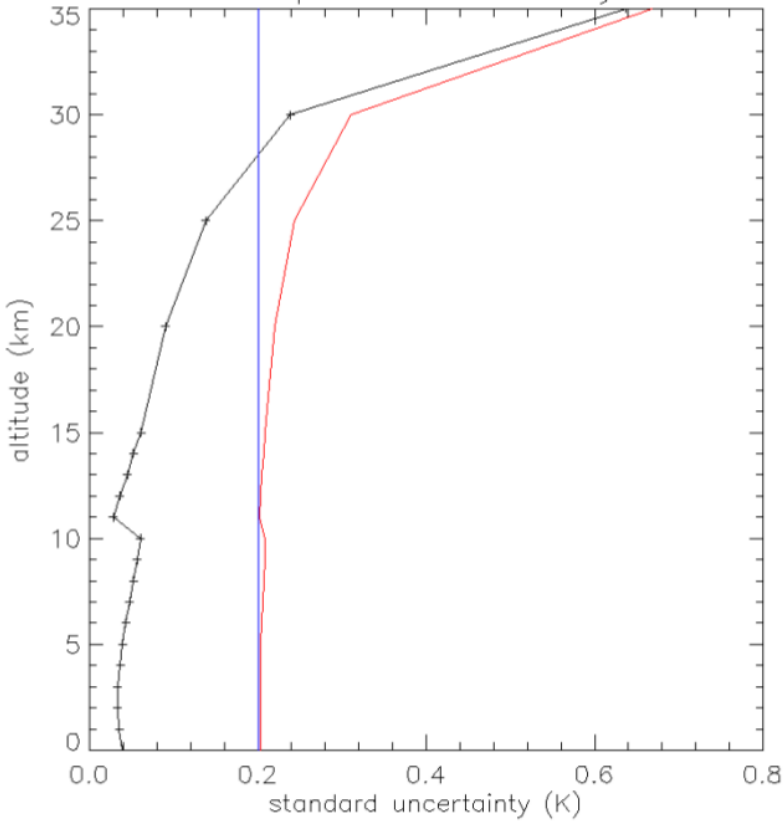


Figure 4.8: Uncertainty in RS92 temperature retrievals. Blue is measurement uncertainty, black is uncertainty due to solar heating, and red is total uncertainty. [22]

factor, and recommended a $\pm 5\%$ uncertainty for night time RS92 soundings [35].

The temperature and RH uncertainties from both of these papers were cited as best practice by the Global Climate Observing System (GCOS) Reference Upper Air Network (GRUAN) [40]. During this campaign the total errors on the RS92 water vapour mass mixing profiles were calculated by propagating these two uncertainties through the Wexler1976 model.

Creating an Uncertainty Envelope for the SVP Models

As was discussed in the subsection on saturation vapour pressure models, there is a great deal of variation between the various proposed models, recall figure 4.4. Determining which of these models is correct is beyond the scope of this thesis. However, it is possible to create an envelope between the two most extreme models: Murphy-Koop 2005 and Tsonis 2002. Figure 4.10 shows that the greatest spread between the two models is approximately 5.8% and occurs

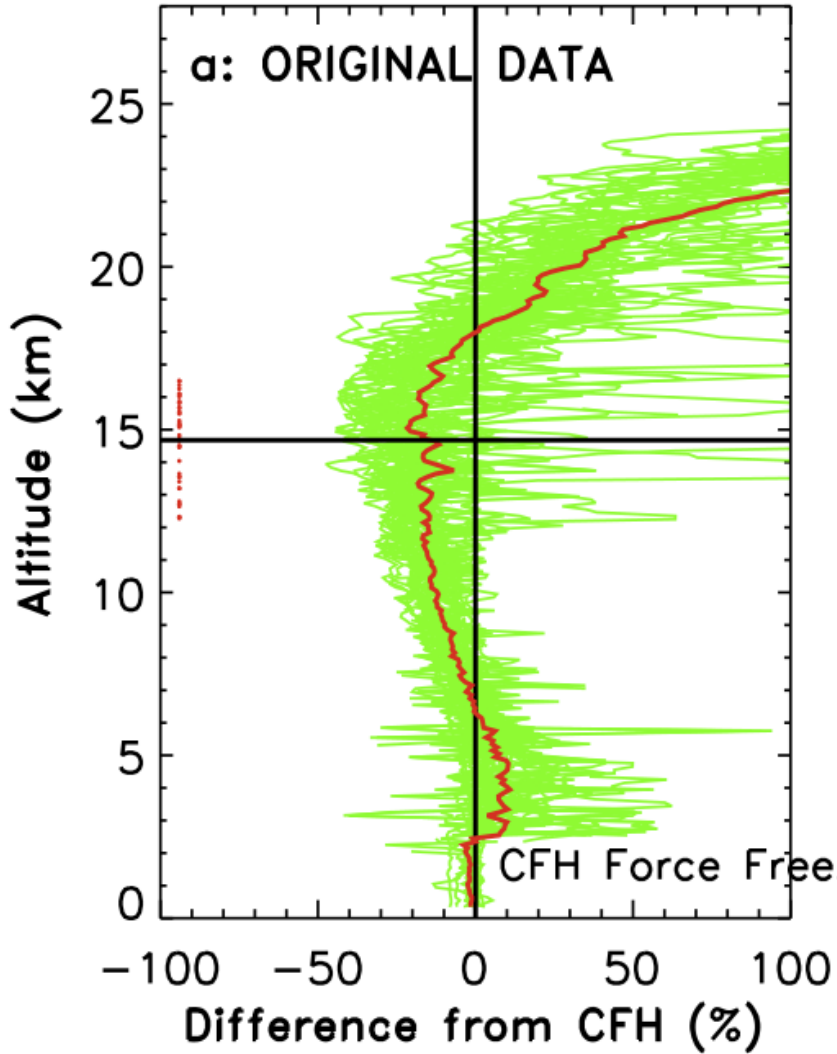


Figure 4.9: Percentile difference profile between RS92 RH profiles and CFH RH profiles. [35]

at the cold point of the atmosphere, near 12 km in the figure. The smallest spread between the models is near the surface at 3.9%.

4.6 Cryogenic Frost Point Hygrometers

Cryogenic Frost point Hygrometers (CFH) rely on a chilled mirror technique where a layer of dew or frost is allowed to form on a mirror. An optical system detects the condensation layer and engages a temperature feedback system which heats or cools the mirror to maintain a constant condensation layer thickness, see figure 4.11. The amount of water vapour in the at-

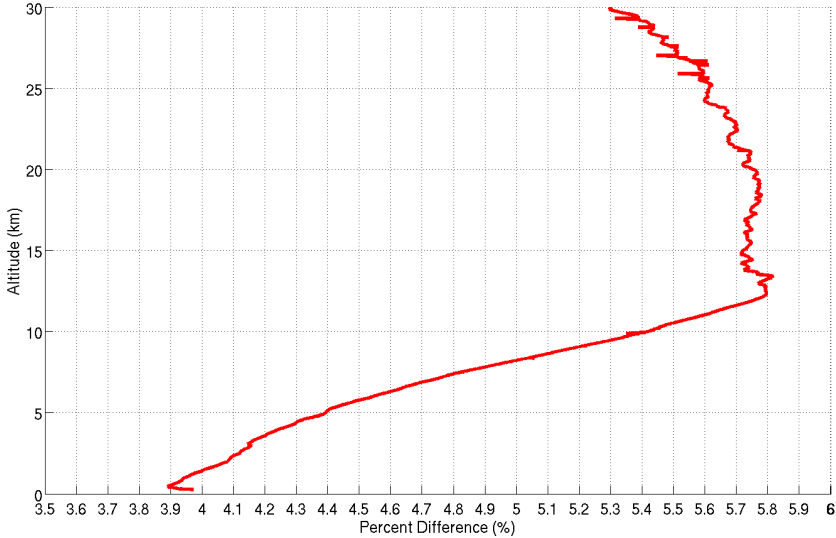


Figure 4.10: Percent difference between Murphy-Koop 2005 and Tsonis 2002 at altitudes from 275 m to 30 km.

mosphere can be determined from the temperature of the mirror. The water vapour mixing ratio can then be derived from the RH, temperature, and pressure of the air, by way of a saturation vapour pressure model [62].

In figure 4.11 the two dotted lines represent stainless steel tubes, approximately 3 cm in diameter, which act as air intake pipes. They are pushed into the CFH casing and held in place by an epoxy right before launch. The cryogen used during this campaign was tetrafluoromethane which was kept at 195 K by a dry ice bath. The CFH is designed specifically to measure water vapour in the upper troposphere and lower stratosphere. In contrast to the RS92, the CFH produces atmospheric measurements which agree with the SVP experiments of Marti and Mauersberger 1993 [32], with differences of less than 2.3% at 200 K. The CFH is calibrated using the Goff Gratch equation for saturation vapour pressure [63]. One limitation of the CFH technique is that it can only be used in clear skies. If a frost point sonde passes through a cloud, then the ice particles and water droplets in the cloud can enter the inlet tube and accumulate on the internal optics, which causes the mirror heater to engage and over compensate [50], [62]. When this happens the absolute calibration of the sonde can be lost.

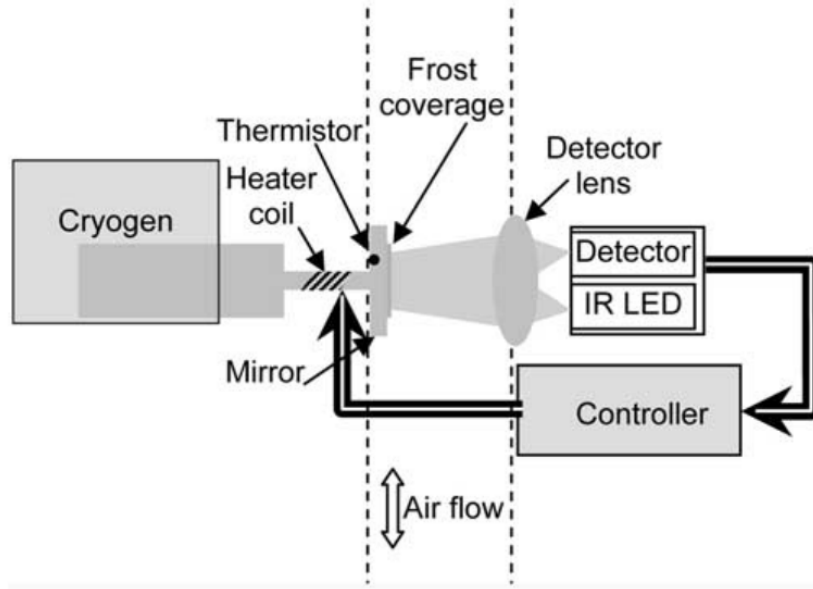


Figure 4.11: Schematic of the cryogenic frost point hygrometer (CFH). Shown is the cryogen tank which holds the carbon tetrafluoride, the heater coil, the mirror, and the optical frost layer detection system Taken from [62]

4.6.1 Past Lidar-CFH Comparisons

Three NASA Raman lidars, the JPL-TMF water vapour Raman lidar, GSFC Aerosol and Temperature lidar, and the GSFC Scanning Raman Lidar [72], were compared directly to CFH measurements during the first MOHAVE campaign. The initial comparison plot can be seen in figure 4.12 and shows lidar measurements which are contaminated at high altitude by fluorescence from the instrument optics. This fluorescence contamination affected all three systems above ~ 10 km as the lidars operate at the limit of their detection range above this region [28].

The fluorescence contamination was addressed for the second MOHAVE campaign and the Raman lidars were shown to give good agreement with the CFH up to 16 km, as seen in Figure 4.13. Fluorescence is not a concern in the PCL for the following reasons:

1. Unlike in ALVICE, the optical path of the transmitted and received light is separated in the PCL system. When the transmitter and receiver use the same optics there is the possibility for the fluorescence lifetime to overlap with the start of data collection. The result is 'ringing' in the receiver.

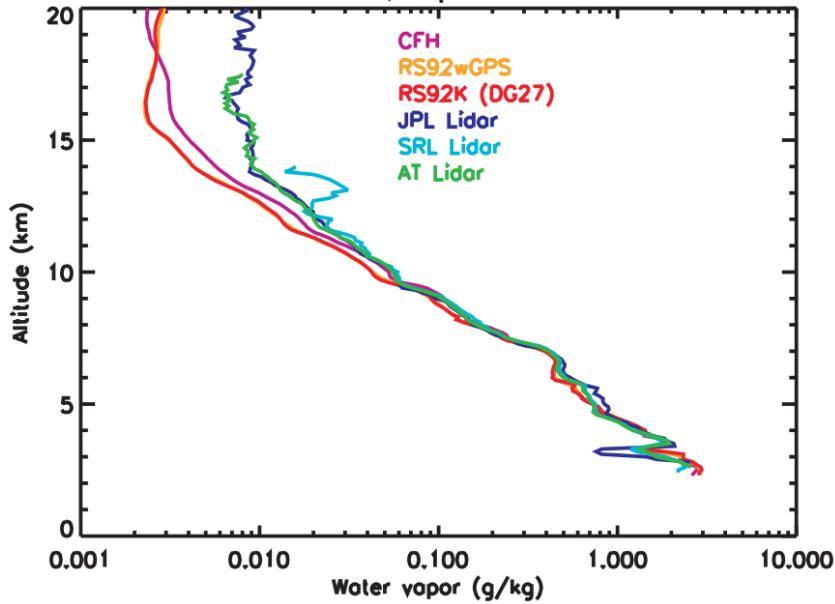


Figure 4.12: Initial CFH-lidar comparison contaminated by fluorescence. Taken from [28]

2. UV lidars are much more likely to have problems with fluorescence than lidars like PCL which operate in the visible.
3. PCL does not have a window on the top of the building through which the transmitted light and returned signal passes through. There is a hatch of the roof of the PCL Observatory which opens and exposes the system directly to the sky. Windows can also act as a fluorescence source.

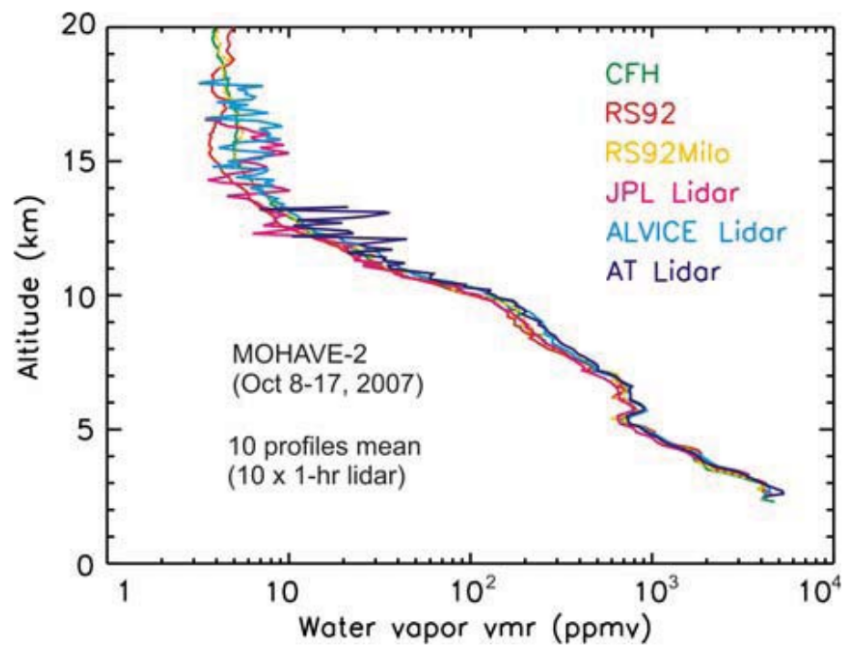


Figure 4.13: CFH-lidar comparison up to 18 km . Taken from [33]

Chapter 5

Results and Discussion

5.1 Summary

The analysis of the PCL-radiosonde campaign data has allowed for the derivation of a PCL system factor, ξ_{sys} . Additionally, comparisons of PCL-ALVICE below 8 km have validated PCL profiles of water vapour mixing ratio in the troposphere. PCL measurements of stratospheric water vapour have also been compared with CFH and ALVICE measurements but have yet to be validated pending further discussion on Raman lidar system corrections above 8 km. Finally, an interesting case study involving PCL stratospheric water vapour measurements, a CFH flight, and the effects of a cirrus cloud will be presented.

5.2 The Calibration Fitting Factor Results

A simple least squares method (5.1),

$$distance = \sum_{i=1}^n (Radiosonde_i - Lidar_i)^2 \quad (5.1)$$

where $Radiosonde_i$ is the water vapour mass mixing ratio at height i , calculated from the radiosonde data, $Lidar_i$ is the corresponding water vapour mass mixing ratio at the same height,

Date	Fitting Factor	Reduced Chi-squared	Good Fit?
May 24	0.812	1.98	marginal
May 24	0.688	2.04	marginal
May 25	0.813	1.48	good
May 26	0.781	2.51	marginal
May 28	0.782	1.74	marginal
May 29	0.938	1.41	good
June 4	0.609	1.74	marginal
June 4	0.656	1.45	good
June 6	0.578	1.65	good
June 6	0.656	1.84	marginal
June 7	0.812	1.47	good
June 8	0.750	1.41	good
June 8	0.906	1.48	good
June 10	0.781	1.73	marginal

Table 5.1: Table of derived lidar fitting factors and reduced chi-squared values for each night of good data during the campaign.

from the lidar, and n is the number of coincident data points, was used to minimize the distance between the hourly PCL profiles and the nightly radiosonde. Each profile was iterated, using the method found in Numerical Recipes [45], until a scalar fitting factor, ξ_{sys} , was determined for each clear sky night. The results of this series of calculations appears in Table 5.2 and the code used to generate the values can be found in Appendix B.

A reduced chi-squared value is also determined as an indication of goodness of fit. Equation (5.2), where σ^2 is an estimation of the total variance, and k is the number of degrees of freedom, shows a reduced chi-square equation used to generate the values in table 5.2.

$$\chi^2_{reduced} = \Sigma \left(\frac{(Sonde_i - Lidar_i)^2}{\sigma^2} \right) \left(\frac{1}{k-1} \right) \quad (5.2)$$

The average scale factor generated from the PCL-ALVICE calibration campaign is 0.754 with a chi-squared value of 1.71. The relatively large average value of the reduced chi-squared is not unexpected. Recall that a lidar is a ground based, zenith pointing measurement and the radiosonde is an in situ measurement which travels with the mean wind. In effect we are seeing the differences between the Lagrangian and Eulerian measurement frames. It is possible to

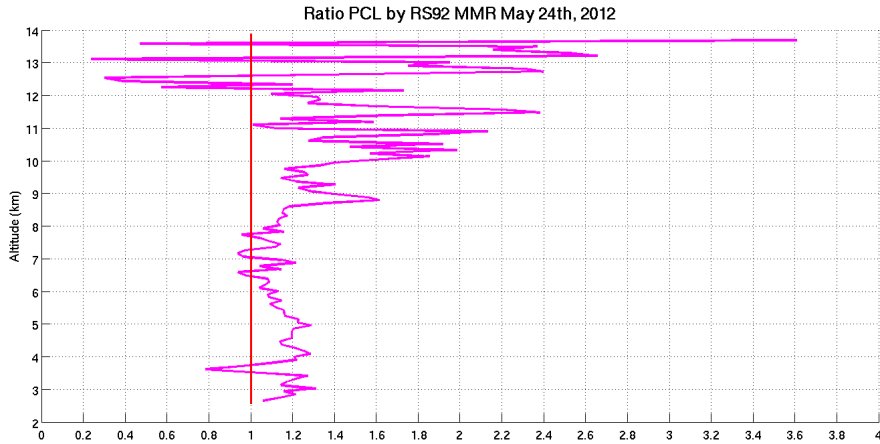


Figure 5.1: The scale factor is only generated from measurements between 3 and 8 km.

calculate radiosonde back-trajectories in an effort to more closely match the air sampled by the sonde and that measured by the lidar; however, time constraints precluded that analysis in this work.

The altitude limits for the fit were determined from the best practice recommendations that came out of the MOHAVE campaigns: [29], [28], and [33].

1. Lidar overlap and non-linear optical effects are known to dominate the near-field returns below ~ 3 km. Inspection of the raw PCL lidar scans show that the overlap error is less than 5% at ~ 2.5 km. Below this point lidar profiles of water vapour mixing ratio have a pronounced dry bias that will need to be corrected in the future. The derivation of the PCL fitting factor allowed for a conservative lower altitude limit of 3 km to ensure that the calibration constant is not influenced by the near field errors. Figure 5.1 shows the characteristics of a percent difference plot between the RS92s and uncorrected PCL water vapour measurements. The feature at ~ 3.6 km represents a well known dry bias which occurs in RS92s as they cross the 273 K isotherm [14].
2. Systematic errors in RH retrieval from radiosondes, as were discussed in chapter 4, become problematic at temperatures below -30°C . For late spring 2012 in London ON this corresponds to an attitude of approximately 8 km. The corrections which can be applied

to RS92 RH profiles for colder temperatures [35], [41], [40] are not easily reproducible by the PCL. Since future RS92 data against which PCL can be compared will not be corrected, the calibration constant was derived with respect to standard RS92 data.

3. Recall that $\Xi_{sys}(z)$ is also a term which is applied to correct for high altitude differences between remote sensing and in situ techniques. There is disagreement in the literature on the best practice for correcting Raman lidar data, near the limits of its detection range, with radiosonde data which contains known biases. There are currently three main ideas for generating this correction:
 - (a) Determination of seasonal correction factors from an ensemble of radiosonde measurements, Moss (2012) [37]
 - (b) Determination of nightly correction factors from individual radiosonde flights, Whitteman (2006) [72]
 - (c) Hybrid radiosonde-lamp calibration which is used to actively correct lidar returns, Leblanc (2008) [27]

5.3 Testing the Calibration Fitting Factor

The percent difference between each pair of RS92 radiosonde and PCL mass mixing ratio (MMR) profiles (Figure 5.2) was calculated as well as the percent difference over the ensemble of measurements (Figure 5.3). As can be seen from figure 5.3 PCL measurements of water vapour MMR are now calibrated to better than $\pm 5\%$ against in situ measurements from 2 km to 9.5 km. Below 2 km altitude, PCL measurements are still dominated by problems associated with the differential overlap function and near field optical effects. In the future, Ξ_{sys} ($0.277 \text{ km} < z < 2 \text{ km}$) can be determined by generating a correction from the radiosonde measurements following the experimental method of Wandinger et al. (2002) [69]. As was discussed earlier in this chapter, the best method to account for the possibility of Ξ_{sys} ($z > 9.5 \text{ km}$)

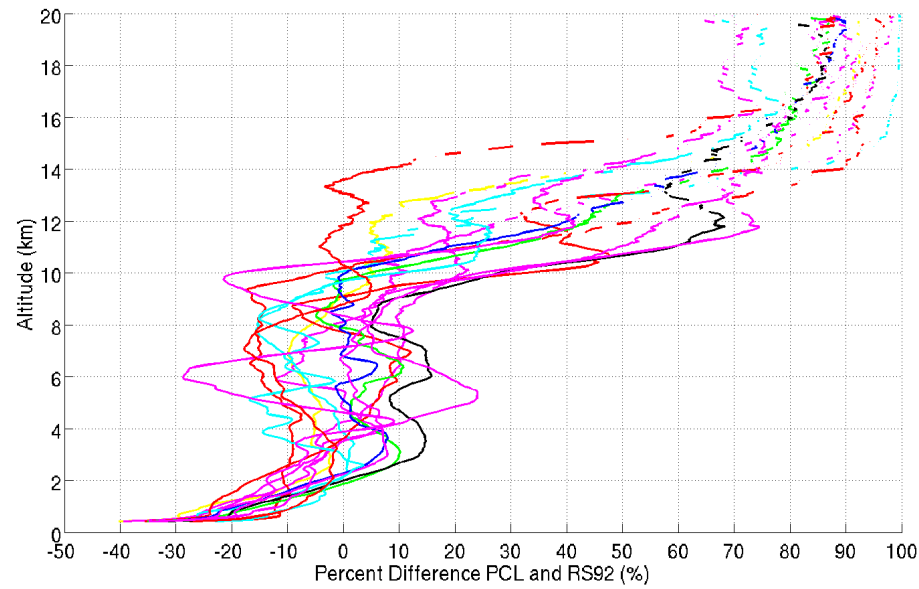


Figure 5.2: Percent difference between each RS92 MMR profile and the hourly profile from PCL.

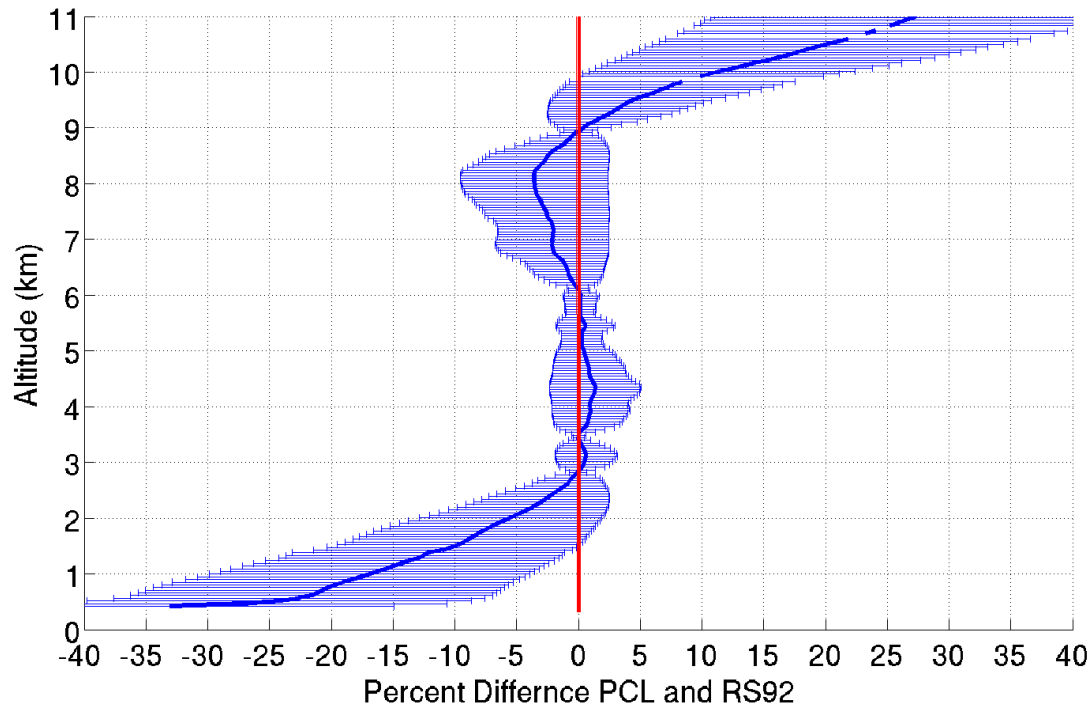


Figure 5.3: Percent difference between the ensemble of RS92 and PCL profiles of MMR with RMS errors.

is still subject to debate.

5.3.1 Difference Profiles

The comparison between the RH as measured by RS92s and CFHs was discussed in chapter 4 and presented in figure 4.9. The RS92 was shown to have a dry bias from the frost point, near 3 km, until approximately 6 km where it started to measure a wet bias with respect to the CFH. The large dry bias of the RS92 above 18 km is the result of RS92 measurements experiencing the difficulties which were summarized in chapter 4.4. Referring to Figure 5.4, the same pattern of biases can be seen between the RS92 and PCL. While not conclusive, this comparison may indicated that the deviations between RS92 and PCL measurements of MMR could be resolved by the application of RS92 corrections derived by Miloshevich et al. in 2009 [35]. Note, the altitude differences in the structures of both profiles can be accounted for by geography: Figure 4.9 by Miloshevich involves radiosondes which were launched in the tropics and Figure 5.3 of PCL campaign data were taken in the mid-latitudes. Tropopause height can range in height from ~9 km near the poles to greater than 17 km near the equator [68].

5.4 Applying the Calibration Fitting Factor

The average calibration fitting factor, $\xi_{sys} = 0.754$, has been integrated into the PCL water vapour processing code. The final step in the campaign data analysis is to validate PCL results against an NDACC reference instrument as described in Chapter 4.2. ALVICE is a mobile NDACC reference instrument for Raman lidars. The percent differnce between the ALVICE and PCL MMR profiles was calculated and can be seen in Figure 5.5 and an average percent difference for each night was recorded in Table 5.2. Figure 5.6 shows excellent agreement between ALVICE, PCL, RS92, and CFH from 2 km to 9 km. Small variations can be attributed to RS92 and CFH flight paths, which sample the atmosphere downwind of the lidars, and the averaging and co-add regimes employed by each lidar. Since this is a blind instrument

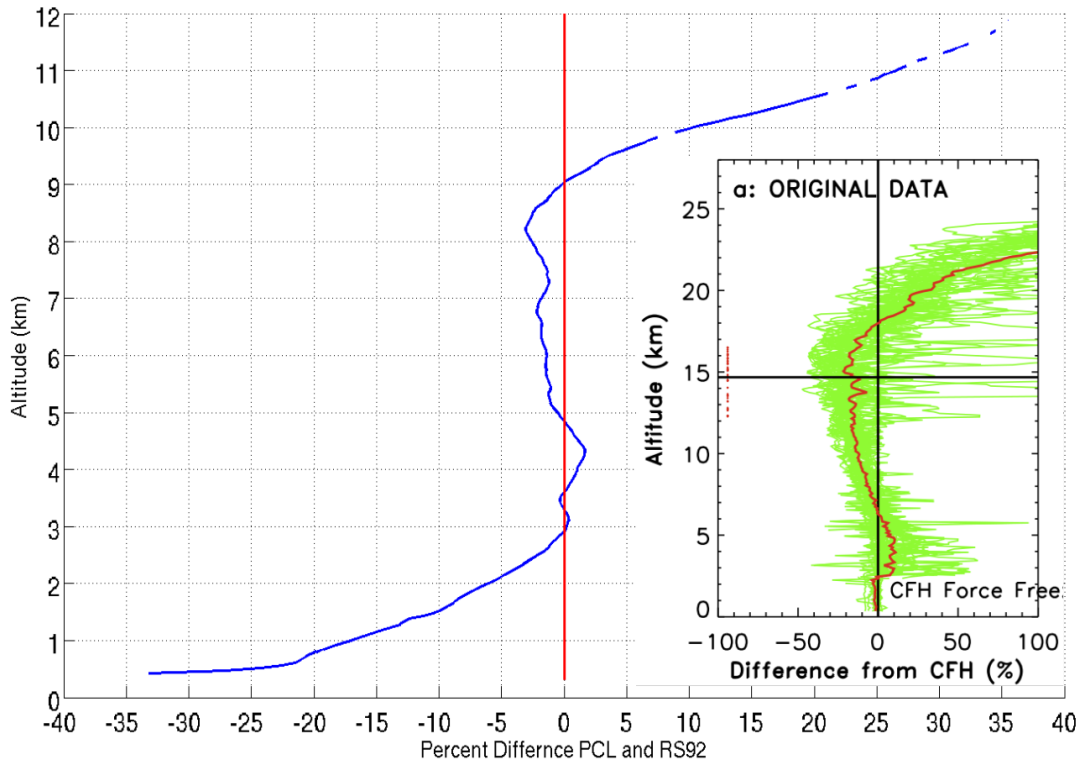


Figure 5.4: Comparison of the percent difference plots between RS92&PCL and RS92&CFH. [35]

Date	Average Percent Difference (%)	Good Fit?
May 24	-8.93	acceptable
May 24	1.07	excellent
May 25	-10.75	poor
May 26	-10.44	poor
May 28	-9.40	acceptable
May 29	-14.59	poor
June 4	-3.59	excellent
June 4	-2.62	excellent
June 6	1.98	excellent
June 6	-0.30	excellent
June 8	-11.49	poor
June 8	-7.29	acceptable
June 10	-8.93	acceptable

Table 5.2: Table of the average percent difference between MMR values measured by PCL and ALVICE lidars for each night of good data during the campaign. Poor fits have percent differences greater than 10%, acceptable fits have differences between 5% and 10%, and excellent fits have differences less than 5%.

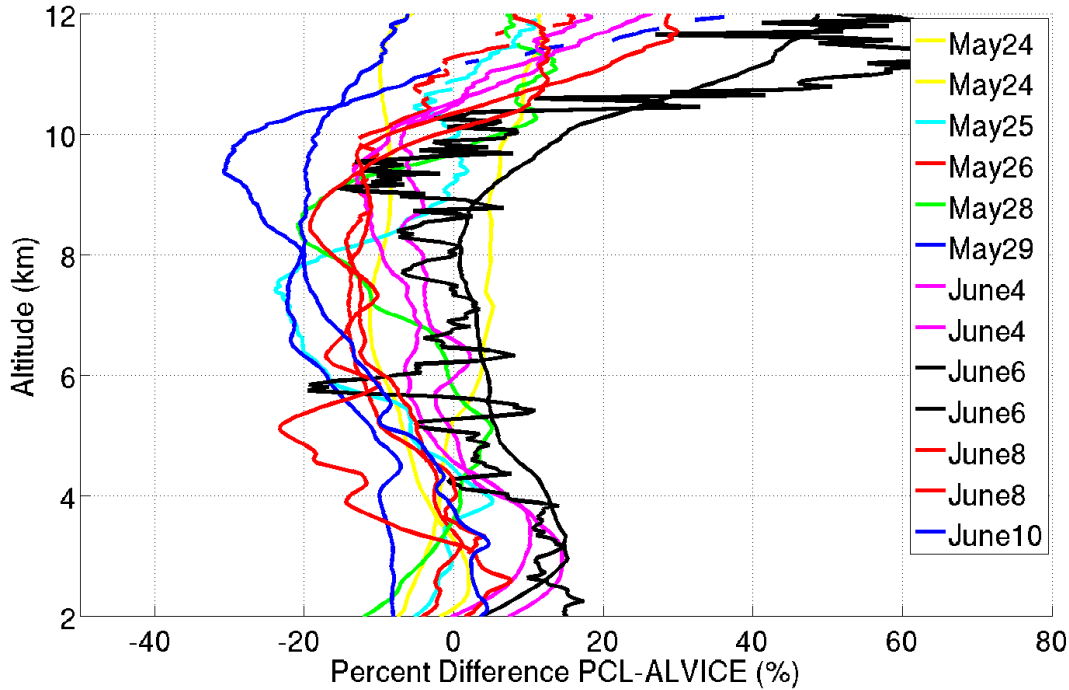


Figure 5.5: Percent difference with height for PCL and ALVICE MMR profiles.

comparison, the statistical criteria and data binning practices of PCL and ALVICE are sure to differ. Lower level profiles of MMR appear to be validated by comparison to ALVICE. Figure 5.8 shows that above 12 km PCL measures a moister atmosphere than ALVICE however, above 14 km the two are generally in agreement. Appendix A contains the plots from every night of the campaign. PCL and ALVICE profiles of MMR often lie within error bars and in many cases have excellent agreement when measuring fine scale variations in water vapour and layering.

Figure 5.7 is an ensemble of percent differences between PCL and ALVICE mass mixing ratio profiles. Ignoring comparisons below 2 km, which have not been corrected for overlap, it can be seen that PCL measures a moister atmosphere up to 4 km. Between 4 km and 10.5 km PCL measures a much drier atmosphere than ALVICE and above 11 km again measures more moisture than ALVICE. Given that PCL and ALVICE measured the same atmosphere at the same time, and that the lidar equation correctly describes the count profiles, then the systematic differences between PCL and ALVICE water vapour profiles must arise during data processing. NDACC should meet and agree on a standard water vapour processing algorithm.

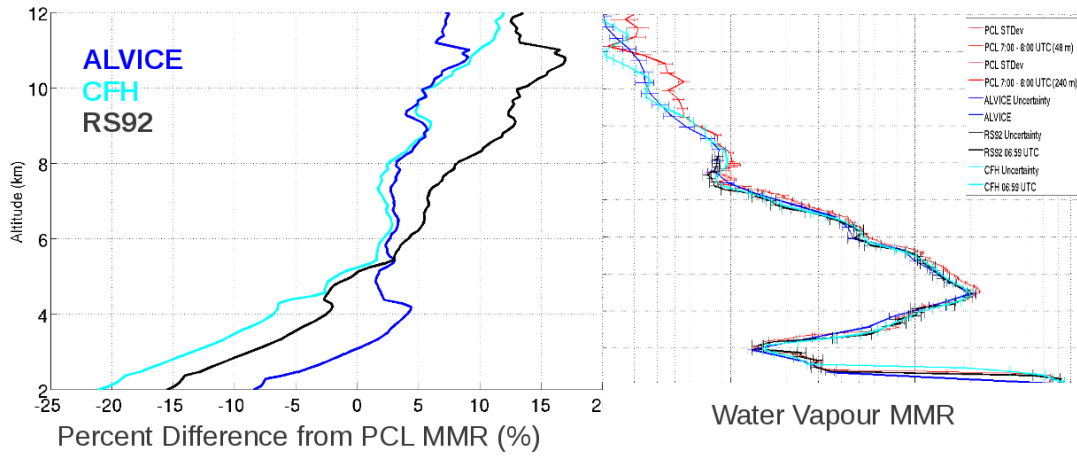


Figure 5.6: Example of a scaled tropospheric PCL lidar profile compared to an RS92 profile and an ALVICE profile accompanied by a percent difference plot between each of the CFH, RS92 and ALVICE with PCL.

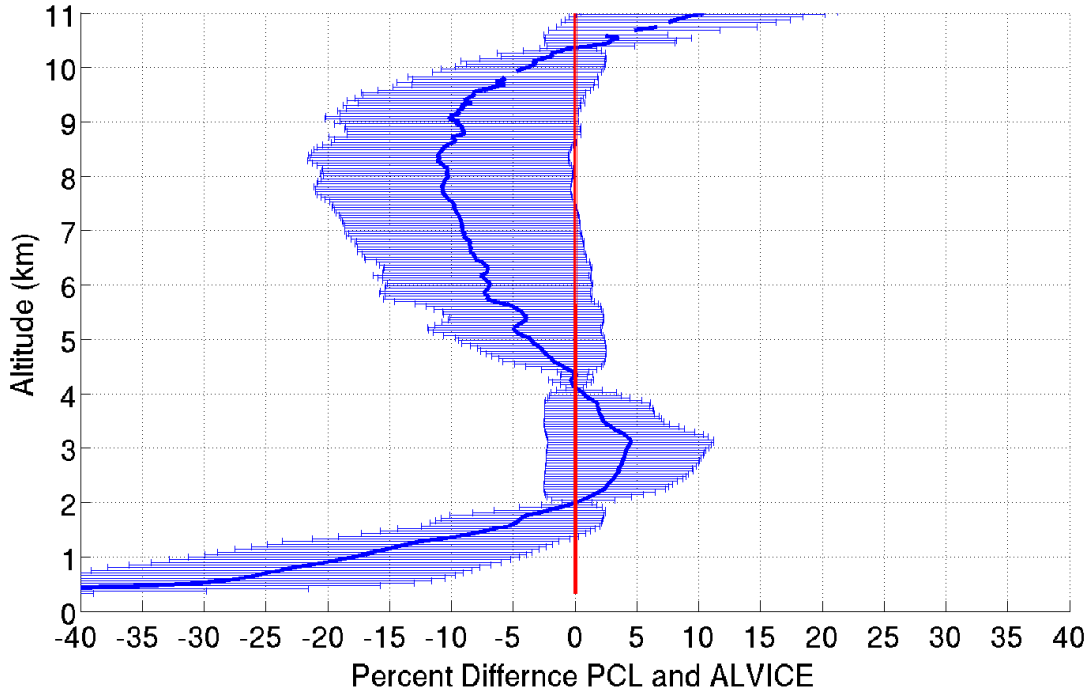


Figure 5.7: Percent difference between the ensemble of ALVICE and PCL profiles of MMR with RMS errors.

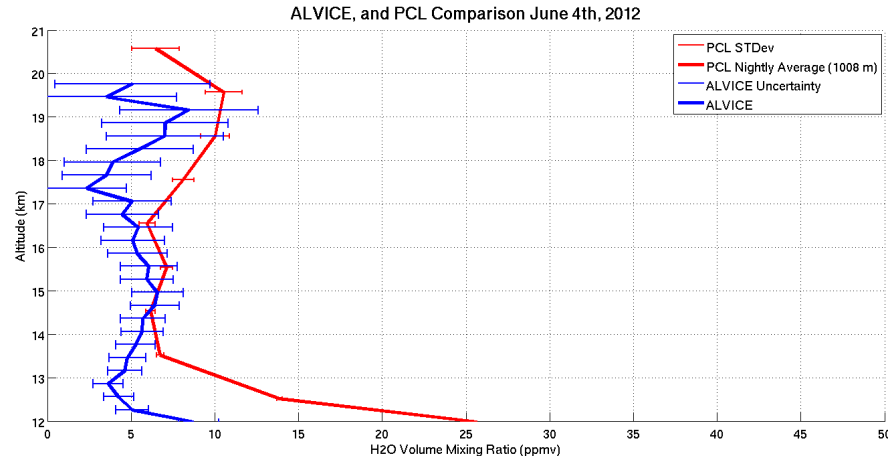


Figure 5.8: PCL and ALVICE stratospheric water vapour returns.

5.5 Case Study: June 8th Cirrus Cloud Event

June 8th was an interesting night for comparing the CFH to the two lidar systems. Figure 5.9 shows an unexpected drop in the water vapour volume mixing ratio (VMR) near 11.5 km as measured by the CFH. After this event the percent difference between the lidar measurements and the CFH spike, figure 5.10. Further investigation was clearly warranted. The flight path of the CFH was retrieved from the data file and the GPS position of the launch site (PCL Observatory) and touch down site (Lake Erie) are plotted in figure 5.11. The CFH encountered the moisture anomaly at an altitude of approximately 11.5 km. The average ascent rate of the sonde was approximately $4.8 \frac{\text{m}}{\text{s}}$ which means that the balloon would have been about 40 minutes south of the observatory, over St. Thomas.

Looking at the CFH standard data plots provided by the ALVICE group, Figure 5.12 it can be seen that the CFH and RS92 recorded 100% RH from ~ 9.5 km to just over 10 km. This is very strong evidence for a cirrus cloud.

Taking a closer look at the total back scatter plots for the night of June 8th it can be seen that there is indeed a cirrus cloud layer which begins to form over the observatory about an hour after the CFH launch. Figure 5.13 is an estimation of the flight time and altitude of the CFH. Notice that the balloon would appear to pass through the leading edge of the cloud layer

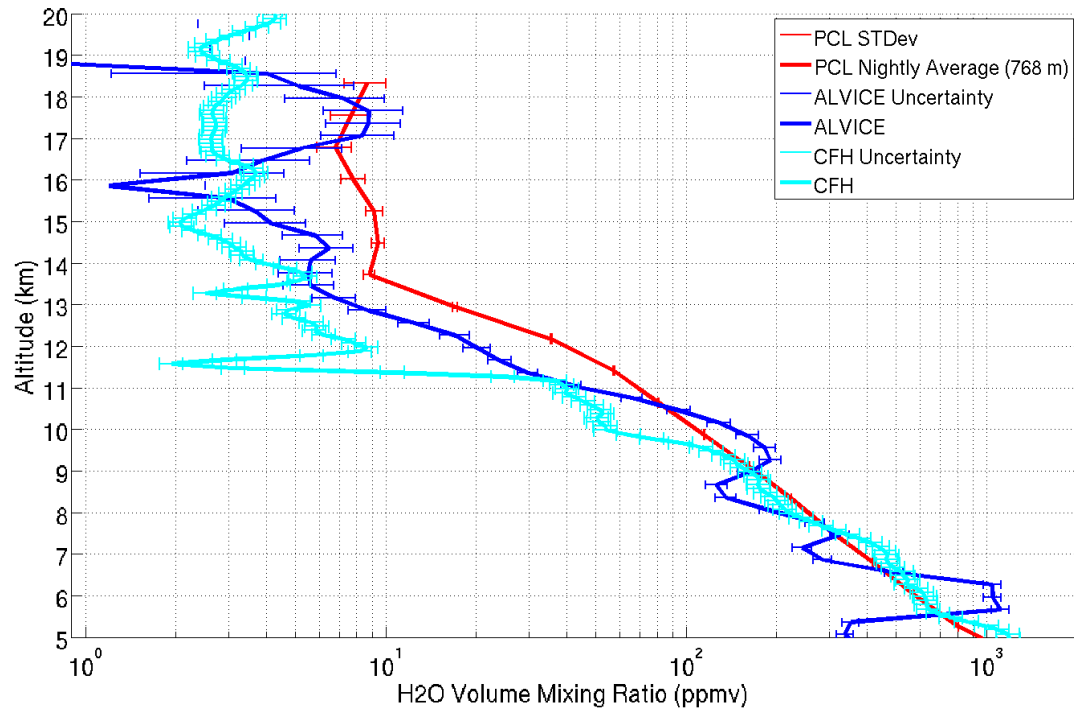


Figure 5.9: Unexpected drop in CFH VMR compared to both lidars.

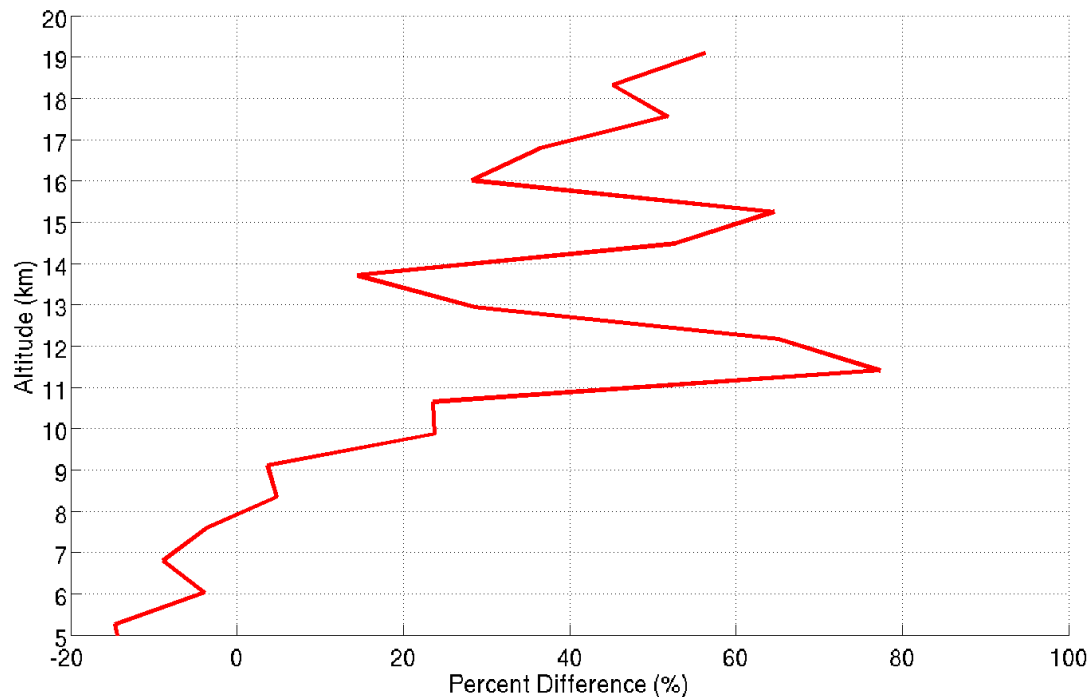


Figure 5.10: Unexplained deviations between the CFH and the lidars above 10.5 km.



Figure 5.11: Approximation for the flight path for the June 8th CFH.

at a time and altitude which corresponds with the moisture anomaly.

There are two possible explanations for how a cirrus cloud could contribute to the discrepancy between the CFH and lidar measurements above 10 km:

1. Recall that CFHs operate by drawing moisture laden air across a temperature controlled mirror and then using the resulting condensate to infer atmospheric water content. When a CFH passes through a cloud containing liquid water droplets or ice particles, the mirror can become coated with a layer of water, causing the heater to engage and warm the mirror. After evaporating the excess water from the mirror, the CFH may have difficulty reforming an appropriate frost layer on the mirror, producing a dry bias in subsequent measurements [50].
2. It is possible that there is a differential transmission correction that should be applied to light at 532 nm, 607 nm, and 660 nm when travelling through a cirrus cloud. If light at 607 nm is attenuated slightly more than light at 660 nm when passing through the cloud then the returned signal in the nitrogen channel would be deficient when compared to the water signal. This achromatic transmission would induce a wet bias in the PCL VMR profile.

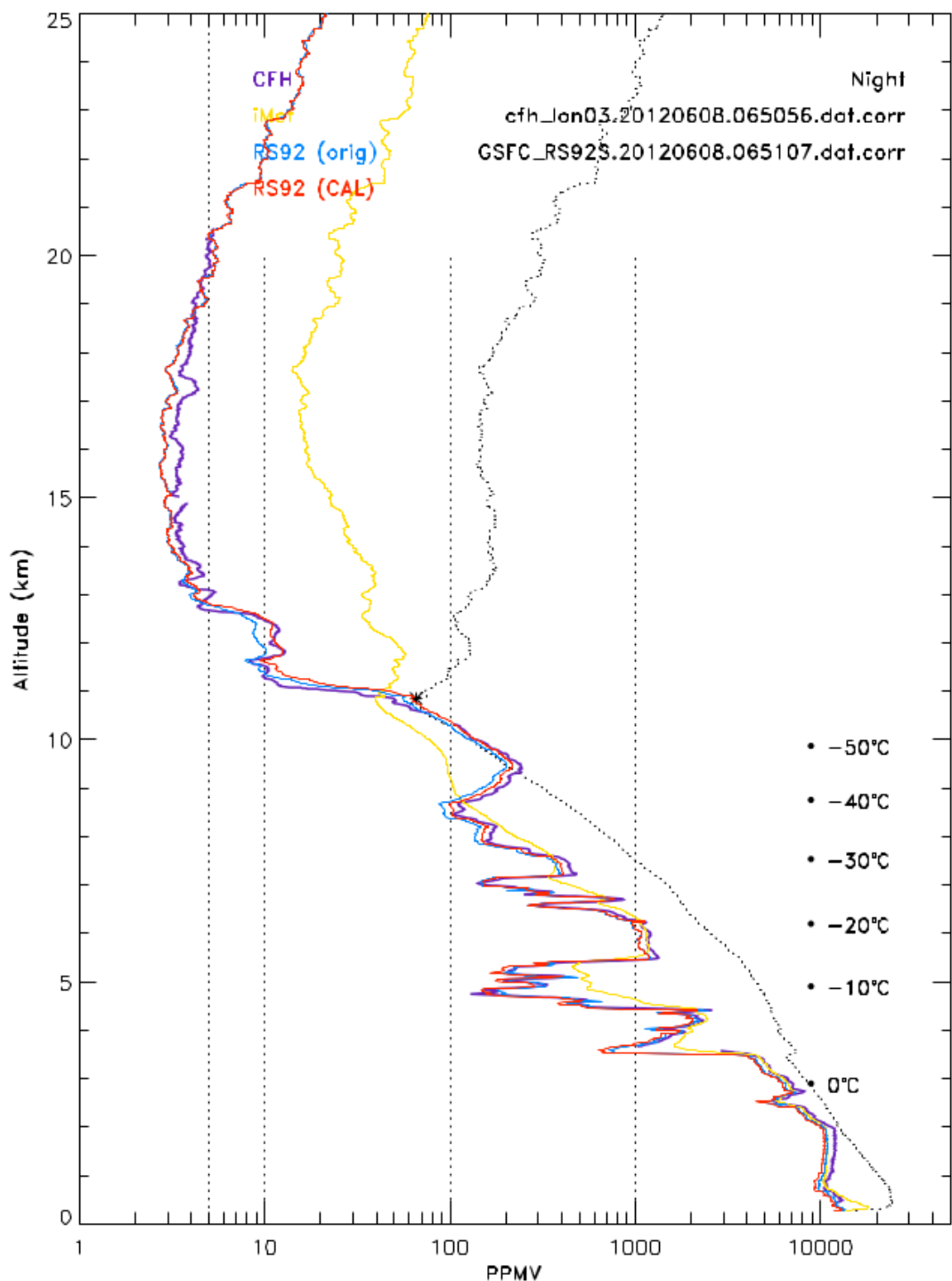


Figure 5.12: Standard CFH and iMet plot for June 8th. CFH (purple), RS92 radiosonde (red), iMet radiosonde (yellow), and SVP curve (black dots). 100% RH is occurring near 10 km.

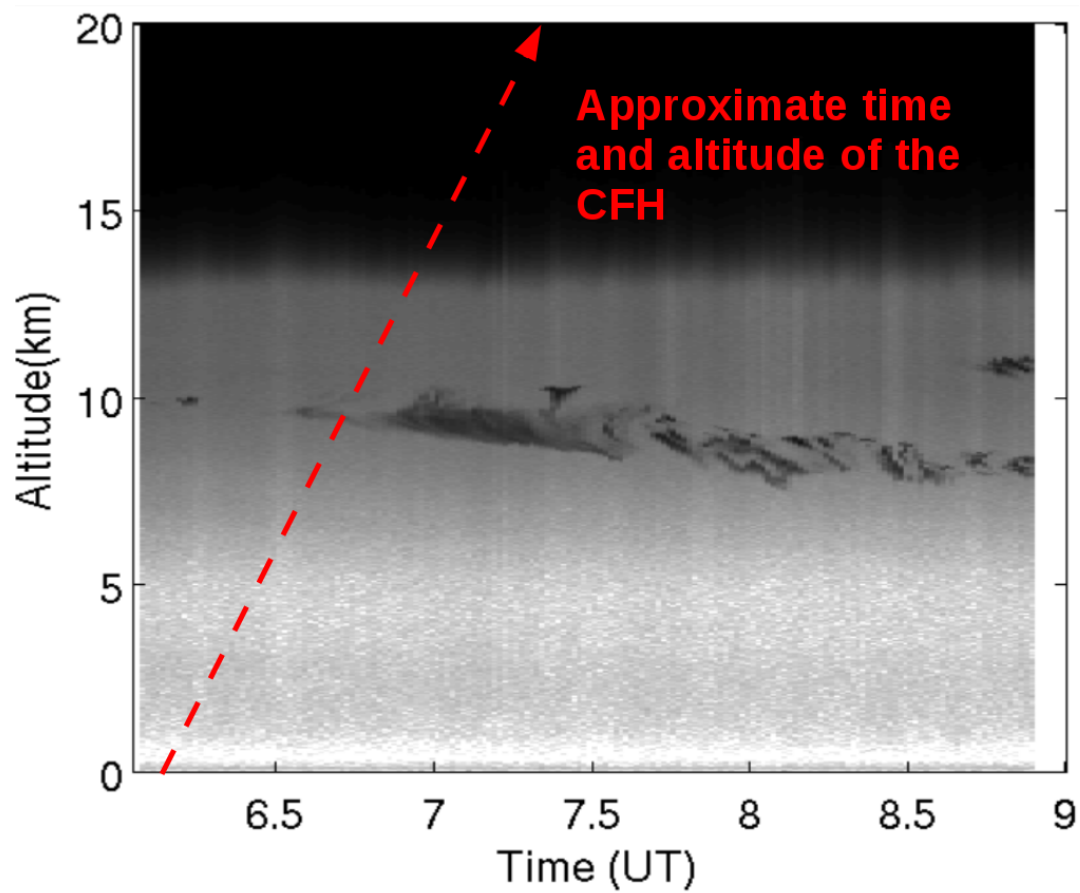


Figure 5.13: PCL and ALVICE stratospheric water vapour returns.

Chapter 6

Conclusions and Future Directions

6.1 Conclusion

The Purple Crow Lidar has been successfully moved from Delaware Radar Tracking Station to the UWO Environmental Science Western Field Station, received new optical components and faster counting electronics, and has participated in a calibration and validation campaign. The application of a system correction factor of $\xi_{sys} = 0.7545$ brings PCL water vapour profiles into agreement at $\pm 5\%$ with in situ measurements in the range from 2 km to 9 km with no systematic height corrections required from 2 km to at least 10 km. Further, comparisons between the lidar profiles of both PCL and ALVICE have validated PCL profiles of water vapour mass mixing ratio over the same range. The process of approving PCL water vapour measurements for submission to the NDACC can now proceed with confidence.

6.2 Future Work

6.2.1 Instrumentation

1. Analysis of PCL water vapour profiles indicates a likely ground loop in the system, figure 6.1. This ground loop produces signal with a period of slightly over 14 minutes

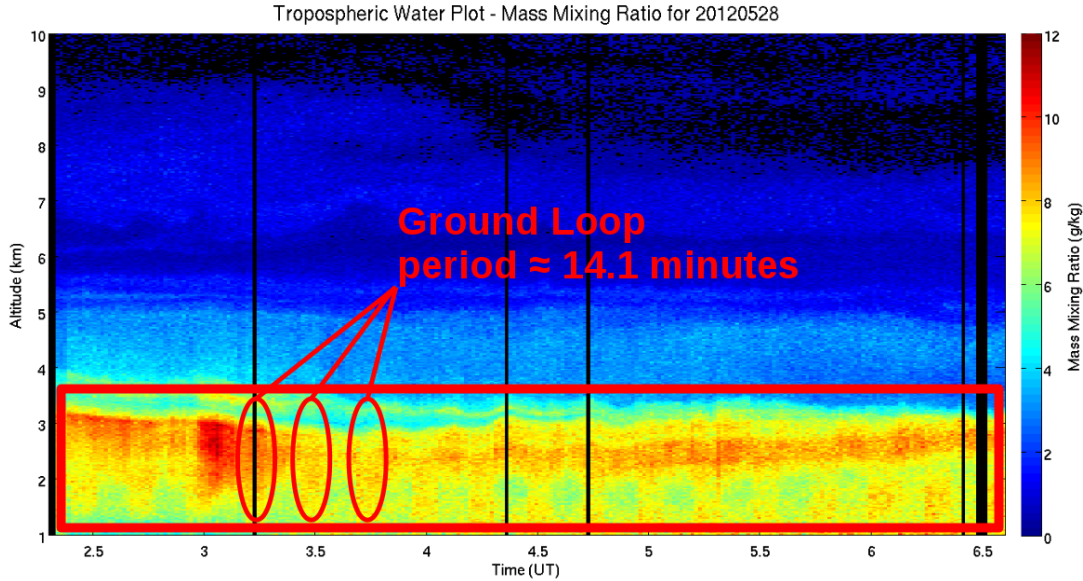


Figure 6.1: Ground loop contaminating PCL returns below ~ 3 km.

and prevents the derivation of a system correction, Ξ_{sys} ($0.277\text{km} < z < 2\text{km}$) which will allow PCL water vapour profiles to extend to the ground.

2. Automated computer control of the motorized mount of the final up mirror (Figure 2.8) would allow for faster and more accurate alignment of the laser beam in the sky. Reducing the required time for nightly system alignment and removing the potential for human-induced error would improve data quality and consistency.
3. Complete the installation of an overlap channel using a side mounted optical telescope as a secondary lidar receiver connected to the low level Rayleigh channel (see Figure 2.1). The new channel would allow measurement of the overlap function which would eliminate the need for model approximations. Having measurements of the overlap function will also allow for a better experimental correction for low level water vapour.
4. Wire the dew point monitor into the mercury telescope braking system. Eliminating the human in this process is a benefit for the mirror air bearing. Should the humidity of the air supplied to the bearing rise above a dew point of 240 K the monitor should trigger the secondary pressure regulator to cut flow to the mirror and trigger the breaks.

5. Complete the wiring and programming of a computerized mirror control box and alarm system. When the temperature of the mirror room changes, the tripod flexes. A computer programme could track the returned signal and correct the mirror's rotation speed and focal length. As well, when the mirror fails the system should send a text message or email which alerts the user.
6. Enclose the optical path figure 2.8 in PVC piping. The system will be more eye-safe if the beam is enclosed. Also, enclosing the system would prevent dust from settling on the up mirrors would extend their lifetime.

6.2.2 Software

1. Develop a new Picon data class for white light calibration data and add code to the Data Acquisition Computers which prompts for nightly calibration measurements and incorporates the measurements into the nightly data product.
2. Develop a code which will flag nights where the white light calibration constant deviates by more than 10% from the reference measurements which were determined during this campaign. This will ensure that the calibration derived in this work doesn't drift over the years.

6.2.3 Calibration

1. Run a second calibration campaign with ALVICE. Focus on CFH measurements and determining a correction Ξ_{sys} ($z > 9.5km$) which will allow for the validation of PCL of UTLS water vapour.
2. Compare newly calibrated PCL water vapour profiles to satellite measurements from ACE. There was an overpass on the night of June 8th.

Bibliography

- [1] PS Argall, RJ Sica, et al. A comparison of rayleigh and sodium lidar temperature climatologies. In *Annales geophysicae*, volume 25, pages 27–35, 2007.
- [2] PS Argall, ON Vassiliev, RJ Sica, and MM Mwangi. Lidar measurements taken with a large-aperture liquid mirror. 2. sodium resonance-fluorescence system. *Applied Optics*, 39(15):2393–2400, 2000.
- [3] A. Behrendt, T. Nakamura, M. Onishi, R. Baumgart, and T. Tsuda. Combined raman lidar for the measurement of atmospheric temperature, water vapor, particle extinction coefficient, and particle backscatter coefficient. *Applied optics*, 41(36):7657–7666, 2002.
- [4] A. Berk. Bernstein. ls & robertson. dc (1989) modtran: a moderate resolution model for lowtran 7. *Geophysics Laboratory, Air Force Command, US Air Force, Hanscom AFB, MA, USA*, 2012.
- [5] C. F. Bohren and B. A. Albrecht. *Atmospheric Thermodynamics*. Oxford University Press, Oxford, 1998.
- [6] D. Bolton. The computation of equivalent potential temperature. *Monthly Weather Review*, 108:1046–1053, 1980.
- [7] EF Borra. The liquid-mirror telescope as a viable astronomical tool. *Journal of the Royal Astronomical Society of Canada*, 76:245–256, 1982.

- [8] EF Borra, L. Girard, S. Szapiel, LM Tremblay, E. Boily, et al. Liquid mirrors-optical shop tests and contributions to the technology. *The Astrophysical Journal*, 393:829–847, 1992.
- [9] F.J. Brousdaides and J.F. Morrissey. Improved humidity measurements with a redesigned radiosonde humidity duct. *Bulletin of the American Meteorological Society*, 52:870–957, 1971.
- [10] Chad Bryant. First measurements of upper tropospheric and lower stratospheric water vapour mixing ratios using the purple crow raman-scatter lidar. Master’s thesis, The University of Western Ontario, 1999.
- [11] A.L. Buck et al. New equations for computing vapor pressure and enhancement factor. *Journal of Applied Meteorology*, 20(12):1527–1532, 1981.
- [12] A.H. Carter and D.F. Styer. Classical and statistical thermodynamics. *American Journal of Physics*, 68:1158, 2000.
- [13] DJ Cziczo, DM Murphy, PK Hudson, and DS Thomson. Single particle measurements of the chemical composition of cirrus ice residue during crystal-face. *Journal of geophysical research*, 109(D4):D04201, 2004.
- [14] W.P. Elliott and D.J. Gaffen. On the utility of radiosonde humidity archives for climate studies. *Bulletin of the American Meteorological Society*, 72:1507–1520, 1991.
- [15] L. Elterman. A series of stratospheric temperature profiles obtained with the searchlight technique. *J. Geophys. Res.*, 58:519–530, 1953.
- [16] P.J. Flatau, R.L. Walko, and W.R. Cotton. Polynomial fits to saturation vapor pressure. *Journal of Applied Meteorology*, 31:1507–1507, 1992.
- [17] D.J. Gaffen. Temporal inhomogeneities in radiosonde temperature records. *JOURNAL OF GEOPHYSICAL RESEARCH-ALL SERIES-*, 99:3667–3667, 1994.

- [18] E. Hecht. *Schaum's Outline of Optics*. McGraw-Hill Companies, 1974.
- [19] R. Hecht-Nielsen. Counterpropagation networks. *Applied optics*, 26(23):4979–4983, 1987.
- [20] W.K. Hocking. *Water in the Atmosphere*. UWO Course Materials, 2012.
- [21] J.R. Holton, P.H. Haynes, M.E. McIntyre, A.R. Douglass, R.B. Rood, and L. Pfister. Stratosphere-troposphere exchange. *Reviews of Geophysics*, 33(4):403–440, 1995.
- [22] FJ Immler, J. Dykema, T. Gardiner, DN Whiteman, PW Thorne, and H. Vömel. Reference quality upper-air measurements: guidance for developing gruan data products. *Atmospheric Measurement Techniques*, 3:1217–1231, 2010.
- [23] Solomon S. Rosenlof Karen H. Portmann Robert W. Daniel John S. Davis Sean M. Sanford Todd J. and Plattner Gian-Kasper. Contributions of stratospheric water vapor to decadal changes in the rate of global warming. *Science*, 327(5970):1219–1223, 2010.
- [24] E. Sunderland Jacob D.J. J. A. Logan, L. J. Mickley. Harvard atmospheric chemistry modeling group website. *Internet*, 2012.
- [25] Solomon S. Qin D. Manning M. Alley RB Berntsen T. Bindoff NL Chen Z. Chidthaisong A. Gregory JM, Hegerl GC, et al. Technical summary. *WMO Report*, 2007.
- [26] A.J. Krueger and R.A. Minzner. A mid-latitude ozone model for the 1976 us standard atmosphere. *Journal of Geophysical Research*, 81(24):4477–4481, 1976.
- [27] T. Leblanc and I.S. McDermid. Accuracy of raman lidar water vapor calibration and its applicability to long-term measurements. *Applied optics*, 47(30):5592–5603, 2008.
- [28] T. Leblanc, IS McDermid, J. Howe, R. Aspey, TD Walsh, H. Vomel, TG McGee, L. Twigg, G. Sumnicht, D. Whiteman, et al. P1. 5 measurements of humidity in the atmosphere: Validation experiments (mohave) overview of the campaign and first results. *Meas. Tech. Discuss*, 2009.

- [29] T. Leblanc, TD Walsh, IS Mcdermid, GC Toon, J.F. Blavier, B. Haines, WG Read, B. Herman, E. Fetzer, S. Sander, et al. Measurements of humidity in the atmosphere and validation experiments (mohave)-2009: overview of campaign operations and results. *Atmospheric Measurement Techniques*, 4:2579–2605, 2011.
- [30] D.R. Lide. *CRC handbook of chemistry and physics*. CRC press, 2012.
- [31] Litron. *Litron Laser Manual*. Litron, 2010.
- [32] J. Marti and K. Mauersberger. A survey and new measurements of ice vapor pressure at temperatures between 170 and 250k. *Geophysical research letters*, 20(5):363–366, 1993.
- [33] IS McDermid, T. Leblanc, and TD Walsh. Ground-based water vapor raman lidar measurements up to the upper troposphere and lower stratosphere—part 1: Instrument development, optimization, and validation, atmos. *Meas. Tech. Discuss*, 4:5079–5109, 2011.
- [34] R. M. Measures. *Laser Remote Sensing Fundamentals and Applications*. Krieger Publishing Co., Malabar, 1984.
- [35] L.M. Miloshevich, H. Vömel, D.N. Whiteman, and T. Leblanc. Accuracy assessment and correction of vaisala rs92 radiosonde water vapor measurements. *Journal of Geophysical Research*, 114(D11):D11305, 2009.
- [36] SB Mockler. Water vapor in the climate system, special report, american geophysical union (agu), 2000 florida ave., nw, washington, dc 20009. Technical report, ISBN 0-87590-865-9, 1995 (www.agu.org/sci_soc/mockler.html), 1995.
- [37] A. Moss, RJ Sica, E. McCullough, K. Strawbridge, K. Walker, and J. Drummond. Calibration and validation of water vapour lidar measurements from eureka, nunavut using radiosondes and the atmospheric chemistry experiment fourier transform spectrometer. *Meas. Tech. Discuss*, 5:5665–5689, 2012.

- [38] DM Murphy and T. Koop. Review of the vapour pressures of ice and supercooled water for atmospheric applications. *Quarterly Journal of the Royal Meteorological Society*, 131(608):1539–1565, 2006.
- [39] F.W. Murray. On the computation of saturation vapor pressure. *Journal of Applied Meteorology*, 6(1):203–204, 1967.
- [40] J. Nash, T. Oakley, H. Vömel, and LI Wei. Wmo intercomparison of high quality radiosonde systems, yangjiang, china, 12 july–3 august 2010. *WMO report*, 2011.
- [41] J. Nash, R. Smout, T. Oakley, B. Pathack, and S. Kurnosenko. Wmo intercomparison of high quality radiosonde systems vacoas, mauritius, 2–25 february 2005. *WMO Report. Available from CIMO*, 2005.
- [42] S.J. Oltmans, H. Vömel, D.J. Hofmann, K.H. Rosenlof, and D. Kley. The increase in stratospheric water vapor from balloonborne, frostpoint hygrometer measurements at washington, dc, and boulder, colorado. *Geophysical research letters*, 27:3453–3456, 2000.
- [43] Edmund Optics. Part nt86-367. *Internet*, 2012.
- [44] J. Ovarlez, J.F. Gayet, K. Gierens, J. Ström, H. Ovarlez, F. Auriol, R. Busen, and U. Schumann. Water vapour measurements inside cirrus clouds in northern and southern hemispheres during inca. *Geophysical research letters*, 29(16):1813, 2002.
- [45] W.H. Press, S.A. Teukolsky, W.T. Vetterling, and B.P. Flannery. *Numerical recipes 3rd edition: The art of scientific computing*. Cambridge University Press, 2007.
- [46] E. Raschke. *Radiation and water in the climate system Remote Measurement Book*. Springer-Verlag Berlin Heidelberg, 1996.
- [47] D. Rosenfeld and W.L. Woodley. Deep convective clouds with sustained supercooled liquid water down to -37.5°C . *Nature*, 405(6785):440–442, 2000.

- [48] HW Schrötter and HW Klöckner. Raman scattering cross sections in gases and liquids. *Raman spectroscopy of gases and liquids*, 11:130–138, 1979.
- [49] C.Y. She. Spectral structure of laser light scattering revisited: bandwidths of nonresonant scattering lidars. *Applied Optics*, 40(27):4875–4884, 2001.
- [50] T. Shibata, H. Vömel, S. Hamdi, S. Kaloka, F. Hasebe, M. Fujiwara, and M. Shiotani. Tropical cirrus clouds near cold point tropopause under ice supersaturated conditions observed by lidar and balloon-borne cryogenic frost point hygrometer. *Journal of geophysical research*, 112(D3):D03210, 2007.
- [51] RJ Sica, S. Sargoytchev, PS Argall, EF Borra, L. Girard, CT Sparrow, and S. Flatt. Lidar measurements taken with a large-aperture liquid mirror. 1. rayleigh-scatter system. *Applied optics*, 34(30):6925–6936, 1995.
- [52] A.E. Siegman. Laser beams and resonators: beyond the 1960s. *Selected Topics in Quantum Electronics, IEEE Journal of*, 6(6):1389–1399, 2000.
- [53] Marcos Algara Siller. Purple crow lidar calibration of water vapour mixing ratios in the lower atmosphere. Master’s thesis, The University of Western Ontario, 2004.
- [54] Bernhard Stein. R9880-20 pmt conversion table. *Internet*, 2012.
- [55] Ahmed Suliman. R5600p-01 best estimate. *Internet*, 2012.
- [56] CPC NDACC Web Team. Network for the detection of atmospheric composition change (ndacc). *Internet*, 2012.
- [57] ThorLabs. Part dmlp605. *Internet*, 2012.
- [58] A.A. Tsonis. *An introduction to atmospheric thermodynamics*. Cambridge University Press, 2002.
- [59] Unknown. Sciencecity. *Internet*, 2012.

- [60] Unknown. Special optics. *Internet*, 2012.
- [61] Unknown. Wikipedia. *Internet*, 2012.
- [62] H. Vömel, DE David, and K. Smith. Accuracy of tropospheric and stratospheric water vapor measurements by the cryogenic frost point hygrometer: Instrumental details and observations. *Journal of geophysical research*, 112(D8):D08305, 2007.
- [63] H. Vömel, V. Yushkov, S. Khaykin, L. Korshunov, E. Kyrö, and R. Kivi. Intercomparisons of stratospheric water vapor sensors: Flash-b and noaa/cmnl frost-point hygrometer. *Journal of Atmospheric and Oceanic Technology*, 24(6):941–952, 2007.
- [64] Holger Vomel. Special optics. *Internet*, 2012.
- [65] Hyland R. W. and A. Wexler. Formulations for the thermodynamic properties of the saturated phases of h₂o from 173.15k to 473.15k. *ASHRAE Trans.*, 89(2A):500–519, 1983.
- [66] C.G. Wade. An evaluation of problems affecting the measurement of low relative humidity on the united states radiosonde. *Journal of Atmospheric and Oceanic Technology*, 11(3):687–700, 1994.
- [67] W. Wagner and A. Pruss. The iapws formulation 1995 for the thermodynamic properties of ordinary water substance for general and scientific use. *Journal of Physical and Chemical Reference Data*, 31(2):387–536, 2002.
- [68] J.M. Wallace and P.V. Hobbs. *Atmospheric science: an introductory survey*, volume 92. Academic press, 2006.
- [69] U. Wandinger and A. Ansmann. Experimental determination of the lidar overlap profile with raman lidar. *Applied optics*, 41(3):511–514, 2002.
- [70] A. Wexler. Vapor pressure formulation for ice. *Journal of Research of the National Bureau of Standards–A. Physics and Chemistry*, 81(1):5–19, 1977.

- [71] Dave Whiteman. Ndacc lidar. *Internet*, 2012.
- [72] DN Whiteman, B. Demoz, K. Rush, G. Schwemmer, B. Gentry, P. Di Girolamo, J. Comer, I. Veselovskii, K. Evans, SH Melfi, et al. Raman lidar measurements during the international h2o project. part i: Instrumentation and analysis techniques. *Journal of Atmospheric and Oceanic Technology*, 23(2):157–169, 2006.
- [73] DN Whiteman, SH Melfi, and RA Ferrare. Raman lidar system for the measurement of water vapor and aerosols in the earths atmosphere. *Applied Optics*, 31(16):3068–3082, 1992.

Appendix A

Campaign Data

A.1 May 24th 2012

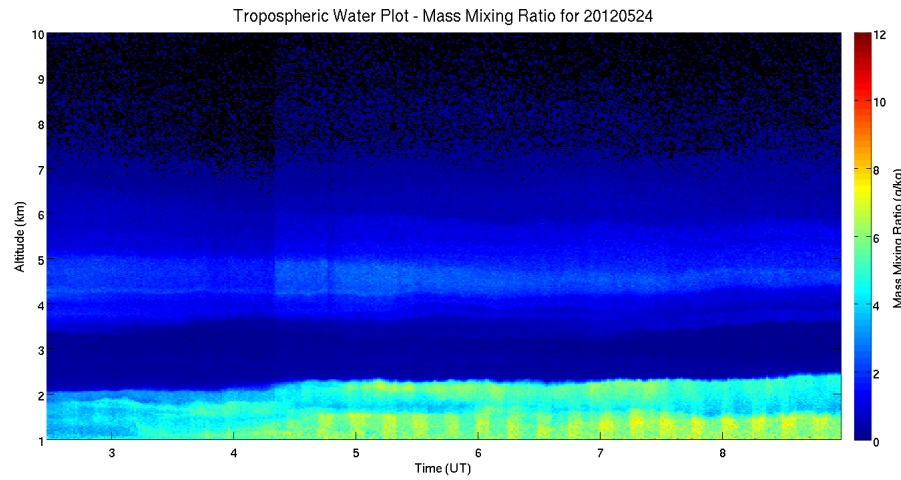


Figure A.1: PCL nightly colour plot of tropospheric water for May 24th.

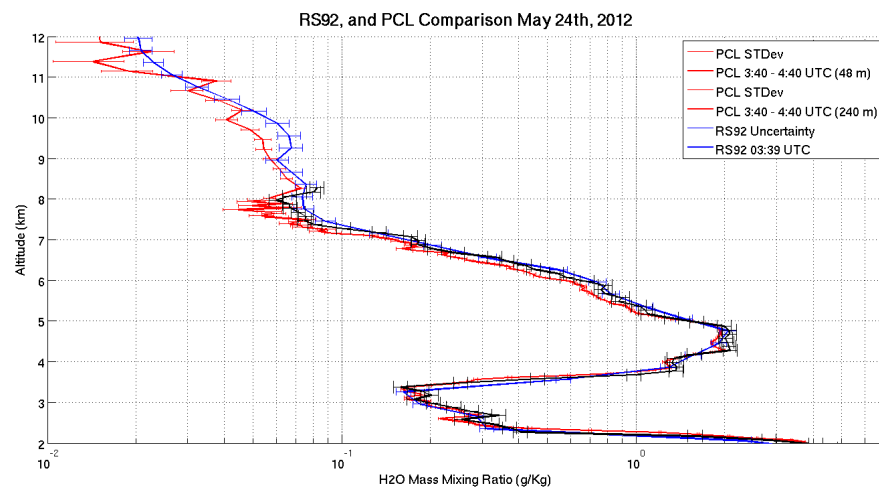


Figure A.2: PCL, ALVICE, and RS92 mass mixing ratio profiles for May 24th at 3:39 UTC.

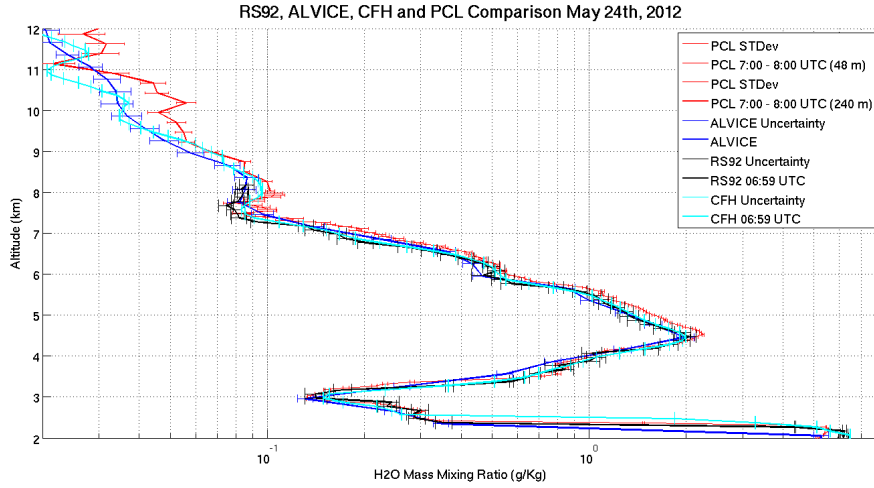


Figure A.3: PCL, ALVICE, RS92, and CFH mass mixing ratio profiles for May 24th at 6:59 UTC.

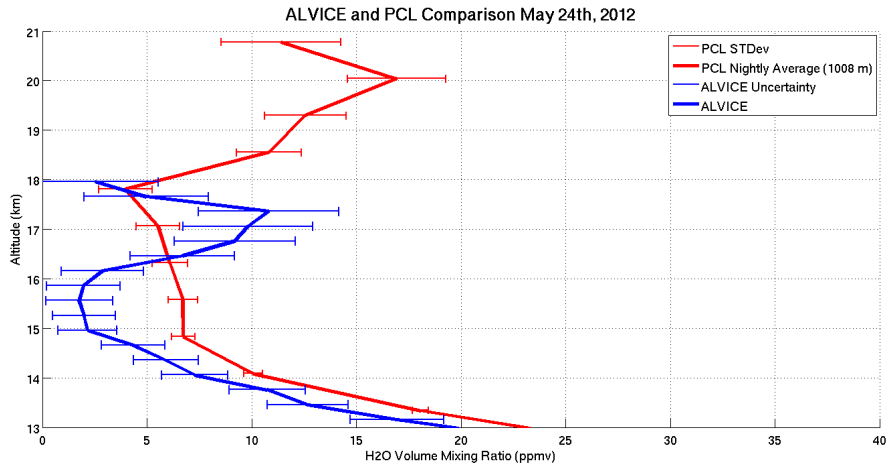


Figure A.4: PCL and ALVICE volume mixing ratio profiles for May 24th at 3:39 UTC.

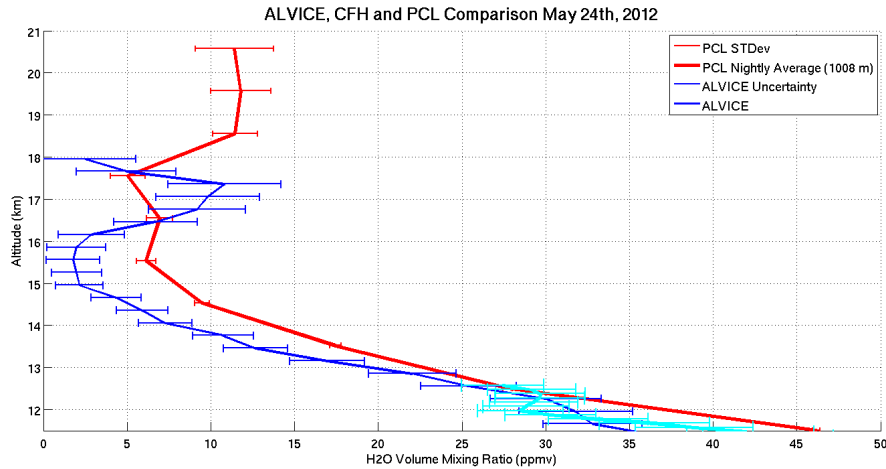


Figure A.5: PCL, ALVICE, and CFH volume mixing ratio profiles for May 24th at 6:59 UTC.

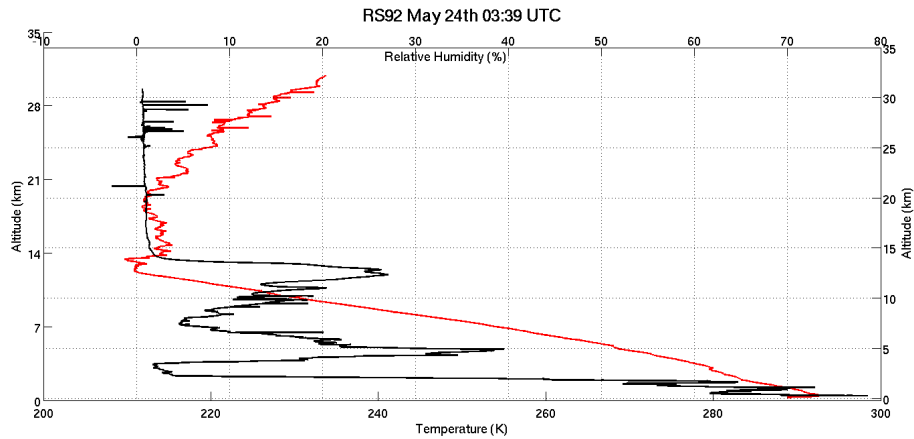


Figure A.6: RS92 profiles for temperature (red) and RH (black) on May 24th at 3:39 UTC.

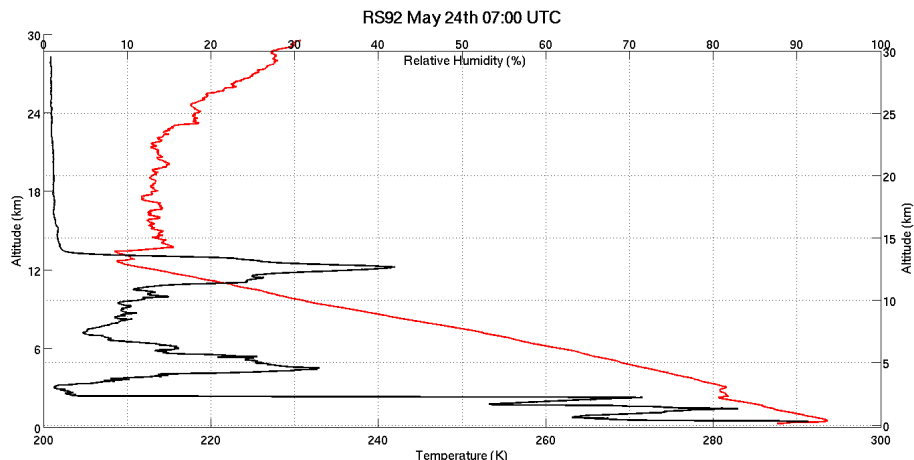


Figure A.7: RS92 profiles for temperature (red) and RH (black) on May 24th at 6:59 UTC.

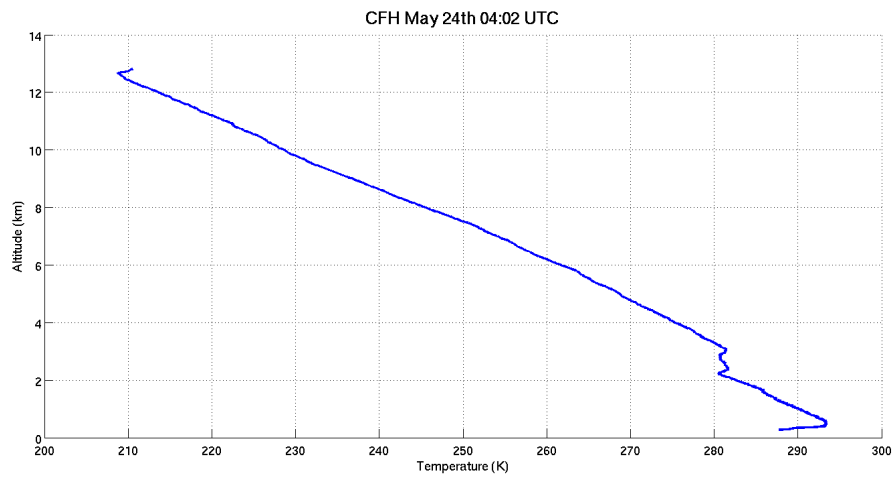


Figure A.8: CFH profile for temperature on May 24th at 4:02 UTC.

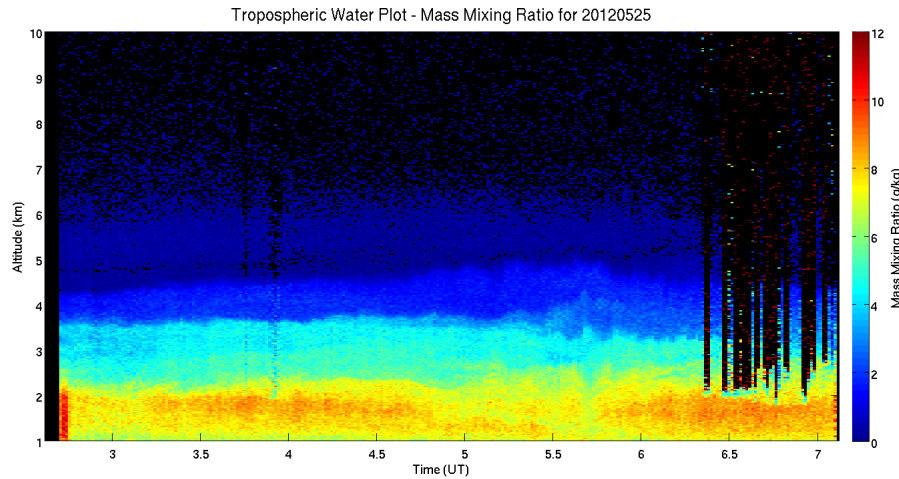


Figure A.9: PCL nightly colour plot of tropospheric water for May 25th.

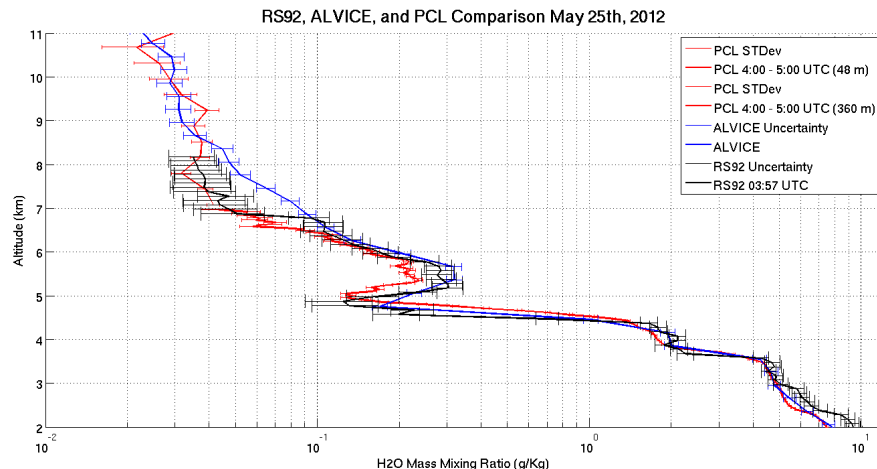


Figure A.10: PCL, ALVICE, and RS92 mass mixing ratio profiles for May 25th at 3:57 UTC.

A.2 May 25th 2012

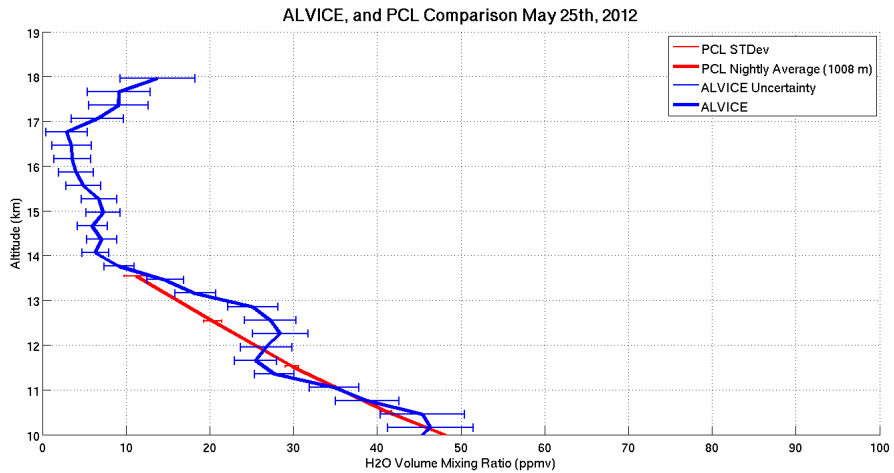


Figure A.11: PCL and ALVICE volume mixing ratio profiles for May 25th at 3:57 UTC.

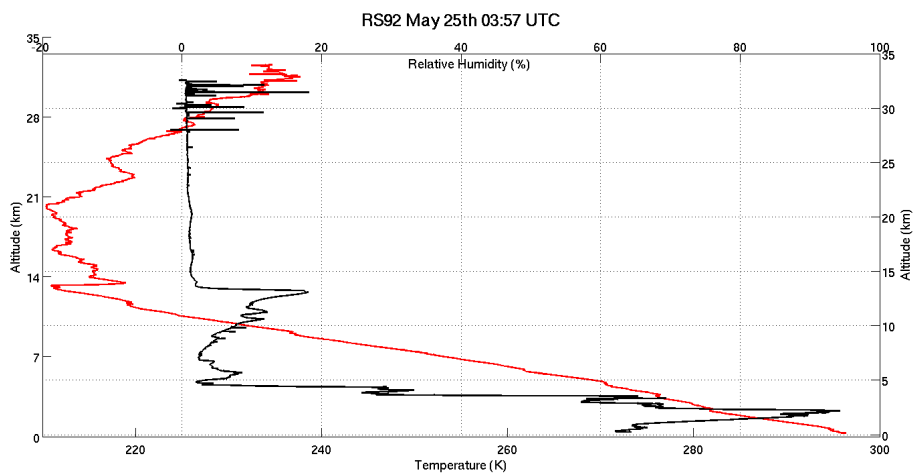


Figure A.12: RS92 profiles for temperature (red) and RH (black) on May 25th at 3:57 UTC.

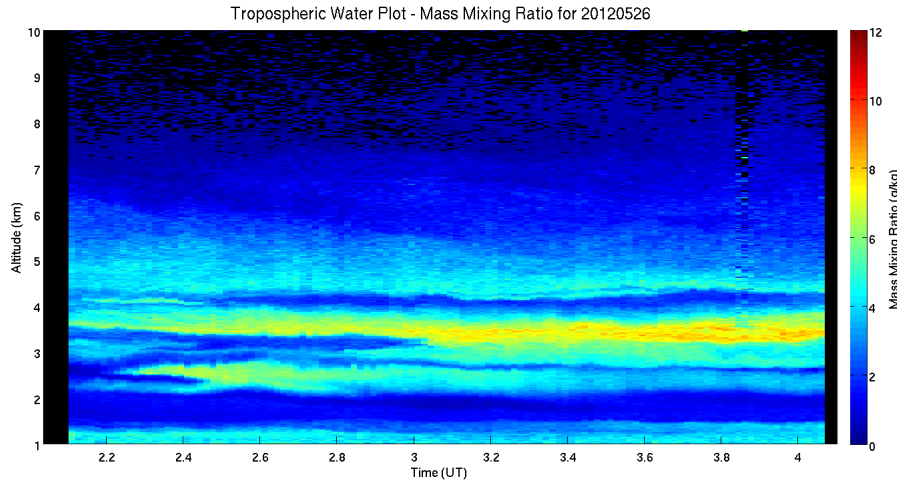


Figure A.13: PCL nightly colour plot of tropospheric water for May 26th.

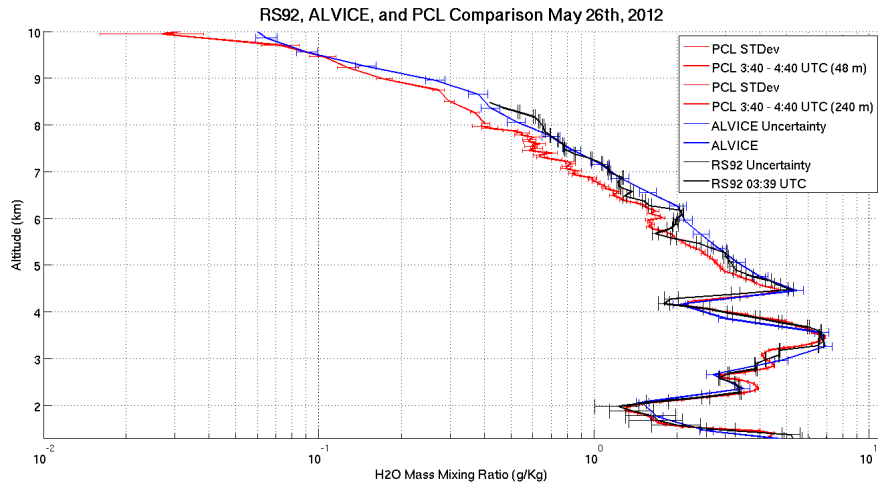


Figure A.14: PCL, ALVICE, and RS92 mass mixing ratio profiles for May 26th at 3:39 UTC.

A.3 May 26th 2012

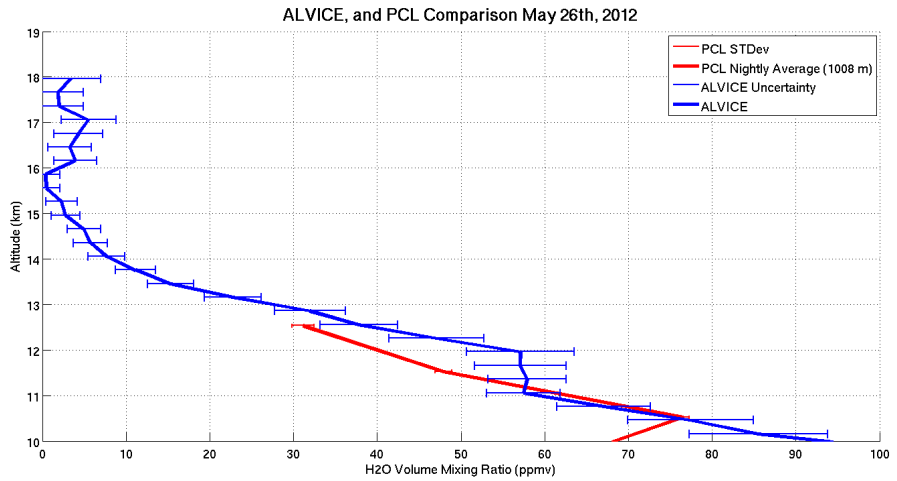


Figure A.15: PCL and ALVICE volume mixing ratio profiles for May 26th at 3:39 UTC.

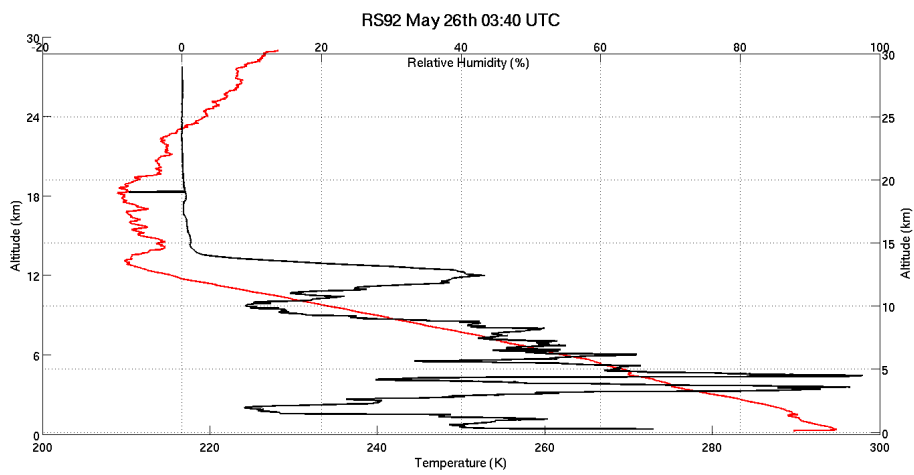


Figure A.16: RS92 profiles for temperature (red) and RH (black) on May 26th at 3:40 UTC.

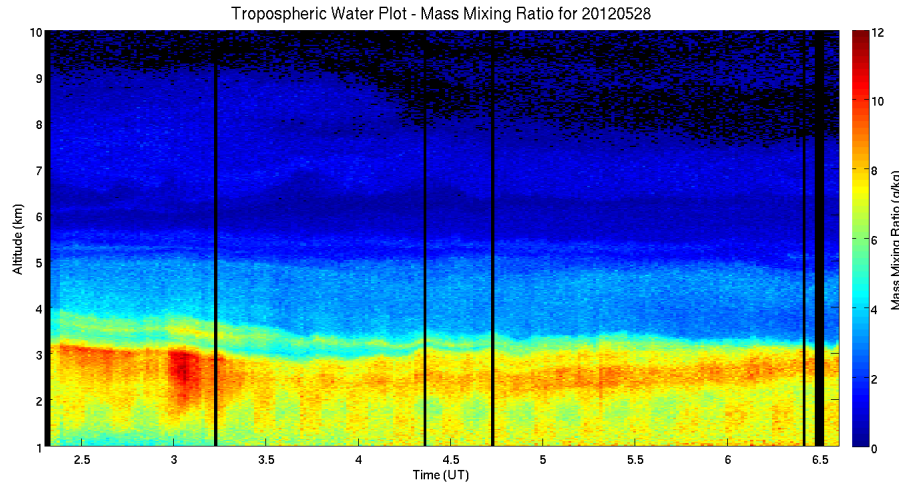


Figure A.17: PCL nightly colour plot of tropospheric water for May 28th.

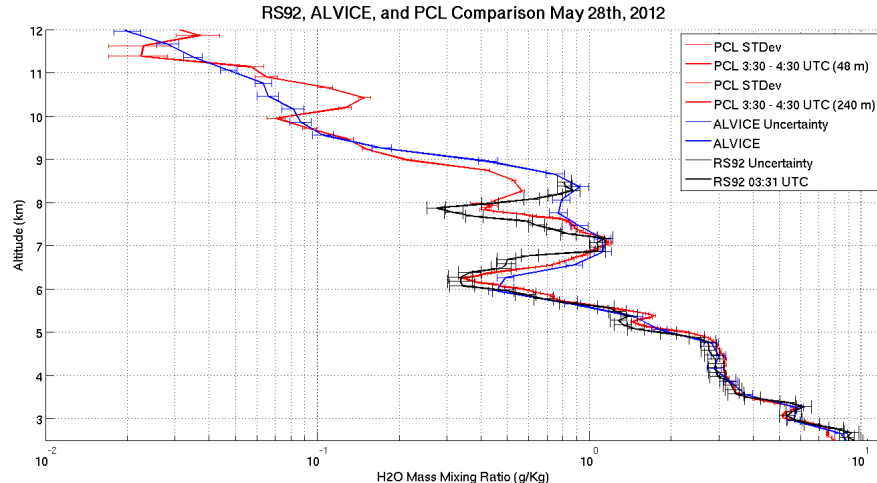


Figure A.18: PCL, ALVICE, and RS92 mass mixing ratio profiles for May 28th at 3:31 UTC.

A.4 May 28th 2012

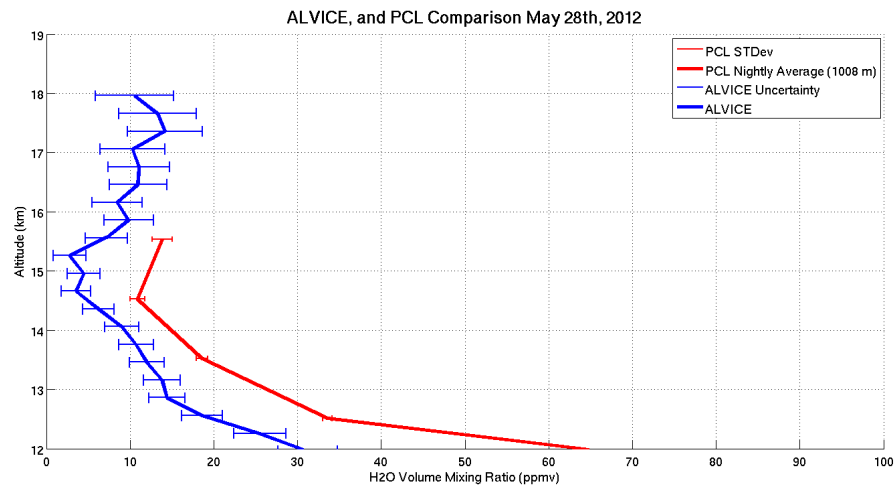


Figure A.19: PCL and ALVICE volume mixing ratio profiles for May 28th at 3:31 UTC.

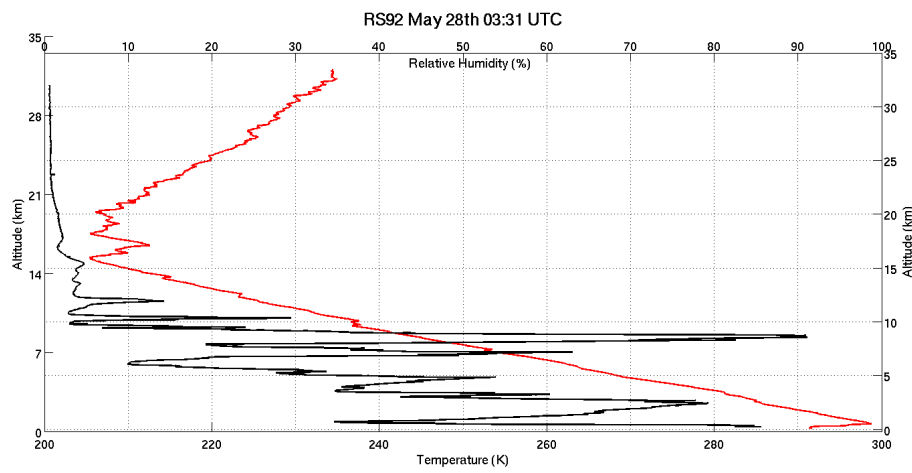


Figure A.20: RS92 profiles for temperature (red) and RH (black) on May 28th at 3:31 UTC.

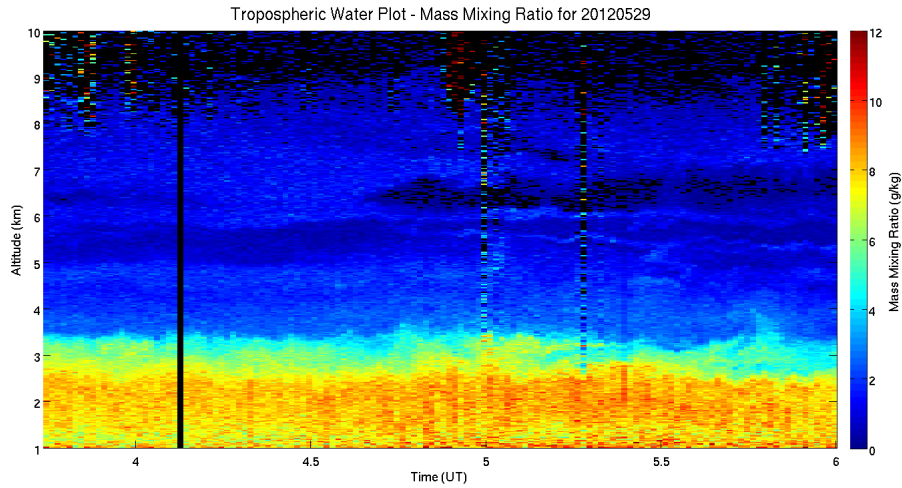


Figure A.21: PCL nightly colour plot of tropospheric water for May 29th.

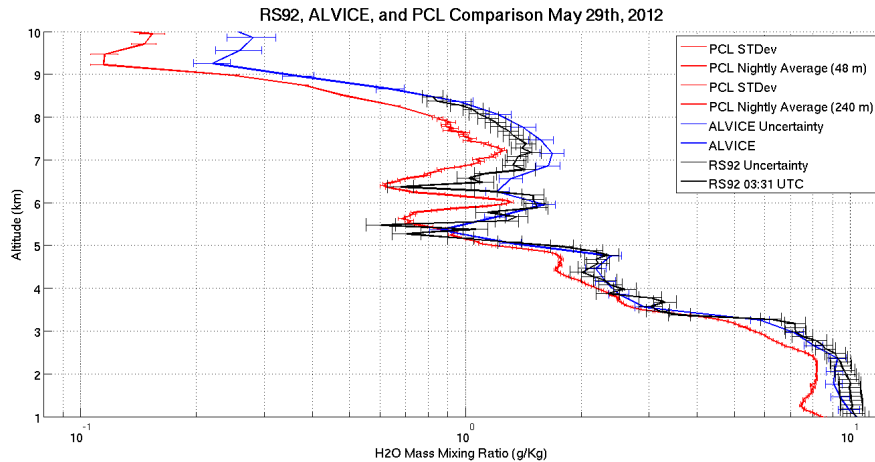


Figure A.22: PCL, ALVICE, and RS92 mass mixing ratio profiles for May 29th at 3:31 UTC.

A.5 May 29th 2012

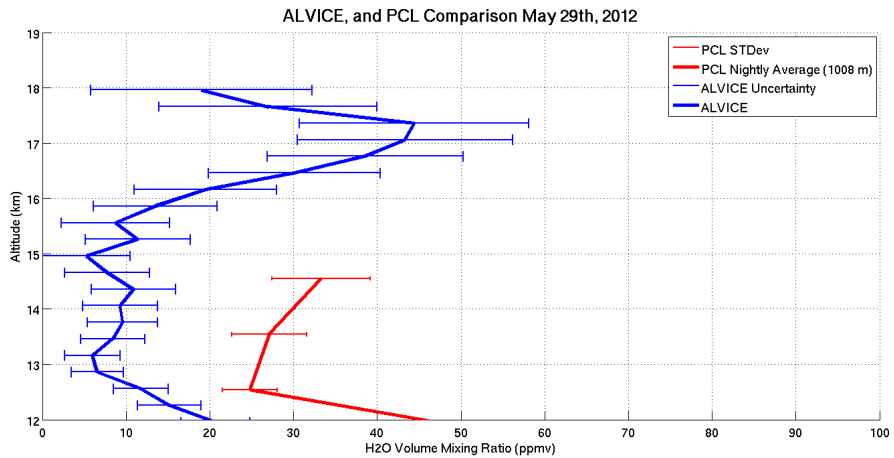


Figure A.23: PCL and ALVICE volume mixing ratio profiles for May 29th at 3:31 UTC.

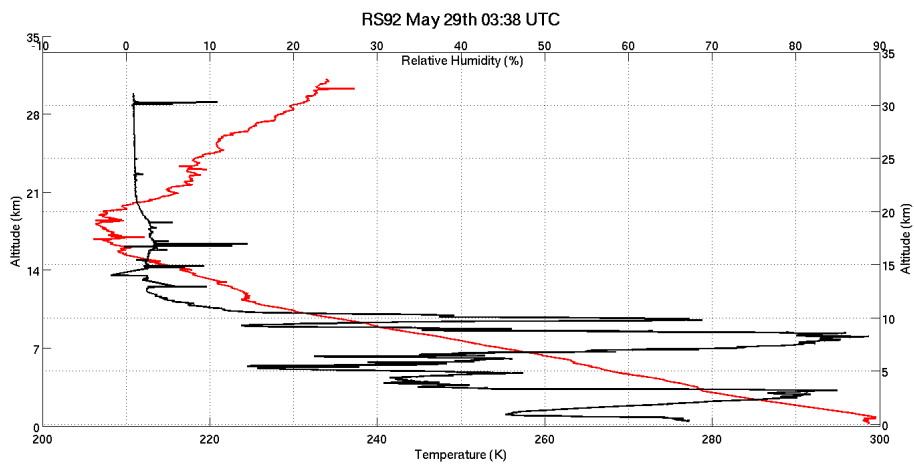


Figure A.24: RS92 profiles for temperature (red) and RH (black) on May 29th at 3:38 UTC.

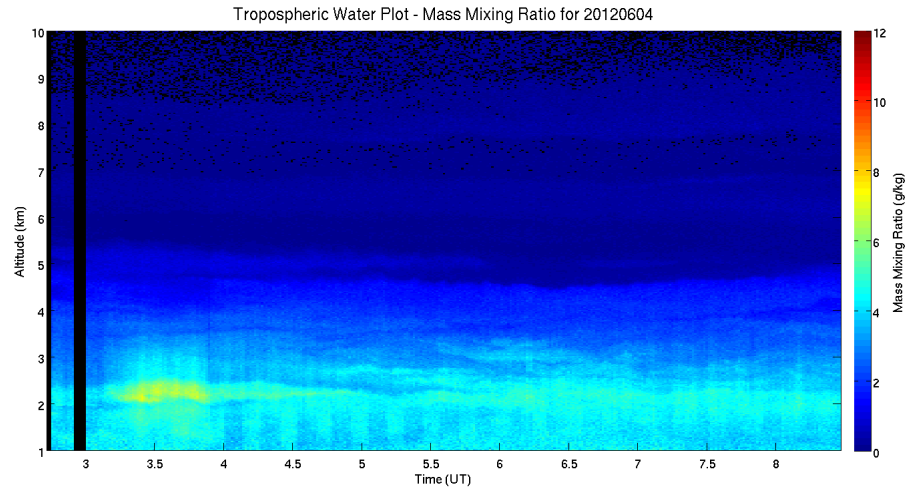


Figure A.25: PCL nightly colour plot of tropospheric water for June 4th.

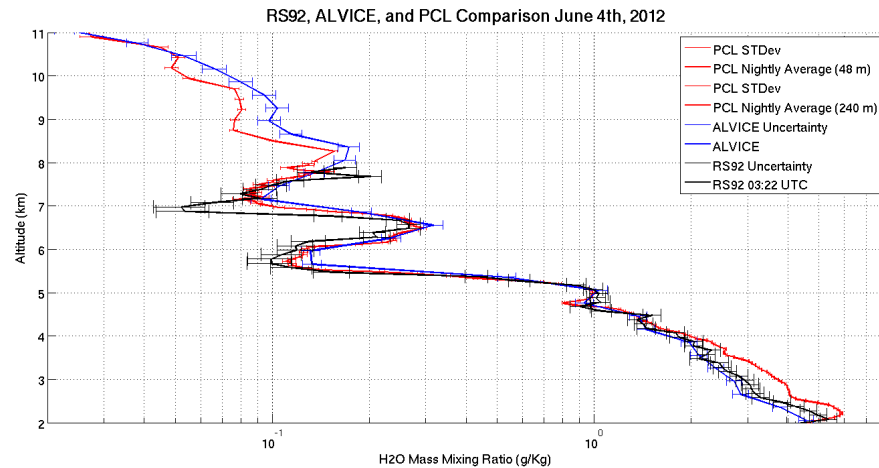


Figure A.26: PCL, ALVICE, and RS92 mass mixing ratio profiles for June 4th at 3:22 UTC.

A.6 June 4th 2012

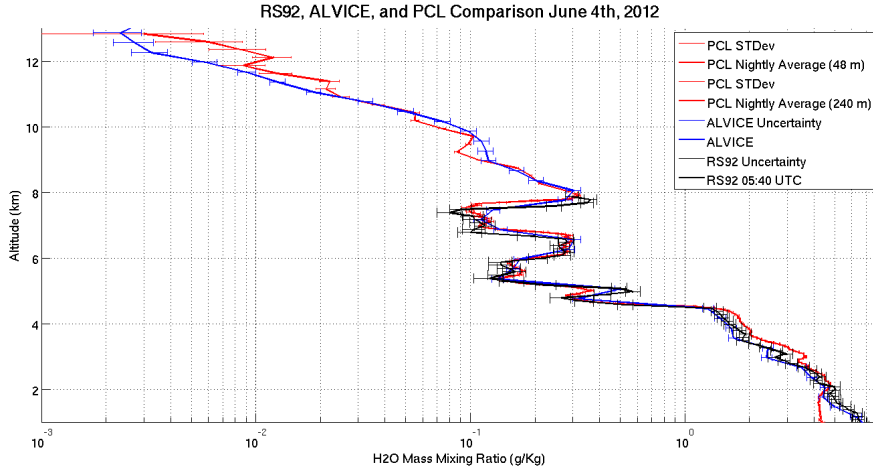


Figure A.27: PCL,ALVICE, and RS92 mass mixing ratio profiles for June 4th at 5:40 UTC.

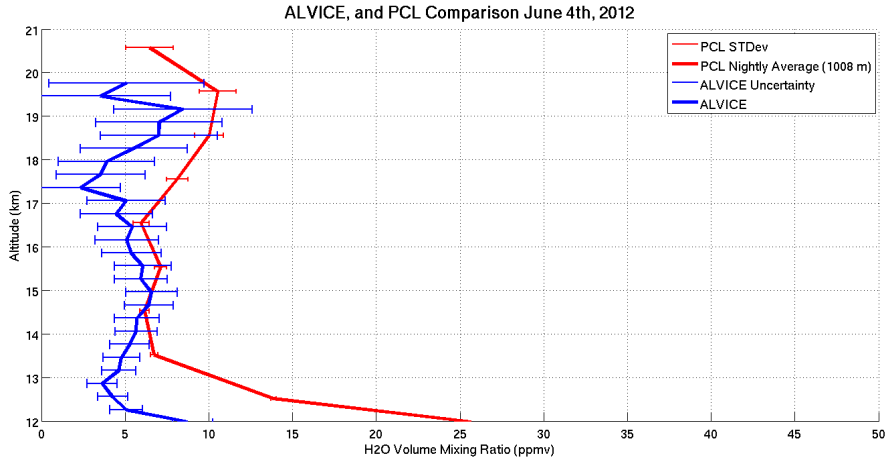


Figure A.28: PCL and ALVICE volume mixing ratio profiles for June 4th at 3:22 UTC.

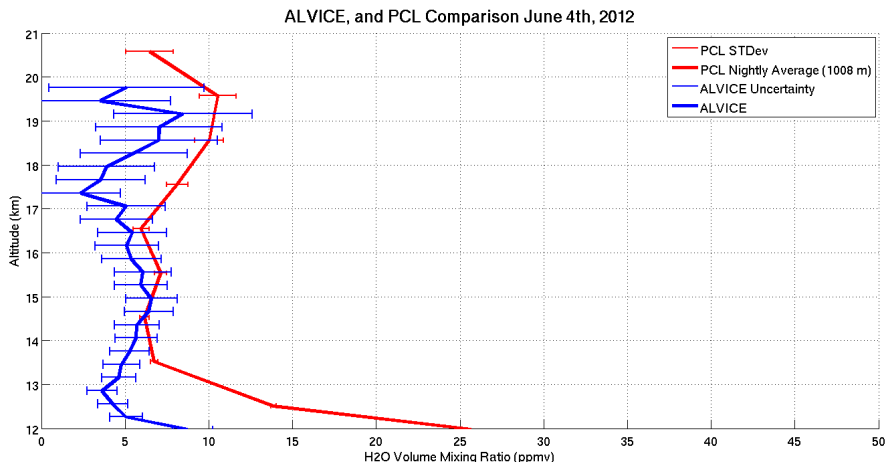


Figure A.29: PCL and ALVICE volume mixing ratio profiles for June 4th at 5:40 UTC.

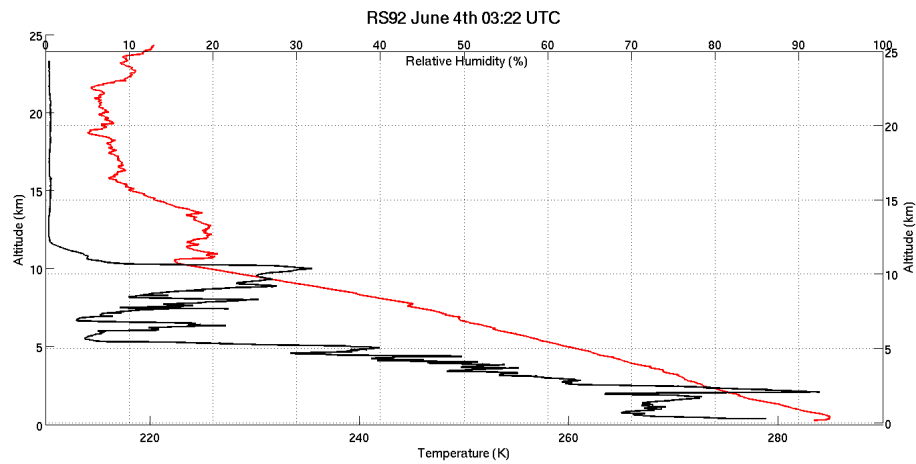


Figure A.30: RS92 profiles for temperature (red) and RH (black) on June 4th at 3:22 UTC.

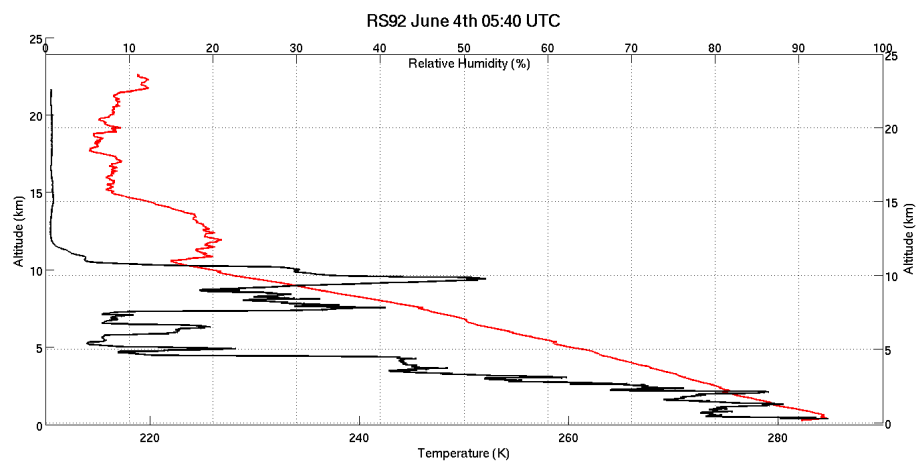


Figure A.31: RS92 profiles for temperature (red) and RH (black) on June 4th at 5:40 UTC.

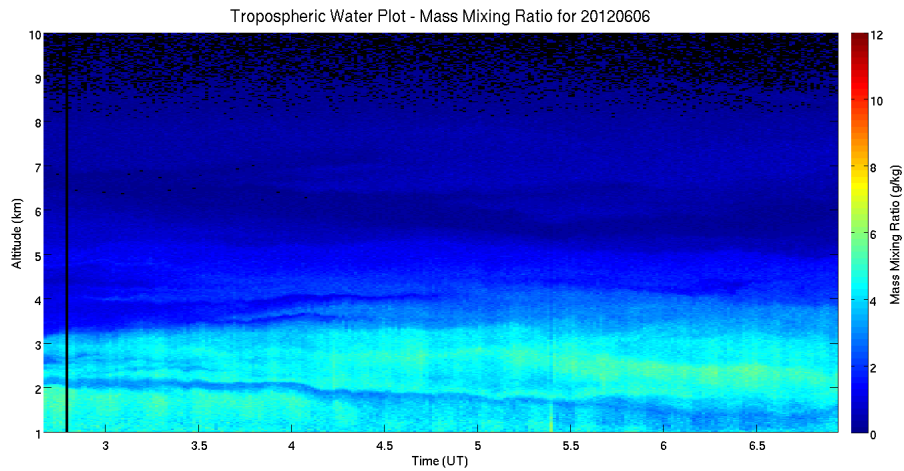


Figure A.32: PCL nightly colour plot of tropospheric water for June 6th.

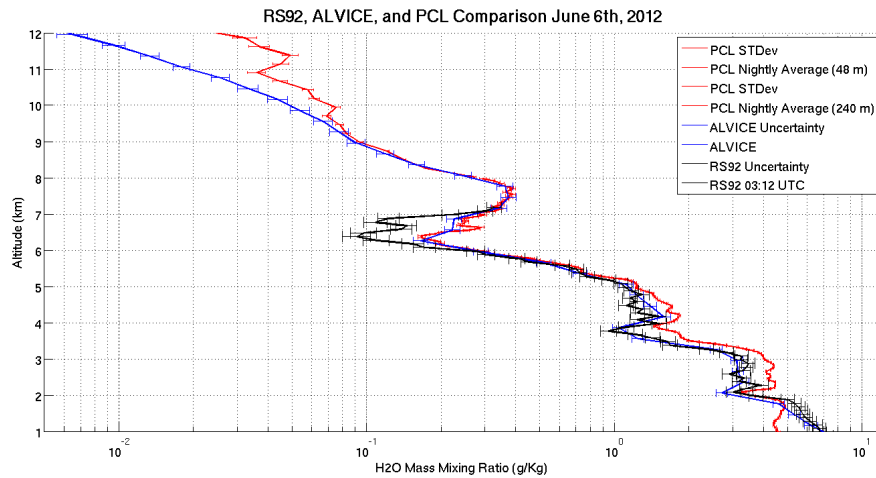


Figure A.33: PCL, ALVICE, and RS92 mass mixing ratio profiles for June 6th at 3:12 UTC.

A.7 June 6th 2012

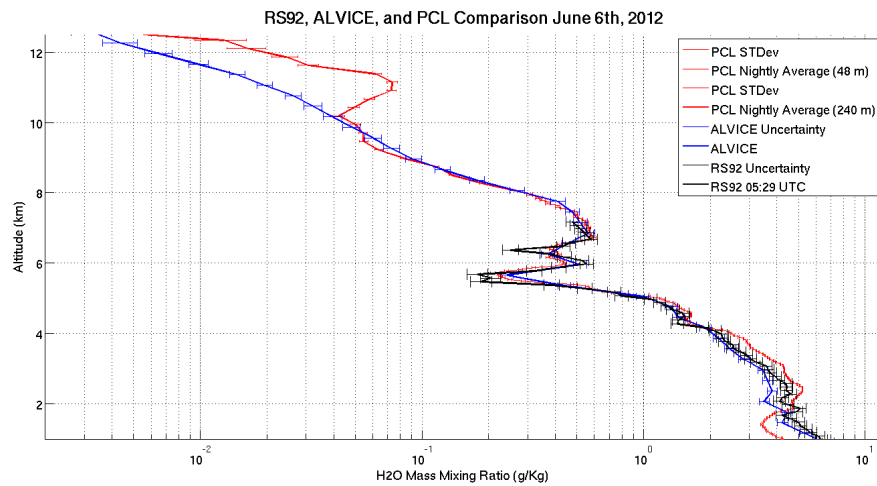


Figure A.34: PCL,ALVICE, and RS92 mass mixing ratio profiles for June 6th at 5:29 UTC.

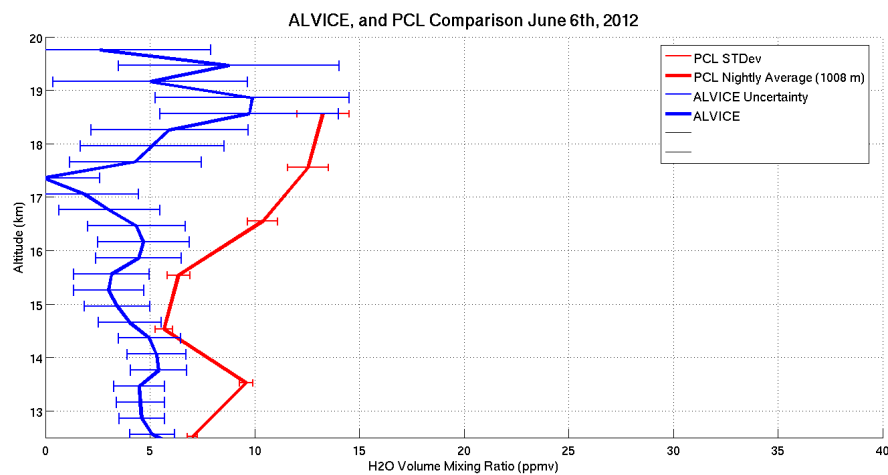


Figure A.35: PCL and ALVICE volume mixing ratio profiles for June 6th at 3:12 UTC.

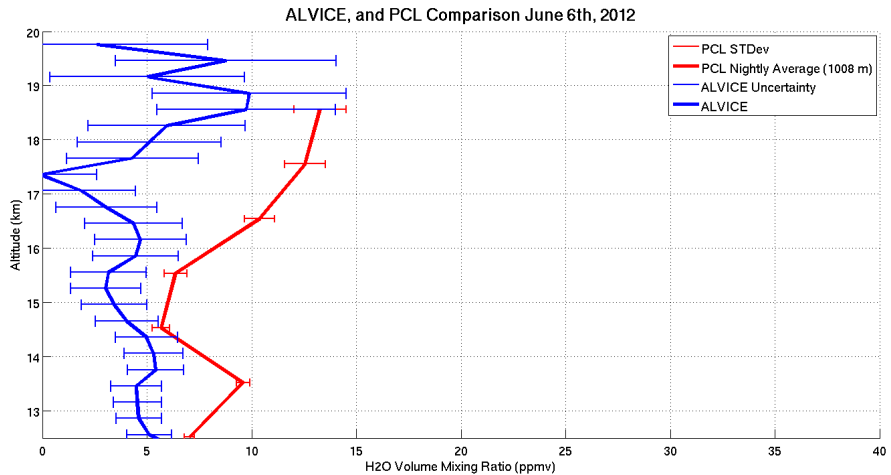


Figure A.36: PCL and ALVICE volume mixing ratio profiles for June 6th at 5:29 UTC.

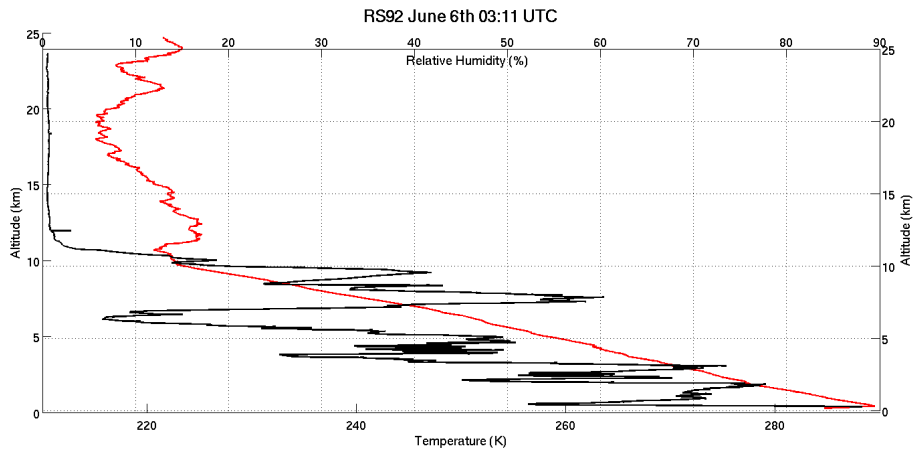


Figure A.37: RS92 profiles for temperature (red) and RH (black) on June 6th at 3:11 UTC.

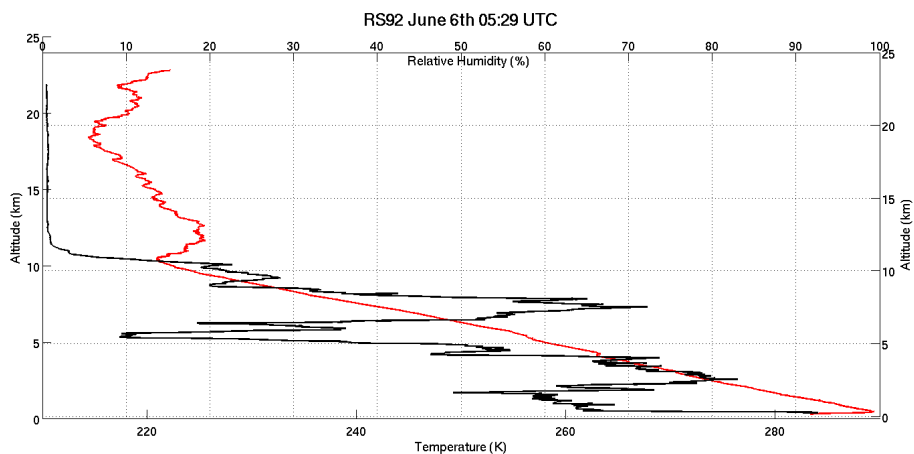


Figure A.38: RS92 profiles for temperature (red) and RH (black) on June 6th at 5:29 UTC.

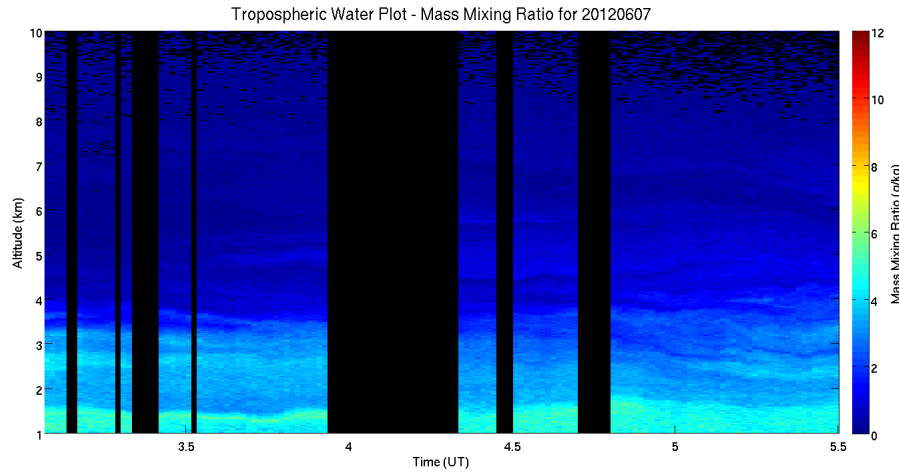


Figure A.39: PCL nightly colour plot of tropospheric water for June 7th.

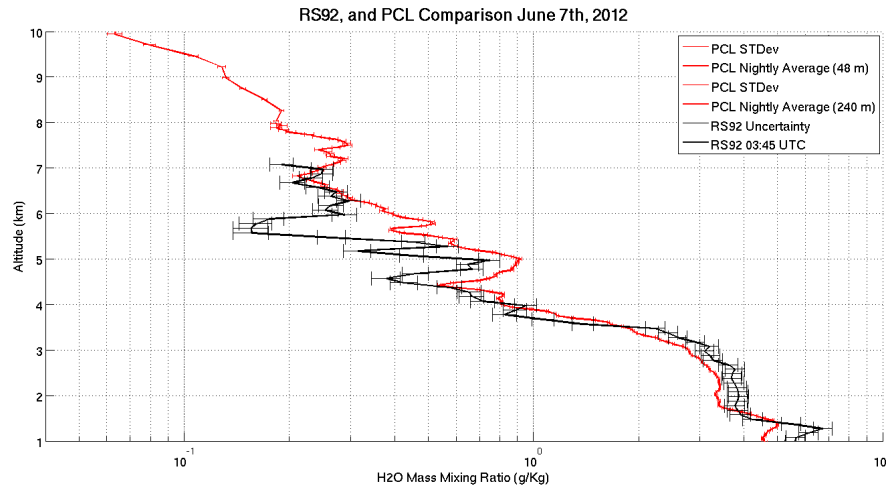


Figure A.40: PCL and RS92 mass mixing ratio profiles for June 7th at 3:45 UTC.

A.8 June 7th 2012

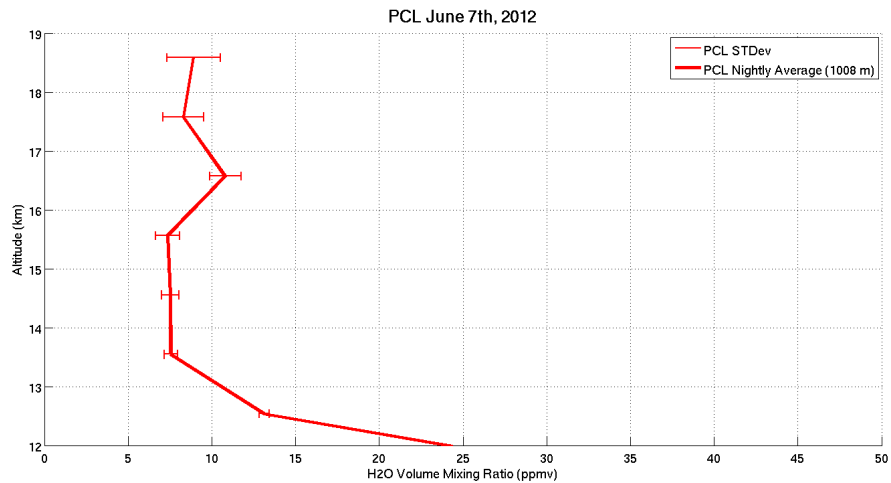


Figure A.41: PCL volume mixing ratio profiles for June 6th at 3:45 UTC.

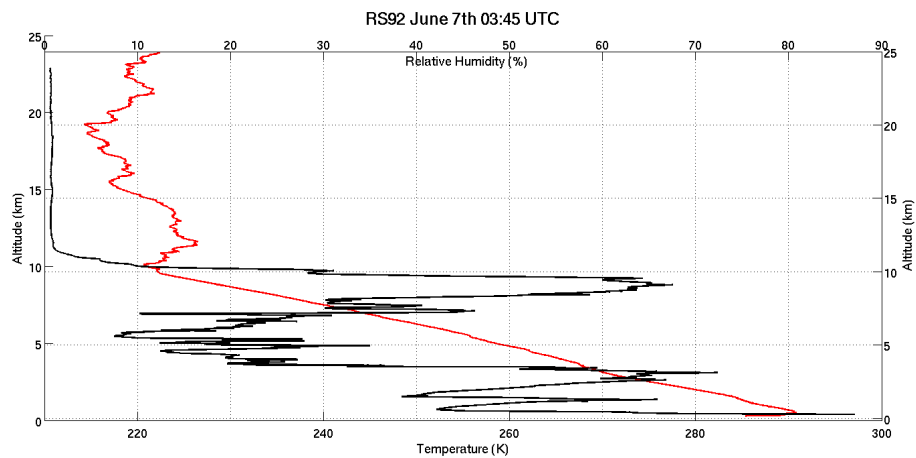


Figure A.42: RS92 profiles for temperature (red) and RH (black) on June 7th at 3:45 UTC.

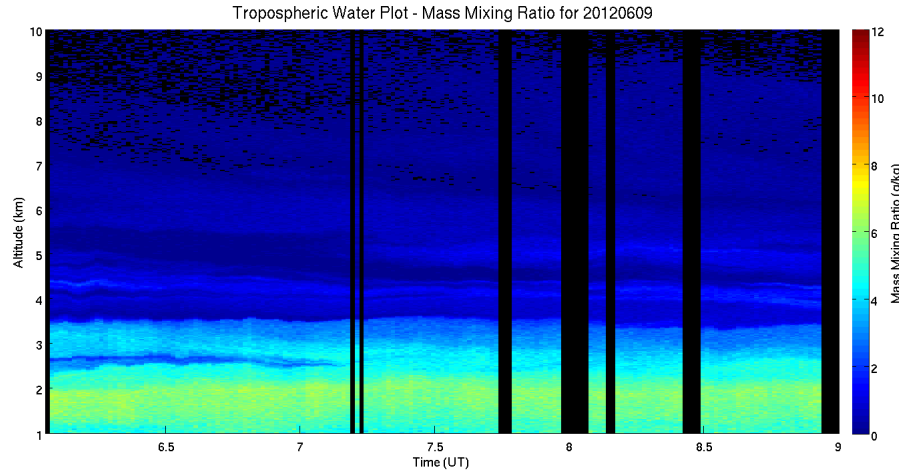


Figure A.43: PCL nightly colour plot of tropospheric water for June 8th.

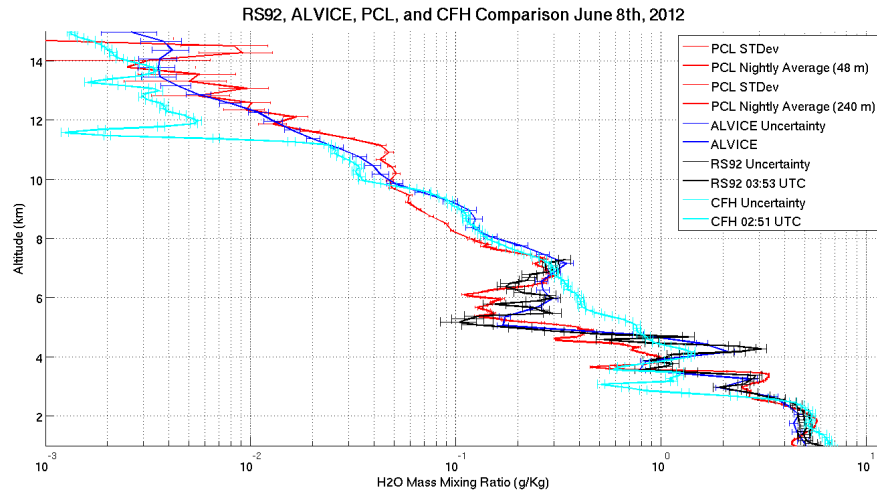


Figure A.44: PCL,ALVICE, and RS92 mass mixing ratio profiles for June 8th at 3:53 UTC.

A.9 June 8th 2012

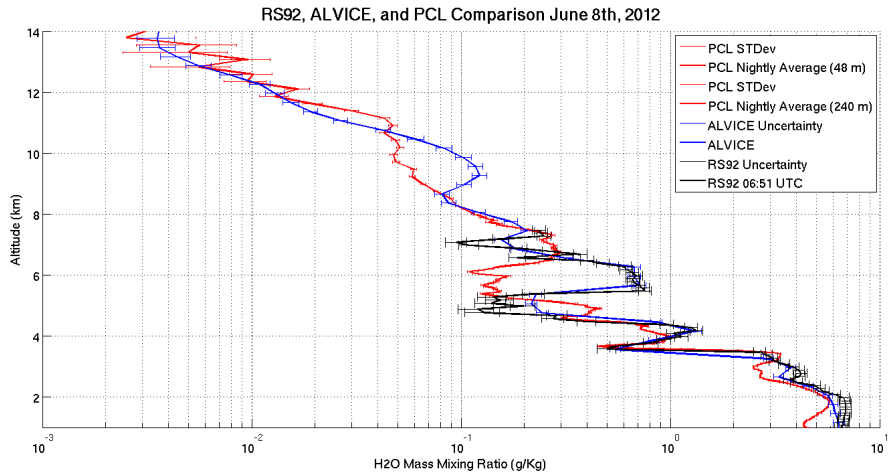


Figure A.45: PCL,ALVICE, RS92, and CFH mass mixing ratio profiles for June 8th at 6:51 UTC.

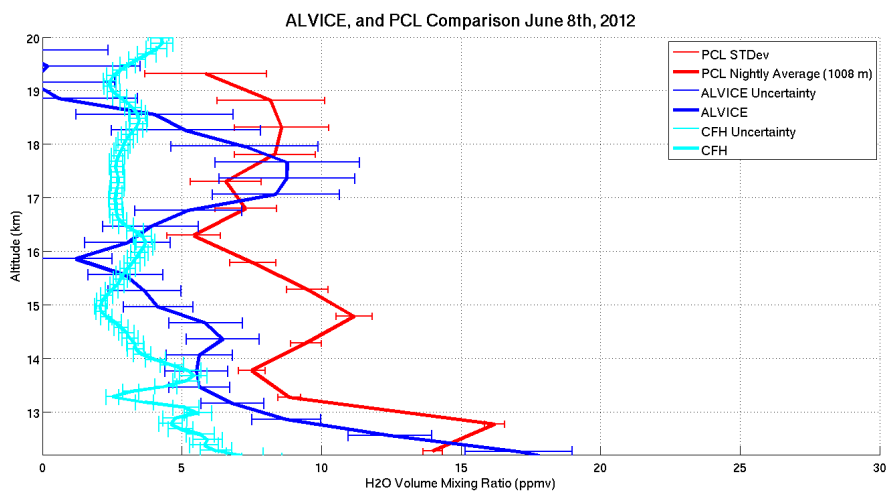


Figure A.46: PCL, ALVICE, and CFH volume mixing ratio profiles for June 8th at 3:53 UTC.

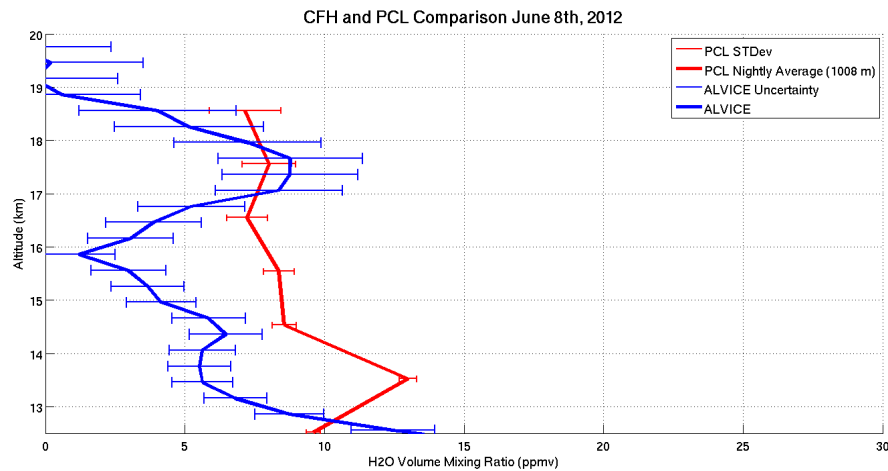


Figure A.47: PCL and ALVICE volume mixing ratio profiles for June 8th at 6:51 UTC.

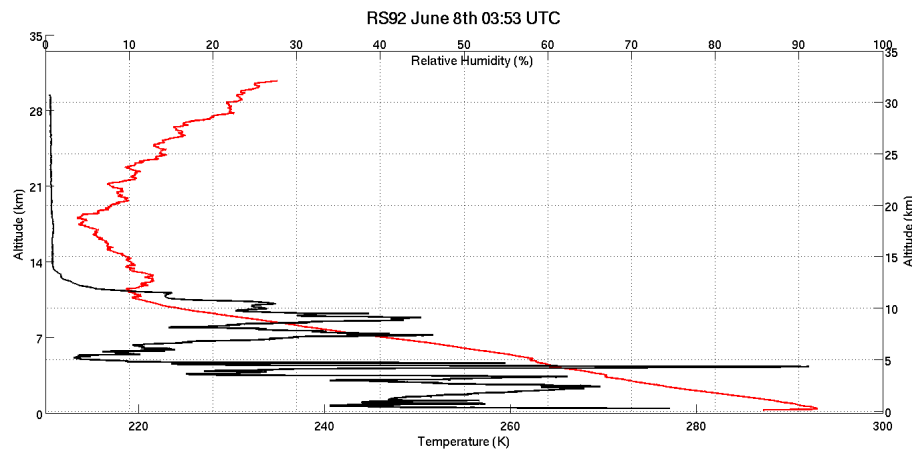


Figure A.48: RS92 profiles for temperature (red) and RH (black) on June 8th at 3:53 UTC.

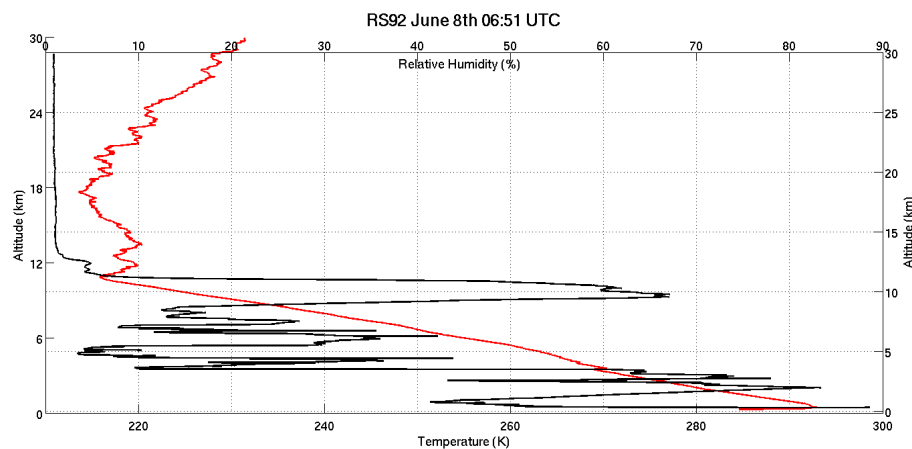


Figure A.49: RS92 profiles for temperature (red) and RH (black) on June 8th at 6:51 UTC.

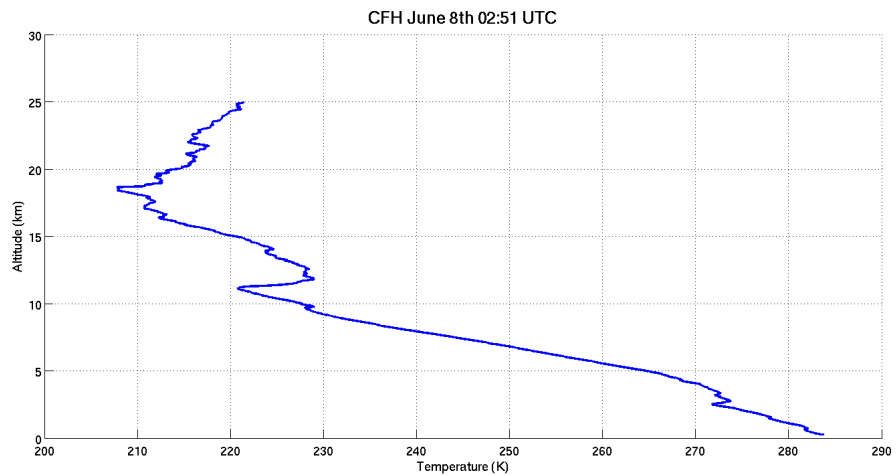


Figure A.50: CFH profile for temperature on June 8th at 2:51 UTC.

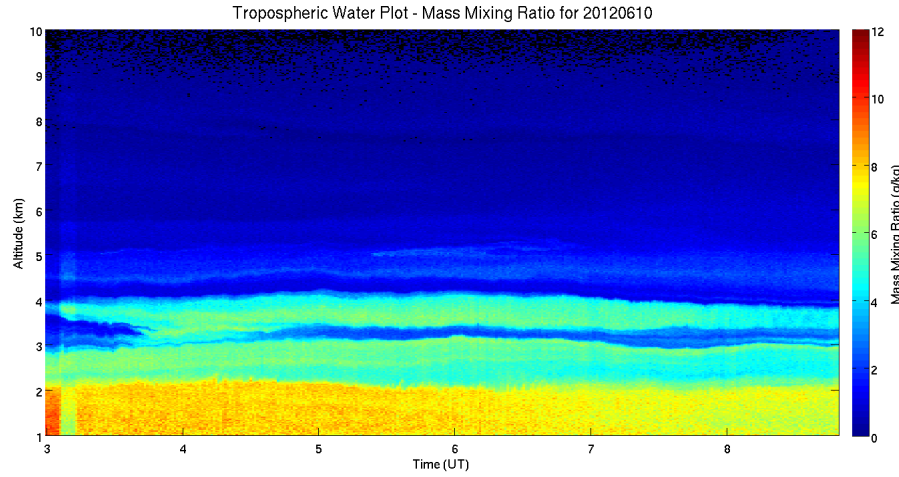


Figure A.51: PCL nightly colour plot of tropospheric water for June 10th.

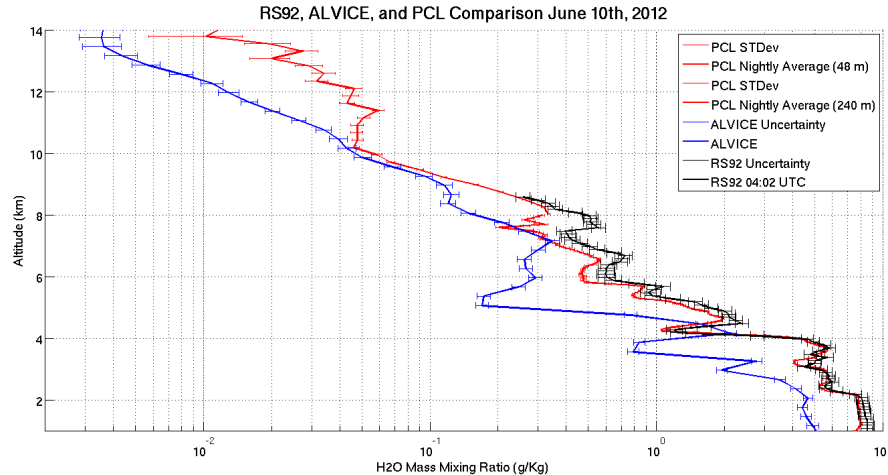


Figure A.52: PCL, ALVICE, and RS92, mass mixing ratio profiles for June 10th at 4:02 UTC.

A.10 June 10th 2012

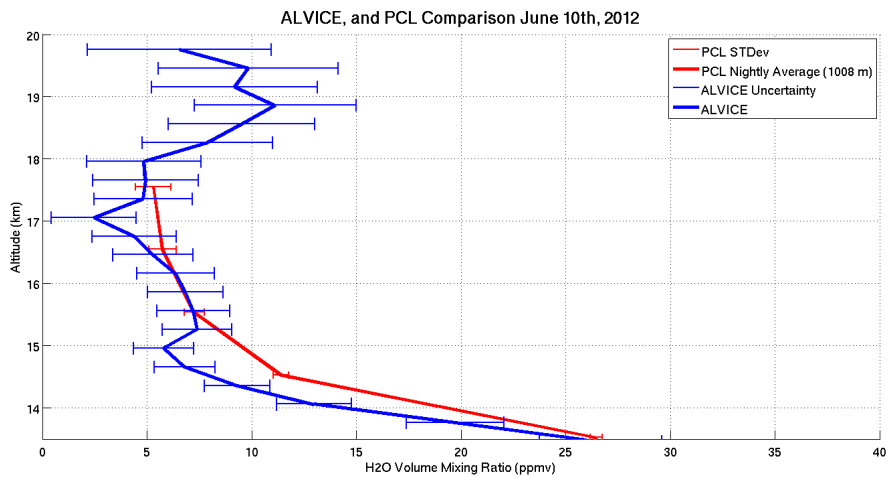


Figure A.53: PCL and ALVICE volume mixing ratio profiles for June 10th at 4:02 UTC.

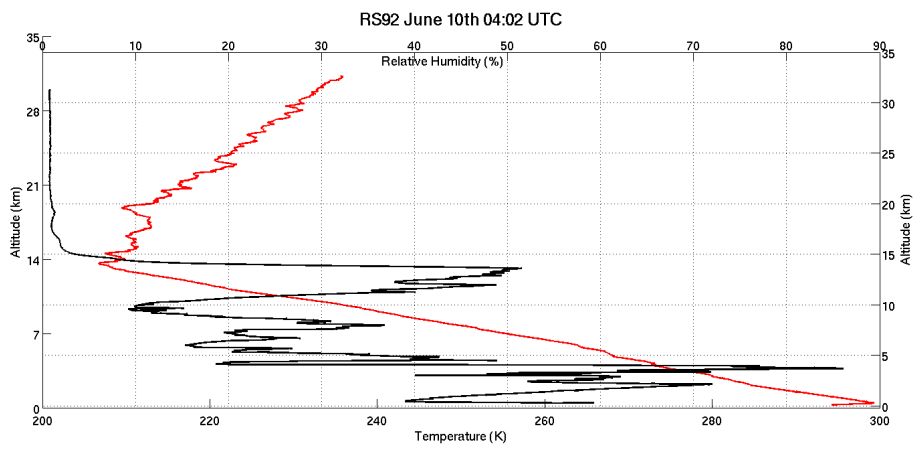


Figure A.54: RS92 profiles for temperature (red) and RH (black) on June 10th at 4:02 UTC.

Appendix B

Sample Code

B.1 Call PCL Water Code

Water vapour is called in three sections. Each section for each night of data has a unique altitude range, vertical co-add, start and end time, temporal co-add, background subtraction case, statistical rejection criterion for individual scans, windowing filter, and a mask to eliminate blocks of bad data.

```
waterlow = Water.Fetch('d',20120524,'bottomalt',275,'topalt',8000,'starttime',3.6,'endtime',4.6,'bgmode','auto'
48m, 1h
watermid = Water.Fetch('d',20120524,'bottomalt',7900,'topalt',14000,'starttime', ... 3.6,'endtime',4.6,'bgmode','auto','rejection',0.99,'coaddalt',10,'coaddtime',60,'filter','3s5s','countfilter','pclwater');
240m, 1h
waterhigh = Water.Fetch('d',20120524,'bottomalt',10000,'topalt',25000,'bgmode','auto','coaddalt',31,'coaddt
1008m, all night
```

B.2 RS92 data

RS92 data must be cleaned before use by removing any data associated with instrument malfunction. These data points are usually assigned a value of 999 but it can happen that the

automated RS92 data programme misses 'bad data' and records clearly unphysical data (ex. several data points taken at 2 km may return pressure values of 5000 hPa). These data points must be identified and removed by hand.

```
sonde = importdata('home/robin/Desktop/CampaignSondes/20120524.033925');
```

```
T = sonde(:,2) + 273.16; Temperature (K)
```

```
P = sonde(:,4); Pressure (hPa)
```

```
Z = sonde(:,3)/1000; Altitude above sea level (m)
```

```
RH = sonde(:,5); Relative Humidity
```

Remove data associated with Temperature less than -30C in RS92s

```
ind = find(T < 243.16); T(ind) = NaN;
```

B.3 Generating Water Vapour Mixing Profile from RS92

Generate a saturation vapour pressure profile for each sonde flight using the Wexler 1976 model.

```
es = 0.001*exp(-2991.279*(T.^2)-6017.0128*(T.^1)+18.87643854-0.028354721*T+  
(0.17838301 * 10^-4) * (T.^2) - (0.84150417 * 10^-9) * (T.^3) + (0.44412543 * 10^-12) * (T.^4) +  
2.858487 * log(T));
```

Calculate the partial pressure of water vapour in hPa

```
e = (RH.*es)/100;
```

Calculate the volume mixing ratio

```
vmr = RH.*(es./(P - (RH/100).*es));
```

B.4 Call the ALVICE Data

Since this is a blind comparison campaign the ALVICE data is simply called from a text file.

```
Alvice1 = importdata('home/robin/Desktop/AlviceData/ALV_20120524_033925_WV_v1.0.dat');
```

```
Alvice1alt = Alvice1(:,2);
```

```

Alvice1Temp = Alvice1(:,10) + 273.16;
Alvice1vmr = Alvice1(:,3);
Alvice1mmr = Alvice1.*(0.643071)/1e3;
Alvice1vmr_unc = Alvice1(:,5);
Alvice1mmr_unc = Alvice1(:,5)*(0.643071)/1e3;
Alvice1sonde_vmr = Alvice1(:,8);

```

B.5 Determine the Fitting Factor for Each Night

A simple code is used to reduce the distance between the RS92 and PCL profiles.

```

n = 2;
dn = 1;
while dn > 0.001;
for i = 1:length(waterlow.alt)
    distance1(i) = (((vmr(i)'-(waterlow.vmr(i).*n+dn)).^2)');
    distance2(i) = (((vmr(i)'-(waterlow.vmr(i).*n)).^2)');
    distance3(i) = (((vmr(i)'-(waterlow.vmr(i).*n-dn)).^2)');
    distance1(isnan(distance1)) = [];
    distance2(isnan(distance2)) = [];
    distance3(isnan(distance3)) = [];
    RMS1 = sqrt(sum(distance1));
    RMS2 = sqrt(sum(distance2));
    RMS3 = sqrt(sum(distance3));
    end
    if (RMS2 < RMS1) & (RMS2 < RMS3)
        dn = dn/2;
    elseif (RMS1 < RMS2)

```

```

n = n + dn;
else
n = n - dn;
end
end
fitting_factor(1,1) = n;

```

B.6 Generating a Reduced Chi-Squared Metric

As an attempt at quality control a reduced chi-squared is calculated for a fit with 114 degrees of freedom at 99.5 percent. The significance criterion is 75.55.

```

for i = 1:length(waterlow.alt)
chi1 = nansum(((fitting_factor(1,1).*waterlow.mmr)-y(i)').^2)./(waterlow.mmr_var + vmr_var),2)./(length(
1);
end
if chi1 > 75.55
chi_2(1,1) = chi1;
else
chi_2(1,1) = NaN;
end

```

B.7 Saturation Vapour Pressure Model Analysis

Calculate each SVP model.

Goff Gratch (1946) SVP over water and ice [38]

$$\begin{aligned}
esGG = 10.7(-7.90298*(373.16/(T-1))) + (5.02808*(log10(373.16/T))) - (1.3816e-7*(10.7^{12.344*(1- \\
T/373.16))-1})) + (8.1328e-3*(10.7^{-3.49149*(1-T/373.16))-1})) + (log10(1013.246)*T/T));
\end{aligned}$$

$esiGG = 10.(\hat{(-9.09718*(273.16./T)-1))} + (-3.56654*log10(273.16./T)) + (0.876793*(1-T/273.16)) + log10(6.1071));$

Goff (1957) SVP over water and ice [38]

$esG = 10.(\hat{-10.79574*(1-(T/273.16))} - 5.02800*(log10(T/273.16)) + 1.50475e-4*(1-10.(\hat{-8.2969*(T/(273.16-1))))} + 0.42873e-3*(10.(\hat{4.76955*(1-273.16)./T}-1)) + 0.78614*T/T);$

$esiG = exp(-9.096853*(273.16./(T-1))) - 3.566506*log(273.16./T) + 0.876812*(1-(T/273.16)) + log10(611.14));$

Wexler (1976) SVP over ice [70]

$esiW = exp(-2991.279*(T.^2) - 6017.0128*(T.^1) + 18.87643854 - 0.028354721*T + (0.17838301*10^4)*(T.^2) - (0.84150417*10^9)*(T.^3) + (0.44412543*10^12)*(T.^4) + 2.858487*log(T));$

Hyland and Wexler (1983) SVP over water and ice [65]

$eshW = exp((-0.58002206*(10^4))./T) + (1.3914993) - (0.048640239.*T) + ((0.41764768*(10^4)).*T.^2) - ((0.14452093*(10^7)).*T.^3) + (6.5459673*log(T));$

$esiHW = exp((-0.56745359*10^4)./T) + (0.63925247*10) + ((-0.96778430*10^2).*T) + ((0.62215701*10^6).*T.^2) + ((0.20747825*10^8).*T.^3) + ((-0.94840240*10^12).*T.^4) + ((0.41635019*10).*log(T))$

Buck (1981) SVP over water and ice (NB formulated in Celcius) [11]

$esBu = 100*6.1121*exp(17.502*C ./(C+240.97));$

$esiBu = 6.1115*exp(22.452*C ./(272.55+C));$

Sonntag (1994) SVP over water [38]

$esS = 100*exp(-6096.9385./T + 16.635794*T/T - (2.711193*10^2)*T + (1.673952*10^5)*(T.^2) + 2.433502*log(T));$

Magnus Tetens equation for SVP over water and ice (Murray 1967) [39]

$esM = 100*6.1078*exp(17.269388*(T-273.16) ./ (T-35.86));$

$esiM = 6.1078*exp(21.8745584*(T-273.16) ./ (T-7.66));$

Bolton (1980) SVP over water (NB formulated in Celcius) [6]

$esBo = 100*6.112*exp(17.67*C ./(C+243.5));$

Murphy & Koop (2005) SVP over water and ice [38]

$$esMK = \exp(54.842763 - (6763.22/T) - (4.21*(\log(T)) + (0.000367.*T) + (\tanh(0.0415*(T-218.8)).*(53.878-1331.22/T - 9.44523*\log(T) + 0.014025*T))));$$

$$esilMK = \exp(9.550426 - 5723.265/T + 3.53068*\log(T) - 0.00728332.*T);$$

Wagner and Pru (2002) SVP over water [67]

$$esWP = 22.064e6 * \exp(647.096/T. * ((-7.85951783 * (1 - T/647.096) + 1.84408259 * (1-T/647.096).1.5 - 11.7866497 * (1 - T/647.096).3 + 22.6807411 * (1-T/647.096).3.5 - 15.9618719 * (1-T/647.096).4 + 1.80122502 * (1-T/647.096).7.5)));$$

Tsonis (2002) SVP over water and ice [58]

$$esT = 6.11 * \exp(53.49 - 6808/T - 5.06*\log(T));$$

$$esiT = 6.11 * \exp(26.16 - 6293/T - 0.555*\log(T));$$

Curriculum Vitae

Name: Robin Wing

**Post-Secondary
Education and
Degrees:** University of Western Ontario
London, ON

2004 - 2010 H.BSc. Specialization in Physics and Major in Conservation Biology

**Related Work
Experience:** Teaching Assistant
The University of Western Ontario
2010 - 2012